An Interacting Particle Approach to Problems in Cancer: Osteocyte Network Formation and Histology Analysis

Jake Patrick Taylor-King

St John's College

University of Oxford

A thesis submitted for the degree of

Doctor of Philosophy

Trinity 2017

To everyone who helped along the way.

Acknowledgements

First I would like to express the most gratitude to my supervisors David Basanta and Jon Chapman. David was wonderful in that he engaged with and allowed me follow my mathematical fancies. I'll admit now that Jon had the far harder job: grounding my work in reality, and forcing me to make logical sense! It would also be remiss of me not to thank Mason Porter, who helped supervise the earlier stages of my D.Phil, before moving to UCLA.

In terms of academic motivation, Paul Dellar and Radek Erban first piqued my interest in kinetic theory years ago. It is a fascinating area with huge potential. Although not present in the thesis, I should also thank my co-authors on my earlier velocity jump work: Emiel van Loon, Gabriel Rosser, Sergei Fedotov, Rainer Klages, and in particular Robert Van Gorder.

The first section of my thesis, motivated by osteocyte network formation, would have been a monumental failure if not for the help of Pascal Buenzli and Conor Lynch. The second section of my thesis is on pathology analysis. Whilst I had a vision for a concept, it was not possible without the help of Etienne Baratchart, Andrew Dhawan, Elizabeth Coker, Inga Hansine Rye, Hege Russnes, and the tireless Andriy Marusyk.

Friends who deserve a mention include: Jacob Scott, Jan Poleszczuk, Natalie Woodward, Laurence Hutton-Smith, Casper "Casperton" Beentjes, Cristian Regep, Jaroslaw Nowak, Florien "Flobot" Klimm, Asbjorn "Ozzy" Nilsen Riseth, Heidi "Heidster" Dritschel, Citlali Solis Salas, Chris Lester, and Tomislav Plesa.

The whole Mathematical Institute is also to be thanked. Whilst I was technically associated to OCIAM and enjoyed their lecture series, having the WCMB on the 4th floor allowed me to attend so many extra talks and lectures that piqued my interest. My D.Phil was a bizarre arrangement between Oxford University and the Moffitt Cancer Center, so I also owe my

thanks to Philip Maini and Alexander Anderson for making arrangements for this scheme to be set up.

Naturally, I should also thank my family and apologise for my futile attempts at communication.

Financial support from the EPSRC, St. John's College, and the Moffitt Cancer Centre is also gratefully acknowledged.

Abstract

Two important factors in cancer progression are: metastatic ability, cancer spreading and disrupting healthy function of bodily processes; and heterogeneity, the variation in different cancers caused by genetics, the microenvironment, and stochasticity. In this thesis, we investigate two scenarios of interest using models and techniques inspired by interacting particle systems.

First, we model osteocyte network formation. Within bone, dendritic osteocytes form a spatial network allowing communication between osteocytes and osteoblasts located on the bone surface. This communication network facilitates coordinated bone formation. In the presence of a cancer, osteocytes manifest with either over- or under-developed phenotypes. Preliminary studies measuring the number of osteocytes per unit area show that the number density of osteocytes changes between healthy and pathological bone. We develop a mathematical framework to describe spatial networks, and present a stochastic agent-based model for bone formation. Our approach allows us to probe both network structure and number density of osteocytes in bone. Analysis of our model is possible via mean-field equations. We consider variations of our model to predict how changing measurable biological parameters relating to osteoblast differentiation can allow for different morphologies. We use our model to hypothesise reasons for the limited efficacy of zoledronate therapy on metastatic breast cancer.

Second, we model the diffusive microenvironment between cells to aid with pathology slide analysis. Intra-tumor phenotypic heterogeneity limits accuracy of clinical diagnostics and hampers the efficiency of anti-cancer therapies. Dealing with this cellular heterogeneity requires adequate understanding of its sources; phenotypes of tumour cells integrate hard-wired (epi-)mutational differences with responses to microenvironmental cues. The latter come in the form of both direct physical interactions,

and gradients of secreted signalling molecules. Here, we develop a partial differential equation based model that allows the separation of phenotypic responses to signalling gradients within tumour microenvironments from the combined influence of responses mediated by direct physical contact and hardwired (epi-)genetic differences. We apply our model for the analyses of breast cancer histological specimens. Our approach allows partial deconvolution of the complex inputs that shape phenotypic heterogeneity of tumour cells, and identifies cells that significantly impact gradients of signalling molecules.

Preface

This is a strange D.Phil.

I was originally signed up to do a Ph.D in computational economics at Cambridge. After realising I disliked the research approach they were using, I hesitantly signed up for a D.Phil place at Oxford entitled "Systems Approaches to Biomedical Science Industrial Doctorate Programme". With such a name, I was not exactly sure what to expect, but I ended up working in mathematical biology due to the familiarity. As time came to pass, it has now been revealed to me that this has been one of the best decisions of my life. However, the journey has been tumultuous.

Over time, a problem regarding the nature of mathematical biology as a field of study became apparent to me. It is very easy to get drawn into one of two pitfall traps. Either:

1) One may drift into mathematical obscurity and approach research problems that are years away from the laboratory and real data; or
2) One may be overly faithful to previous biological knowledge and build models with self-evident conclusions.

This is a common criticism of the field, and I certainly do not have the answer.

Having been initially advised by Mason Porter who was interested in networks, and David Basanta who was interested in metastatic bone cancer, I felt that I should be trying to combine their interests in some way. Earlier during my time in Oxford, I did my master's thesis on kinetic theory applied to swarm robotics. Being rather unimaginative, I felt I could use this toolset to think about other interacting particle systems — in this case osteocyte network formation in bone. I then asked Jon Chapman to be involved as I needed someone who knew the topic well — it turns out he knows *most* topics within applied maths well.

As such, the first part of my D.Phil considers using kinetic theory to explain osteocyte network formation in different microenvironments. Whilst this was a nice problem in that it elucidated on a mechanism seldom studied systematically by biologists, I felt that if one reasoned through the problem carefully, one *may* be able to heuristically come to some of the conclusions. Some results did in fact turn out to be unintuitive — a pleasant surprise!

However, I still wanted to see if I could find a problem which steered well clear of the two pitfall traps. The holy grail for me was twofold: first to find a problem where I could design a reusable tool; and second, a problem that utilised the mechanistic modelling frameworks with which I was familiar.

The problem that came to mind was cellular heterogeneity. Using interacting particle systems to approach interacting cellular systems is no longer very original. However, one should not disregard what has been done previously. Cellular automaton models have indeed driven the field forward. The crux of why they have limited utility appears to be that objects within a cellular automaton belong to a state space that the modeller has to specify. And this is essentially half the problem with any mathematical cancer modelling — one can not specify what mutations are important ('driver mutations') until one has done prior genetic screening. Similarly, one cannot know what environmental factors are important until the relevant experiments have been carried out to show that they are indeed important. We have now reverted back to the second pitfall of circular reasoning.

If this were not enough, in the case of cancer, the attractive mathematical framework of kinetic theory where we take mean field limits is unsuitable. It is the fluctuations in a system that show the interesting behaviour, so averaging out fluctuations is an entirely unsuitable thing to do! The first pitfall is not even available to us were we so inclined to go that way.

The second part of my D.Phil changes track. It is essentially about posing a model that we *know* to be incorrect, but to see if the differences between the model and data can be assumed to be representative of a biological reality. The fundamental assumption is that while cells may have different

internal dynamics, their method of communication is identical between all cells.

So, there we have it. I've had a wonderful time at Oxford; and while one can always do *more* work for a D.Phil, I'm pleased to say that it is the chance to chase originality that has made this whole venture worth pursuing.

Contents

List of Figures

Chapter 1

Introduction

Cancer is an evolutionary disease characterised by abnormal cell growth, and in advanced cases, metastasis (the spread of cancer cells to other parts of the body). The progression of cancer is governed by the phenotypes of the cells within a tumour. Phenotypic heterogeneity is associated with tumour aggression, and also complicates diagnosis and underpins therapy resistance. This heterogeneity arises as the result of interplay between: a) cell-intrinsic differences stemming from genetic heterogeneity and stable epigenetically defined states; b) stochasticity arising via variability in gene expression; and c) environmental inputs in the form of physical forces, contact-mediated signals from neighbouring cells, the extracellular matrix (ECM), and diffusible signals in the form of gradients of growth factors, cytokines, oxygen and metabolites [103]. Metastasis occurs through the lymphatic system and blood vessels, and cells preferentially move from a specific primary tumour location to form a secondary (or metastatic) tumour [60].

Metastases and the treatments they require are the leading causes of mortality from cancer [144]. The establishment of a metastasis is broadly believed to follow the "seed and soil" hypothesis where cells from one organ move to a second with a favourable microenvironment [60]. Additionally however, genetic mutations present only in secondary tumours (and not in the primary) have been found. Once at the new location for colonisation, tumour cells will drastically alter the microenvironment to create "niches" to promote survival and avoid the immune system; examples of niches include, hypoxia-induced angiogenesis [88] and immunoediting [156]. For example, prostate and breast cancer frequently metastasise to bone, where they infiltrate and disrupt the bone formation process. Crucially, once a secondary tumour has established itself, it can disrupt healthy function of the organ in question. For example, in bone cancer, the bone remodelling cycle can be disrupted and can lead to incorrect

structure both at the macroscopic scale (net bone gain/loss) and microscopic scale (malformed osteocyte networks).

When considering anti-cancer therapeutics, the primary issue that has recently emerged is that heterogeneity is a critical biomarker of tumour prognosis, as greater heterogeneity provides a clear advantage in the face of the evolutionary bottleneck of anti-cancer therapy — there are simply more paths available to facilitate the generation of resistance [97]. The design of therapies must consider the existing heterogeneity in a tumour and account for the most aggressive cells that may exist; and in failing to do so, one may select for pre-existing resistant cells [102]. Furthermore, a critical generator of phenotypic heterogeneity involves microenvironmental variability within the tumour, as a varying environment contributes greatly to different modes of adaption upon spatially organised subgroups of cells [149]. In fact, it has been shown that heterogeneity of oxygen distribution within a tumour leads to the adaption of subsets of cells in microenvironmental niches to the hypoxic microenvironment, which has been shown to result in poorer prognosis and more aggressive tumours [95]. Lastly, heterogeneity has also been implicated as an important consideration in the field of immunotherapy, where neo-antigen generation is a function of polypeptide heterogeneity, which is a critical determinant of the success of immunotherapy, and reflects underlying genetic heterogeneity [139].

※

Mathematical modelling appears to be a somewhat formal process for constructing conceptual metaphors; one uses mathematical constructions and operations (the *source domain*) to understand physical reality (the *target domain*) [9]. Essentially, one puts our beliefs and incomplete knowledge into formal equations and expressions; this allows us to propose future experiments and make predictions when perturbing the mathematical construction. Particularly in cases where the system of interest is difficult to observe, a mathematical modelling approach can be exceedingly relevant.

Ignoring the microbiome, all human body function (and malfunction) is the coordinated action of the cells within it. When it is necessary to model each cell separately, a common theme within mathematical biology is the construction, simulation, and analysis of cellular automata (CA) and other interacting particle systems, often built upon the foundations of kinetic theory. This has been a proven success at replicating the core qualitative behaviour of many biological processes that involve the movement of "particles" (e.g., animals, cells, bacteria, proteins, ions etc).

Within this thesis we create models of interacting particle systems to approach two problems, the first relating to metastasis and the second relating to heterogeneity. The first system we wish to look at is metastatic bone cancer, where the secondary tumour alters the microenvironment leading to malformed osteocyte networks; osteocyte networks being a cellular communication network to allow for coordinated bone remodelling. We wish to know how different types of metastatic bone cancer can lead to different osteocyte morphologies. The second problem we wish to approach is broader — heterogeneity; can we use mathematical modelling to estimate how cells contribute to their local microenvironment?

Through partnership with the Moffitt Cancer Center, we have obtained histology slides for bone and breast cancer. For the bone samples, using image analysis, one can locate the osteocytes within bone, unfortunately without elucidating on the underlying network structure. For the breast cancer samples, cells are stained multiple times, reflecting the concentrations of intracellular protein targets.

As well as using our mathematical models to answer biological questions, we are also required to build modelling frameworks to deal with two problems. The first is the networked structure of cellular communication: Osteocytes have a network structure; not every cell can communicate with every other cell because osteocytes are encased in osteoid and mineralised calcium. The second is heterogeneity: cells cannot be considered identical agents following the same rules. When each cell has the potential to be mutated in a different way, assuming all cancer cells act according to the same rules is an unrealistic assumption.

For the preceding two problems, different approaches must be taken and assumptions must be made to analyse the models presented.

When modelling osteocyte network structure, we want to analyse how the network forms, and find summary statistics for our model. This is an intrinsically dynamic process, and so we build a forward model of osteocyte network formation. We examine how, after initialisation, different parameterisations and modelling assumptions lead to different network morphologies.

When modelling phenotypic heterogeneity, we assume there is a diffusible microenvironment of cytokines between cells, and this microenvironment is at a steady state, with all other processes happening at slower timescales. These assumptions allow us to build an inverse problem where we can estimate to what extent each cell on a pathology slide is contributing to this diffusible microenvironment.

We now provide three literature reviews on the three topics: cancerous osteocyte network formation, cellular heterogeneity, and interacting particle systems.

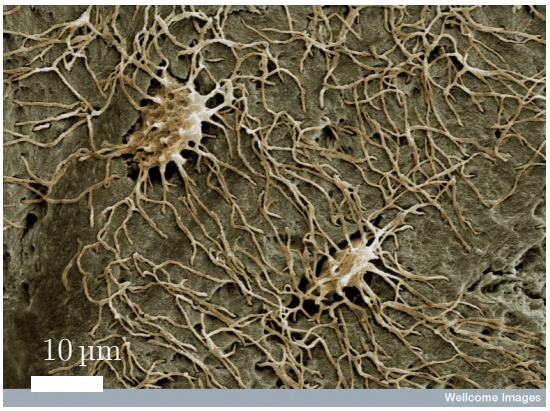

Figure 1.1: Scanning electron micrograph of osteocytes in bone. The sample was prepared by embedding the bone in resin, which was subsequently etched with perchloric acid. The image was created by removing the entire mineral in the sample, leaving a replica of the cells. Therefore, what is observed is the resin that filled the spaces in the bone and the spaces inside the cells. Scale bar is approximate only. (This picture is copyrighted work and is available via Creative Commons [28] from Kevin Mackenzie, University of Aberdeen, Wellcome Images [158].)

1.1 Cancerous Osteocyte Network Formation

1.1.1 Healthy Bone Remodelling

Bone remodelling consists of careful coordination between 3 cell types: *osteoblasts*, *osteoclasts*, and *osteocytes*. Osteoblasts line bone surfaces due to be remodelled, and then move aside for osteoclasts to resorb old or damaged bone. New bone is created by osteoblasts secreting osteoid (a scaffold), and undergoing terminal differentiation into osteocytes. As this differentiation process occurs, the osteoid becomes calcified. Bone is constantly being recycled; damaged bone is resorbed and new bone built.

An *osteocyte* [151] is a cell found in cortical (dense weight bearing bone) and trabecular ("flexible" porous highly vascularised bone) bone. The cell has protrusions (or dendrites), which are known as *processes* and form a communication network between the osteocytes and cells on the bone surface. To avoid confusion, we refer to *processes* as dendrites. Osteocytes are densely packed in bone, where they occupy spherical cavities called *lacunae*; their dendrites occupy porous channels called *canaliculi* [27, 124]. The dendrites enable communication via gap junctions, allowing diffusion of signalling molecules to take place. Additionally, around the osteocyte network there is a thin layer of fluid.

Perturbations in osteocyte-network organisation can impact both fluid flow and diffusion and thereby allow mechanosensation and signalling [78, 81, 92, 143]. The exchange of signalling molecules relate to: oestrogen deficiency, skeletal unloading, and fatigue damage [75]. The variety of signalling molecules detected is vast and arise in the regulation of many other organs; these include Receptor Activator of Nuclear Factor Kappa-B Ligand (RANKL), Vascular Endothelial Growth Factor (VEGF) [75], Parathyroid Hormone (PTH) [164], calcium ions (Ca^{2+}) [72], and Sclerostin [138].

Because of the location of osteocyte networks in bone, it is difficult to examine

Table 1.1: Cancer type impact on bone morphology.

Cancer type	**Origin**	**Bone growth**	**Osteocyte morphology**	**Ref.**
Osteogenic Sarcoma. [Fig. 1.2(*i*)]	Mesenchymal cells	Mixture	Canaliculi upregulated, Lacunae empty.	[145]
Osteoma (benign). [Fig. 1.2(*ii*)]	Unknown	Osteoblastic	Canaliculi down regulated (retarded growth).	[145]
Myeloma	Plasma cells / White blood cells	Primarily osteolytic	Osteocyte lacunae spherical, canaliculi reduced in number, shorter, distorted.	[41, 87]
Metastasis (A group)	Lung, Breast, Liver	Primarily osteolytic	Unknown	[41]
Metastasis (B group)	Prostate	Primarily osteoblastic	Unknown	[93]

them experimentally. In Figure 1.1, we show the outcome of applying an obtrusive experimental technique to view osteocytes after nearby mineral has been dissolved. Three-dimensional imaging data is now available by using confocal microscopy [76, 147, 148], and such work has led to the identification of some structural features of osteocyte networks. Identified features include the mean number of dendrites that protrude from each osteocyte [148] and mean lengths of a canalicular network [22]. Other work has reported that high-density networks correlate positively with high bone quality. Note the mineral matrix has an orientation (due to dendrites and collagen), and bone quality is associated with the level of organisation of this mineral matrix [78].

1.1.2 Bone Cancer

Advanced prostate, breast, and lung cancer commonly metastasise to bone [134, 168]. With the onset of various types of bone cancer, it is common for the bone remodelling process to be disrupted. A particularly painful symptom is net bone formation in some regions and simultaneous weakening in other areas [126]. Small bone lesions can also develop. Much previous work has been focused on macroscopic properties of the resulting bone, e.g., the osteoblastic (net bone formation) and osteolytic (net bone reduction) phenotypes. As bone is formed and resorbed cyclically, osteocyte networks can be morphologically malformed. A relatively unexplored area regarding cancerous bone formation is the study of osteoblast to osteocyte differentiation whilst concurrently taking into account network structure.

It was evidenced in Refs. [41, 145] that for myeloma and (benign) osteoma, osteocytes appear exceptionally spherical with shorter distorted dendrites that are reduced in number. An experimentally contrasting osteocyte network was observed with unregulated excessive dendritic growth (greater numbers of dendrites) in the presence of osteogenic sarcoma [145]. Broadly speaking, osteocytes within a cancerous microenvironment display either over- or under-developed phenotypes (see Figure 1.2) leading to "more connected" or "less connected" networks. Table 1.1 summarises the findings of a literature review linking bone cancer type to bone phenotype.

Understanding the full nature of bone formation networks is now becoming important, especially understanding how osteocyte network structure relates to the limited effectiveness of current anti-cancer therapy. Therapeutically, zoledronic acid is frequently used to treat metastatic breast cancer (BCA) where pathological bone is formed with lower densities of osteocytes per unit volume; zoledronate then helps recover the number of osteocytes, but can lead to brittle bone. There is also literature available suggesting that metastatic prostate cancer (PCA) leads to increased levels of osteoblast proliferation, and/or increased levels of differentiation [93]. For example, TGFβ expressed by tumour cells promotes excessive osteoblast growth [91], however, TGFβ targeted cancer therapy has only been a mitigated success [33].

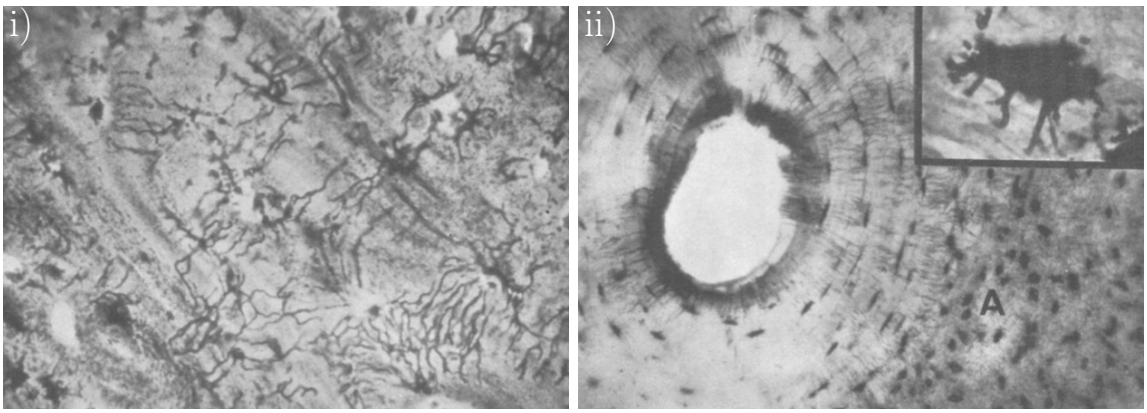

Figure 1.2: Histology slices of cancerous bone. (i) Morphology of osteocyte network showing extensive irregular canaliculi formation. Sample is from patient with sarcoma of the jaw. (ii) Morphology of osteocyte network around a Haversian canal showing normal osteocytes next to the area (A) showing osteocytes with stunted dendrites. Sample is from patient with osteoma. On higher magnification (*inset*) one can see a close up of an osteocyte from the region (A). (Figures recreated with permission from Ref. [145].)

Because osteocytes are cells derived from osteoblasts, osteocyte morphology is primarily influenced by the bone formation phase. Minimal changes to osteocyte morphology may occur, but primarily in older osteocytes [34, 35]. Whilst the osteo-

cyte and dendrites may move within the lacunae and canaliculi channels, the actual physical structures stay fixed. For this reason, we focus on the bone formation phase.

1.1.3 Bone Formation Phase

When there is no bone remodelling taking place, a layer of osteoblasts line the surfaces of bone. Osteoblasts originate from mesenchymal cells and have one of four possible fates: undergo apoptosis (approximately 65%), become embedded in bone as osteocytes (approximately 30%), transform into inactive osteoblasts and become bone-lining cells, or trans-differentiate into cells that deposit chondroid bone [44]. Osteoblasts express RANKL and osteoprotegerin (OPG), which promote and inhibit the bone resorption by osteoclasts, respectively.

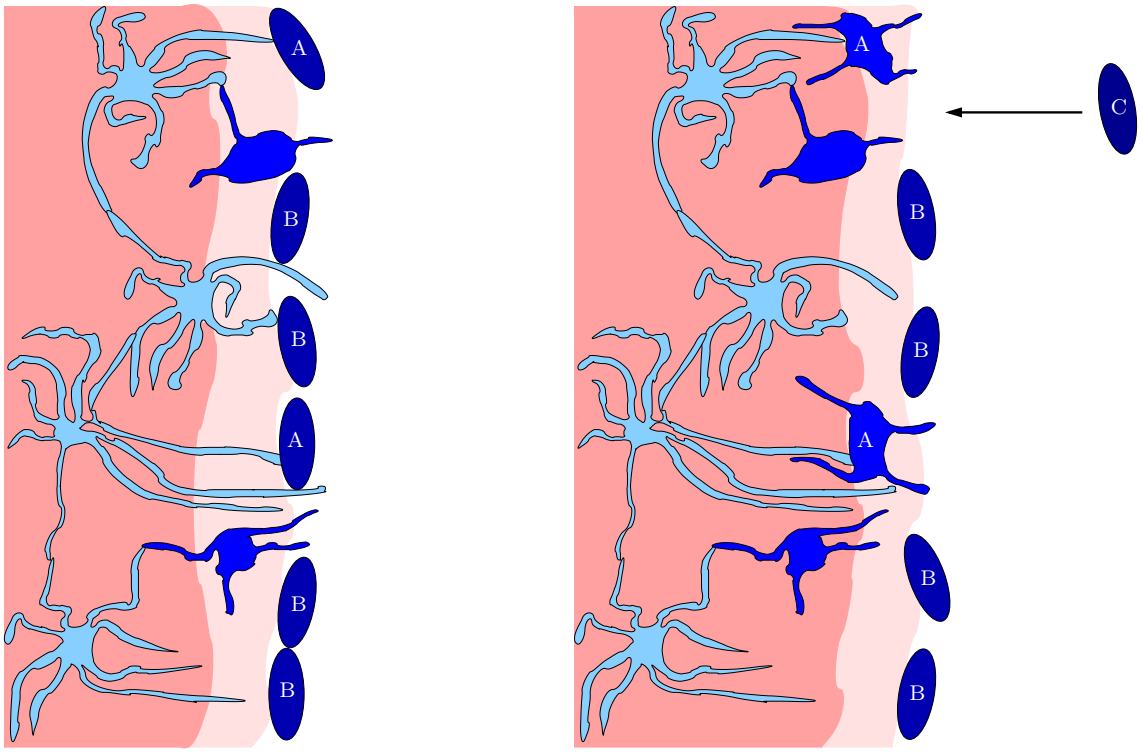

Figure 1.3: Diagrammatic illustration of the bone-formation process. Lighter shades of blue indicate more differentiated cells. The lighter shade of pink indicates the deposition front, and the darker shade of pink indicates the mineralisation front. The left panel precedes the right panel. Dendritic osteocytes (light blue) have dendrites that extend towards the osteoblast layer (dark blue). The osteoblasts secrete bone matrix. Osteoblast cells marked with "A" are signalled by the osteocyte network to differentiate into osteocytes. Osteoblast cells marked with "B" do not differentiate and stay on the outer bone surface. Osteoblast cells marked with "C" arrive at the bone front after differentiating from precursor osteoblasts (preosteoblasts). (This figure is inspired by a similar illustration in Ref. [44].)

Upon some signalling event, multi-nucleated osteoclasts arrive and the osteoblasts

move aside. The osteoclasts then burrow into the bone; as they do so, they resorb some of the osteocyte matrix [132]. It has been suggested that after an osteocyte undergoes apoptosis, pro-osteoclastogenic signals are released by the osteocyte's neighbours in the network [77].

A trail of osteoblasts then follows the osteoclasts and secretes new bone matrix[1], although some of these get left behind to become osteocytes. This second stage is the bone formation phase. Kamioka *et. al.* suggested osteoblasts are incorporated into the osteocyte network by mature osteocytes extending their dendrites towards the osteoblast layer [76, 99, 101, 115, 118].

Thus far, we have discussed three types of bone cells: osteoblasts, osteoclasts, and osteocytes. For at least the osteoblast-to-osteocyte cell transition, biologists have subdivided the process of cell differentiation to include eight phenotypes: (*i*) preosteoblast; (*ii*) preosteoblastic osteoblast; (*iii*) osteoblast; (*iv*) osteoblastic osteocyte; (*v*) osteoid-osteocyte (i.e., Type-II preosteocyte); (*vi*) Type-III preosteocyte; (*vii*) young osteocyte; and (*viii*) old osteocyte [44]. Additionally, the secretion of bone occurs as two steps: first osteoid is deposited as a scaffold, and then mineralisation occurs to confer strength. Stages (*iv*)–(*vi*) are cells after the deposition front but before the mineralisation front; they are surrounded by a non-mineralised osteoid matrix. (In other words, there is scaffold around them.) Stages (*vii*)–(*viii*) are cells whose volume has depleted (by reduction in the endoplasmic reticulum and Golgi apparatus) and are in mineralised bone. The diagram in Figure 1.3 shows the bone-formation step. Although it is potentially useful to consider all the above phases (defined from osteogenic markers, see [44]), we are interested only in the structure of a mature osteocyte network [stages (*vi*)–(*viii*)], so we will make simplifications when later building mathematical models.

1.1.4 Data Available

Through collaboration with the Moffitt Cancer Center, we obtained mice tibia samples under different experimental protocols. All animal studies were conducted under University of South Florida IACUC approved protocols (R2238 and R1762-CCL).

Specimens for analysis were derived from mice that were intratibially inoculated with either saline (Control), prostate cancer (PCa, PAIII cell line) or breast cancer (BCa, PyMT cell line) as described previously [7, 152]. Mice were harvested for analysis prior to breach of the cortical bone (day 14 for PAIII study mice, Day 21 for

[1]The unit that consists of osteoblasts following osteoclasts is known as a "Bone Multicellular Unit" (BMU).

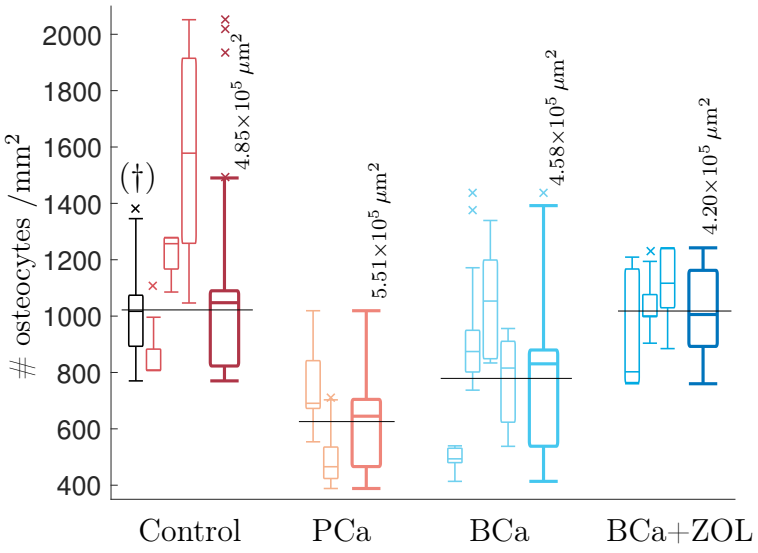

Figure 1.4: Tukey box plots to show results of preliminary image analysis of osteocyte number density. Means plotted in black. The far left histogram (marked †) is representative of a collection of histology slides imaged at a lower resolution. Total area measured for each experimental protocol marked next to each combined box plot.

PyMT study mice). Additionally, BCa-PyMT inoculated mice were treated with a bisphosphonate (zoledronate) over the course of the study period (1mg/Kg, subcutaneously thrice weekly) [7, 152]. Subsequent to tissue collection and isolation, bones were decalcified, processed and paraffin embedded. Sections (5μm) were generated, rehydrated and then stained with either Gomori's Trichrome or Hematoxylin & Eosin using standard procedures. This formed the basis of a preliminary study described below.

The trabecular bone had osteocytes (and their communication network) embedded within them. Unfortunately, the samples were not at a quality high enough to determine network structure, however it was possible to estimate number of osteocytes per unit area (#osteocytes/mm^2).

Using routine image analysis tools (see Appendix A), we created a user assisted algorithm to estimate the area of visible bone within a pathology slice, and subsequently count the number of osteocytes within this region. In Figure 1.4, we see box plots presenting the results. The smaller box plots are the osteocyte densities for each mouse using a few imaging slides (3–8 slides per mouse), weighted by the quantity of visible bone within the sample. The larger box plots show the combined data for mice undergoing the same protocol.

From Figure 1.4, prostate and breast pathological bone have lower osteocyte number densities when compared to healthy bone. When applied as a therapy for breast cancer, it appears the zoledronate treatment allows for partial recovery of osteocyte number density.

Common to both cancers is the reduced osteocyte number density. However there are also differences between the cancer pathologies: breast cancer is more often osteolytic and suppresses osteoblast proliferation and maturation, whilst prostate cancer is more often osteoblastic and promotes osteoblast proliferation and maturation.

When viewing the pathology slides of bone under the breast cancer protocol, there seems to be some noticeable quantity of osteoblasts that were buried without full differentiation. This manifests as osteocytes that are larger and more osteoblast-like inside a lacunae with excess space around the cell body, see Figure 1.5. In this work, we do not carry out rigorous analysis of osteocyte sizes. When referring back to Table 1.1, we believe this is consistent with osteocyte phenotype where cells are inside *spherical lacunae* and have *downregulated canaliculi*. Therefore, we assume breast cancer has poor osteocyte network formation and therefore the dendritic network is less connected. The prostate cancer samples however were more difficult to interpret.

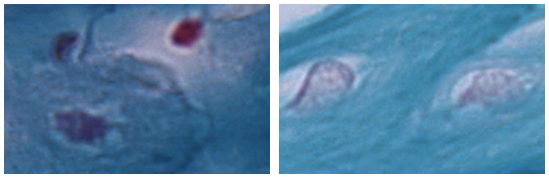

Figure 1.5: Comparison between osteocyte sizes: (left) control, (right) bone under breast cancer protocol. Image size corresponds to $32 \times 21\,\mu$m.

The zoledronate treatment is known to improve osteoblast proliferation and maturation while simultaneously killing osteoclasts. It should also be noted that the zoledronated treated bone is brittle compared to healthy bone; this brittleness is suggestive of poor osteocyte network formation. One should then be able to conclude that whilst zoledronate therapy restores osteocyte number density, it does not restore the osteocyte network structure.

1.1.5 Previous Mathematical Models

The functional role of these different network topologies is unclear and can be investigated with mathematical modelling. Experimental work reveals a snapshot of the communication between the osteocytes within bone, and the osteoblasts on the bone surface. Sclerostin has been stained for and observed within the dendrite structures between osteocytes and osteoblasts [127]. From these studies, it is clear that one should place importance on incorporating some aspect of network structure so one can adequately model osteoblast differentiation.

Numerous previous studies have examined osteocyte density, but none of them explore network structure. References [54, 107, 161] give ordinary differential equations (ODE) and hence non-spatial models for cell populations; these include osteoblast,

osteoclast, and osteocyte populations. Existing models of healthy bone remodelling (homeostasis) include partial differential equation (PDE) models [135, 136] and then these models have been adapted for the cancerous regime [137]. Mechanically focused models capturing stresses and strains on the bone have also been explored [131, 155]. A general continuum modelling approach has also been proposed [20].

1.1.6 Requirements for New Generations of Models

Suppose we wanted to build an agent-based model accounting for osteocyte network structure. The agents in our model would be cells within a spatial network. The spatial network would then specify if cells were able to communicate. Based on the description of the bone formation phase, the minimum requirements for a model would be that:

1) A network structure is modelled in a mathematically consistent way;

2) Agents have a "state", that may dynamically change, e.g., position, cell type, how the cell is embedded in the network structure;

3) Network structure is added to/modified over time;

4) New agents enter the system through (pre-)osteoblast proliferation/migration; and

5) The domain may change size.

Agents of the same type (either osteocytes or osteoblasts) would then follow the same rules, although each agent may have different states.

By accounting for network structure in an agent-based model, providing analysis of the model is possible, one should inquire how candidate mechanisms lead to different osteocyte morphologies. Additionally, one should then explain how the process is altered in cancerous microenvironments.

1.2 Heterogeneity in Cancer

1.2.1 Evolution in Cancer

In Nowell's seminal paper [110], it was put forward that cancer was an evolutionary process: cells would undergo clonal expansion, genetic diversification, and clonal

selection. Evolution happens at an (epi-)genetic level but is shaped by the tissue ecosystem and the tumour progenitor cell [55].

The central dogma of molecular biology explains how genetic information flows within a biological system. In short, *deoxyribonucleic acid* (DNA) undergoes transcription into *ribonucleic acid* (RNA), which then undergoes translation into proteins. However, this whole process is in fact a lot more complicated due to other transfers of biological sequential information and regulation, e.g., reverse transcription, non-coding RNA, RNA replication, post-translational modification etc. Note also the term *gene*, that is, a functional unit of inheritance traditionally defined as a sequence of DNA base pairs that encodes for a specific protein[2] [48]. When mutations occur, DNA base pair sequences are altered which leads to the corresponding RNA producing modified proteins, which then affects cell function. The types of mutations include local changes to DNA base pairs, e.g., missense and nonsense mutations. However, there are more involved mutations such as insertions, deletions, and duplications which apply to larger sections of the DNA strand, or involve multiple strands. These mutations can then be classified, e.g., frameshift mutations, repeat expansions.

As one can imagine, stochasticity is a big driver of mutation; however the microenvironmental context in which the cell resides selects for phenotypes that thrive within said environment. There are many types of microenvironments which are commonly studied, and often these relate to metabolites, e.g., hypoxia (insufficient oxygen), acidity (low pH), hypoglycaemia (insufficient glucose). Other noted microenvironments include: necrotic (factors related to cell apoptosis), immunoreactive (abundance of immune cell infiltration), immunoinflamed (cytokine abundance).

1.2.2 Quantification of Genetic Heterogeneity

With the advent of low-cost high-fidelity genetic sequencing, intra-tumour genetic heterogeneity may be assayed with high accuracy. There are many methods for analysing genetic material, although it seems most techniques are grounded upon variations of either: sequencing of cells [62], DNA microarrays [26], or fluorescence *in-situ* hybridisation (FISH) based methods [69].

Sequencing of cells allows for analysis of the whole genome. Bulk tumour strategies utilise measurements such as variant allele frequencies (VAFs) to characterise the proportion of different genetic subtypes comprising a tumour from bulk sequencing

[2]Definitions have often been altered over time to incorporate newly observed biological phenomena, e.g., RNA editing, protein *trans*-splicing etc.

data, which may be used to construct phylogenetic histories of the genetic heterogeneity arising within a tumour [6]. Bulk sequencing a tumour can be expensive and will miss out spatial contexts, often giving data regarding a population average not representative of any single cell [157]. With single-cell level sequencing of the genome for cells in different spatial regions of a pathological sample, intra-sample genetic heterogeneity may be captured. However, single-cell is even more expensive, and data sets are noisy. Quantification of this genetic heterogeneity on a statistical level, to better understand disease progression, particularly in evolutionary diseases, such as cancer, is proving to be very promising [47, 97, 159].

DNA microarrays and FISH methods are probe based methods. Essentially, one tests for specific sequences (associated with genes) to see if they are present; this is done by attaching a fluorophore-, silver-, or chemiluminescence-labeled target to determine the relative abundance of a nucleic acid sequence in the target. The (frankly) amazing feature of FISH is that it is *in situ*, so one can apply it to histology slides and preserve their spatial structure [69].

1.2.3 Histology slides

Microscopy imaging of histological specimens is widely and routinely used in clinical diagnostics of cancers, as well as in experimental studies aiming to understand the underlying biology and responses to anti-cancer therapies. After fixation and placement on glass slides, tissues are subjected to chromogenic or fluorescent staining using chemical or antibody-based stains[3]. Staining intensity reflects concentration of the chemical moiety to which the stain binds. Therefore, digitisation of chromogenic or fluorescent signals allows quantification the of concentration of these chemicals. Since histological slides retain spatial information, they are suitable for the analysis of not only cellular phenotypes and genotypes, but also microenvironmental factors that shape cellular heterogeneity [64].

1.2.4 Data Available

Through collaboration with the Moffitt Cancer Center and the University of Oslo, we obtained multi-channel immunofluorescence *in-situ* hybridisation (iFISH) stained breast cancer histology samples [69]. The data used were collected in compliance with the Declaration of Helsinki and approved by the regional ethics committee (REK

[3]Note once fixation has taken place, using these cells for sequencing is no longer an option.

S-06495b) and the institutional review board of Oslo University Hospital Radiumhospitalet (IRB 2006-53). Full details of the experimental protocol can be found in Refs. [2, 154].

For the stained samples, 5 channels were available. Two channels related to the FISH procedure, both a *HER2* gene specific probe and a centromeric probe (centromere 17). The *HER2* gene is associated with poor prognosis in breast cancer and encodes the *HER2* protein [105]. The *HER2* gene is found on centromere 17, and so by looking at the ratio of the number of copies of the *HER2* gene probes detected compared to the number of centromere 17 probes detected, one can specify if the *HER2* gene is amplified.

The other 3 channels were the IHC stains: *DAPI* that reflects cellular DNA content; the *HER2* protein, a receptor tyrosine kinase that is amplified in a subset of breast cancers; and *Oestrogen Receptor (ER)*, a nuclear receptor that mediates cellular response to oestrogen signalling. Both *HER2* and *ER* expression are expected to have profound influence on cell phenotypes.

1.2.5 Previous Mathematical Models

Substantial mathematical modelling efforts have been focused on understanding the impact of the microenvironment on phenotypic heterogeneity using biophysical principles; common themes include diffusion of cytokines, and construction of chemical reaction networks. Efforts at modelling the microenvironment in a spatial setting have largely been focused on forward modelling, where one makes assumptions and rules for a model, initiates the model in some starting configuration, and then evolves it forward in time. Due to the complexity of the models involved, cellular automata approaches have often been utilised [3–5, 13, 125]. Such approaches, depending on the complexity of the rules built into the model, can reproduce many experimental/clinical observations, and in some cases are capable of making experimentally validated predictions [7]. Unfortunately, mathematical modelling approaches are limited by: the frequent need for model iteration, where model components are added and removed; the complexity of rules needed to describe the behaviour of biological systems, underlying assumptions may often be untestable; and the experimental difficulty obtaining relevant measurements required for adequate parametrisation of the underlying model.

People have also applied quantitative techniques to image analysis, however these statistical approaches have been focused on the tasks of feature extraction, feature

selection, and dimension reduction of large histological images. This field is sometimes known as whole-slide imaging (WSI). Feature extraction can happen at both a pixel-level, largely uninterpretable by a human (e.g., pixel intensities compared to neighbours), and at an object-level, recovering features in which a pathologist would naturally be interested (e.g., circularity of cell nuclei, location of blood vessels). Feature selection (along with the preceding staining procedure) can be carried out depending on the histopathology of the specific disorder, or based on dimensionality reduction (e.g., using principle component analysis) and irrelevant features can be ignored. Feature analysis is a statistical/machine learning problem, where the aim is to link the collective cell (or pixel) properties to macroscopic disorders/clinical outcomes [49]. Modern trends include considering ecologically motivated spatial statistics [64, 108]. Histology analysis is both cheap and also highly clinically relevant, and a pathologist can make a diagnosis based on an image. However, a histology slide is static and one is seldom able to elucidate any mechanism underlying observations.

1.2.6 Requirements for New Generations of Models

The main drawback to forward mathematical modelling of heterogeneous cell populations in is the over specification of *a priori* knowledge. For example, in breast cancer, the following paracrine molecules have been detected: Wnt signalling, epidermal growth factor (EGF), fibroblast growth factors (FGFs), insulin-like growth factor (IGF), transforming growth factor-beta (TGFβ) [and therefore bone morphogenetic proteins (BMPs)], and Notch signalling [133]. The aforementioned examples are only a subset of the full list of proteins, and it should be noted that these are not individual proteins, but usually families of proteins under one umbrella. Genetic differences between cells are too numerous to count, however some group properties are considered notable, e.g., triple negative breast cancer where the cells do not express the genes for oestrogen receptor, progesterone receptor, or *HER2*. The point being, trying to incorporate all this into a model is nigh on impossible.

Incorporating discretely labelled genotyped cells may be possible, e.g., one could build a CA model where cells are cancerous, with some probability of having one of a finite number of mutations which then subsequently affect the behaviour of the cell in question. Due to extensive genetic sequencing of tumours, one can use results from statistical analysis to identify and include mutations which are relevant to the process under investigation.

With proteomics, one is able to identify what proteins may exist both within cells, and within the extracellular matrix (ECM). However, a harder task is to specify which

proteins are important, and how they react. That is, a signalling molecule may have been observed, and subsequently built into a model — however, unless one knows the signalling mechanism well, it can be hard to specify confidence in conclusions.

Continuing new iterations of models may allow one to move "closer" to the truth, however to break from this cycle we need a method to tell us what cytokines we should be including in our models. We need a method to "rule in" critical determinants.

1.3 Interacting Particle Systems

Contemporary mathematical biology frequently uses some variant of reaction–diffusion modelling, often with a discrete set of interacting particles as agents. These models (hopefully) can be derived from first principles, and so we provide a general overview here as to how one would go about doing this. Before we describe interacting particle systems, we start with the easier case of particle motion without interactions.

1.3.1 Non-Interacting Particle Systems

Imagine a particle has a state vector $\boldsymbol{s}$ that is embedded within state space $\mathbb{S}$. This state space could be representative of the particle's genotype, phenotype, position, velocity, or other physical or latent social variable. Two things are then required for a model: first, a model for the dynamics of $\boldsymbol{s} \in \mathbb{S}$; and second, the specification of an initial condition. Many models for dynamics exist, but usually the modeller in question has a preference, e.g., ODEs, or stochastic differential equations (SDEs). To illustrate our mathematical construction, we shall give two examples with abridged details on their analysis.

Common to both examples (and many others) is that once equations for the particle dynamics are established, one can write down a PDE for $\rho = \rho(t, \boldsymbol{s})$; where the probability (density) of observing the particle in state $\boldsymbol{s}$ at time t is given by $\rho(t, \boldsymbol{s})\mathrm{d}\boldsymbol{s}$. There are many reasons for why one may want to do this. If the particle dynamics are deterministic (e.g., dynamics given by ODEs), then one can look at the variation in sample paths by specifying the initial condition as a distribution; also one can investigate properties of the dynamics from an ergodic perspective (especially useful should the dynamics be chaotic). When the particle dynamics are stochastic, writing down a PDE allows one to specify the probability of observing the particle in some specific state without having to carry out a large number of stochastic simulations. Additionally, when stochastic dynamics involve SDEs, the dynamics can be difficult

to analyse as one is required to utilise Itô calculus. In contrast, ODEs and PDEs have a plethora of methods available to analyse their solutions.

Once we have specified what the particle dynamics are, we write an evolution equation of the form

$$\frac{\mathrm{d}\rho}{\mathrm{d}t} = \frac{\partial \rho}{\partial t} + \mathcal{L}\rho = 0\,, \tag{1.1}$$

for a linear operator $\mathcal{L}$. We require that the particle is always in some state $\boldsymbol{s} \in \mathbb{S}$ with probability 1, i.e.,

$$\int_{\mathbb{S}} \rho(t, \boldsymbol{s}) \mathrm{d}\boldsymbol{s} = 1\,, \text{ for } \rho : \mathbb{R}_+ \times \mathbb{S} \to \mathbb{R}_+\,. \tag{1.2}$$

There are many names for equation (1.1), specific scenario-dependent names include the Liouville equation, the Fokker–Planck equation, or the Kolmogorov forward equation. The most general interpretation of equation (1.1) would be as the Perron–Frobenius operator [80][4].

1.3.1.1 Particle Motion in a Potential Well

The first example we consider is a particle of unit mass in a potential well following Newton's equations of motion, in which case $\boldsymbol{s}(t) = (\boldsymbol{x}(t), \boldsymbol{v}(t)) \in \mathbb{S} \subseteq \mathbb{R}^{2d}$, and

$$\dot{\boldsymbol{x}}(t) = \boldsymbol{v}(t)\,, \quad \dot{\boldsymbol{v}}(t) = -\nabla_{\boldsymbol{x}} V(\boldsymbol{x}(t))\,. \tag{1.3}$$

The ODEs in equation (1.3) can be solved using a numerical scheme, and depending on the geometry and specifics of the model, analytic techniques may be employed.

There is a Liouville equation interpretation of equation (1.3) where one derives a PDE using the divergence theorem and imposes conservation of probability mass. For probability distribution $\rho = \rho(t, \boldsymbol{x}, \boldsymbol{v})$, the Liouville equation for the system of ODEs given in equation (1.3) is

$$\begin{aligned} \frac{\mathrm{d}\rho}{\mathrm{d}t} &= \frac{\partial \rho}{\partial t} + \nabla_{\boldsymbol{x}} \cdot (\dot{\boldsymbol{x}}\rho) + \nabla_{\boldsymbol{v}} \cdot (\dot{\boldsymbol{v}}\rho) \\ &= \frac{\partial \rho}{\partial t} + \boldsymbol{v} \cdot \nabla_{\boldsymbol{x}} \rho - \nabla_{\boldsymbol{x}} V(\boldsymbol{x}) \cdot \nabla_{\boldsymbol{v}} \rho \\ &= 0\,, \end{aligned} \tag{1.4}$$

[4] For completeness, we note that the operator $\mathcal{L}$ in equation (1.1) is the negative of the adjoint of the infinitesimal generator $\mathcal{A}$, i.e., $\langle \mathcal{L}\rho, q\rangle_{L^2} = -\langle \rho, \mathcal{A}q\rangle_{L^2}$ where $\langle \rho, q\rangle_{L^2} := \int_{\mathbb{S}} \rho q \,\mathrm{d}\boldsymbol{s}$. Equation (1.1) governs how probabilities evolve and the adjoint system (using the infinitesimal generator) governs how expectations evolve. The adjoint system is then known as either the Kolmogorov backward equation, or most generally, the Koopman operator.

with initial condition $\rho(0, \boldsymbol{x}, \boldsymbol{v}) = \rho_0(\boldsymbol{x}, \boldsymbol{v})$ and possibly boundary conditions on $\partial\mathbb{S}$. Due to the dynamics being deterministic in equation (1.3), the corresponding Liouville equation has no dispersal term[5].

1.3.1.2 Particle Motion with Stochastic Fluctuations

Our second example consists of the stochastic position jump process in which $\boldsymbol{s}(t) = \boldsymbol{X}(t) \in \mathbb{S} \subset \mathbb{R}^d$ and[6]

$$\mathrm{d}\boldsymbol{X} = \boldsymbol{\mu}(\boldsymbol{X})\mathrm{d}t + \sigma\,\mathrm{d}\boldsymbol{W}_t\,, \tag{1.5}$$

where $\boldsymbol{\mu}$ is a vector-valued function that specifies the direction of (deterministic) drift, σ is a scaling constant for the "noise" in the system, and $\boldsymbol{W}_t$ is standard Brownian motion [113]. Other examples of stochastic dynamics include velocity jump processes [114] and fractional diffusion processes [104]. Due to equation (1.5) being stochastic, a Liouville description is no longer possible, one must use a Fokker–Planck equation for the distribution of sample paths, that is for $\rho = \rho(t, \boldsymbol{x})$, then

$$\frac{\partial\rho}{\partial t} + \nabla_{\boldsymbol{x}} \cdot \left(\boldsymbol{\mu}(\boldsymbol{x}) - \frac{\sigma^2}{2}\nabla_{\boldsymbol{x}}\right)\rho = 0\,, \tag{1.6}$$

with initial condition $\rho(0, \boldsymbol{x}) = \rho_0(\boldsymbol{x})$ and potentially boundary conditions depending on $\mathbb{S}$ (usually no flux boundary conditions are used to preserve mass). Due to the stochastic nature of equation (1.5), equation (1.6) is derived using Itô calculus and has a dispersal term (second order spatial derivatives).

1.3.2 Pairwise Interactions

By allowing for multiple interacting particles, most of the mathematical construction follows as before but with multiple copies of the state space. The PDE for the distribution of sample paths then lies in a high dimensional space. The mathematical challenge is then finding a low dimensional description of the high dimensional system; this is usually done though making some mean-field closure assumption. The details below are abridged, for full details surrounding the validity of assumptions, see Refs. [30, 142].

We first consider the n particle distribution $\rho = \rho(t, \vec{s}_n)$, such that the probability of simultaneously observing all n particles with states $\vec{s}_n = \{\boldsymbol{s}_1, \ldots, \boldsymbol{s}_n\}$ at time t is

[5]Under the classifications of PDEs, equation (1.4), corresponds to a hyperbolic transport equation. Therefore all motion described by ODEs have hyperbolic transport equations, but only some stochastic motion has this property, e.g., velocity jump motion [114, 153].

[6]Following standard practice, we use capital letters for random variables and lower-case letters for realisations of these variables.

given by $\rho(t, \vec{s}_n)\mathrm{d}\vec{s}_n$. Analogously to equation (1.1), we can then write an n-particle evolution equation as

$$\frac{\mathrm{d}\rho^{(n)}}{\mathrm{d}t} = \frac{\partial\rho^{(n)}}{\partial t} + \mathcal{L}^{(n)}\rho^{(n)} = 0\,, \tag{1.7}$$

where the interactions are encoded in the $\mathcal{L}^{(n)}$ term. We also have the following normalisation

$$\int_{\mathbb{S}_n} \rho^{(n)}(t, \vec{s}_n)\mathrm{d}\vec{s}_n = \int \cdots \int_{\mathbb{S}_n} \rho^{(n)}(t, \boldsymbol{s}_1, \ldots, \boldsymbol{s}_n)\mathrm{d}\boldsymbol{s}_1 \ldots \mathrm{d}\boldsymbol{s}_n = 1\,, \tag{1.8}$$

for $\rho : \mathbb{R}_+ \times \mathbb{S}_n \to \mathbb{R}_+$. The n-particle distribution is identical with respect to pairwise particle relabelling, so for $i \neq j$

$$\rho^{(n)}(t, \boldsymbol{s}_1, \ldots, \boldsymbol{s}_i, \ldots, \boldsymbol{s}_j, \ldots, \boldsymbol{s}_n) \equiv \rho^{(n)}(t, \boldsymbol{s}_1, \ldots, \boldsymbol{s}_j, \ldots, \boldsymbol{s}_i, \ldots, \boldsymbol{s}_n)\,, \tag{1.9}$$

providing the particles are identical and equation (1.9) also holds for the initial condition. Unless specified otherwise,

$$\mathbb{S}_n = \mathbb{S}^n = \underbrace{\mathbb{S} \times \cdots \times \mathbb{S}}_{n \text{ times}}\,. \tag{1.10}$$

If there are no direct interactions between particles, then

$$\rho^{(n)}(t, \boldsymbol{s}_1, \ldots, \boldsymbol{s}_n) \equiv \prod_{k=1}^{n} \rho(t, \boldsymbol{s}_k)\,, \tag{1.11}$$

where each equation for ρ follows equation (1.1). In this case, one can then also decompose the linear $\mathcal{L}^{(n)}$ particle operator into n 1-particle $\mathcal{L}$ operators where each operator acts on one particle index.

One can calculate the q-particle distribution (the probability density of finding particles $1, \ldots, q$ with states $\vec{s}_q = \{\boldsymbol{s}_1, \ldots, \boldsymbol{s}_q\}$) by integrating over particles $q + 1, \ldots, n$ in equation (1.7), thus

$$\begin{aligned}
\rho^{(q)}(t, \vec{s}_q) &= \rho^{(q)}(t, \boldsymbol{s}_1, \ldots, \boldsymbol{s}_q) \\
&= \int \cdots \int_{\mathbb{S}_{n-q}} \rho^{(n)}(t, \boldsymbol{s}_1, \ldots, \boldsymbol{s}_n)\mathrm{d}\boldsymbol{s}_{q+1} \ldots \mathrm{d}\boldsymbol{s}_n \\
&= \int_{\mathbb{S}_{n-q}} \rho^{(n)}(t, \vec{s}_n)\mathrm{d}\vec{s}_n^{(q+1)}\,,
\end{aligned} \tag{1.12}$$

where we introduce the shorthand notation $\mathrm{d}\vec{s}_n^{(\mu)} = \mathrm{d}\boldsymbol{s}_\mu \ldots \mathrm{d}\boldsymbol{s}_n$ for $\mu \in \{1, \ldots, n\}$. We drop the superscript when $q = 1$, so $\rho^{(1)} \equiv \rho$. We can also consider the number density of particles with state vector $\vec{s}_q$ via the relation

$$f^{(q)}(t, \vec{s}_q) = \frac{n!}{(n-q)!}\rho^{(q)}(t, \vec{s}_q)\,. \tag{1.13}$$

The quantity $f^{(q)}(t, \vec{s}_q)\mathrm{d}\vec{s}_q$ indicates how many particles are in the configuration where q-particles have states $\vec{s}_q$. Equation (1.13) relies on indistinguishable particle relabelling, see equation (1.9).

If there are pairwise interactions between particles, then by integrating over particles $q+1, \ldots, n$ for all $q = 1, \ldots, n$, one generates the Bogoliubov–Born–Green–Kirkwood–Yvon (BBGKY) hierarchy, where the evolution equation for $\rho^{(q)}$ depends on $\rho^{(q+1)}$. Crucially, for $q = 1$, we wish to evaluate the term

$$\int \cdots \int_{\mathbb{S}_{n-1}} \mathcal{L}^{(n)} \rho^{(n)}(t, \boldsymbol{s}_1, \ldots, \boldsymbol{s}_n) \mathrm{d}\boldsymbol{s}_2 \ldots \mathrm{d}\boldsymbol{s}_n \,. \tag{1.14}$$

If one then approximates $\rho^{(2)}$ using the mean-field approximation

$$\rho^{(2)}(t, \boldsymbol{s}_1, \boldsymbol{s}_2) \approx \rho(t, \boldsymbol{s}_1)\rho(t, \boldsymbol{s}_2) \,, \tag{1.15}$$

then one obtains a quadratic operator which we write as $\bar{\mathcal{L}}\rho$. By calculating the quadratic operator in equation (1.14), one obtains an approximate low dimensional description of the interacting particle system, where one solves a PDE for $\rho = \rho(t, \boldsymbol{s})$:

$$\frac{\partial \rho}{\partial t} + \bar{\mathcal{L}}\rho = 0 \,. \tag{1.16}$$

In equation (1.16), we write how a single particle probability distribution evolves over time. By making the mean-field approximation in equation (1.15), we discard correlations between pairs of particles. Therefore, the second particle responds as an "average" particle, sometimes referred to as a "cloud" of particles.

We alter the examples above to now include interactions between particles, and discuss a corresponding low dimensional approximation.

1.3.2.1 Particle Motion in Pairwise Potential Well

Our example in Section 1.3.1.1 is modified to n identical particles of unit mass that follow Newton's equations of motion with a smooth pairwise potential Φ. In that case, $\boldsymbol{s}_i(t) = (\boldsymbol{x}_i(t), \boldsymbol{v}_i(t)) \in \mathbb{S} \subseteq \mathbb{R}^{2d}$ and

$$\dot{\boldsymbol{x}}_i = \boldsymbol{v}_i \,, \quad \dot{\boldsymbol{v}}_i = -\nabla_{\boldsymbol{x}_i} V(\boldsymbol{x}_1, \ldots, \boldsymbol{x}_n) \,, \tag{1.17}$$

for a potential of the form

$$V(\boldsymbol{x}_1, \ldots, \boldsymbol{x}_n) = \sum_{1 \le i < j \le n} \Phi(\boldsymbol{x}_i - \boldsymbol{x}_j) \,. \tag{1.18}$$

Variations of these equations have been used to consider collective motion such as swarming [37, 45, 71]. We first consider the n particle distribution, i.e., the probability

of simultaneously observing all n particles with positions $\vec{x}_n = \{\boldsymbol{x}_1, \ldots, \boldsymbol{x}_n\}$ and velocities $\vec{v}_n = \{\boldsymbol{v}_1, \ldots, \boldsymbol{v}_n\}$.

The high dimensional description for $\rho^{(n)} = \rho^{(n)}(t, \vec{x}_n, \vec{v}_n)$ follows the Liouville equation

$$\begin{aligned}\frac{\mathrm{d}\rho^{(n)}}{\mathrm{d}t} &= \frac{\partial \rho^{(n)}}{\partial t} + \mathcal{L}^n \rho^{(n)} \\ &= \frac{\partial \rho^{(n)}}{\partial t} + \sum_{k=1}^{n} \left(\boldsymbol{v}_i \cdot \nabla_{\boldsymbol{x}_k} - \nabla_{\boldsymbol{x}_k} V(\vec{x}_n) \cdot \nabla_{\boldsymbol{v}_k}\right) \rho^{(n)} \\ &= 0\,. \end{aligned} \tag{1.19}$$

We now demonstrate the steps necessary to obtain an equation for $\rho^{(q)}$. We now integrate equation (1.19) over positions and velocities $q+1, \ldots, n$ term by term. The partial time derivative immediately passes through the integral

$$\int_{\mathbb{S}_{n-q}} \frac{\partial \rho^{(n)}(t, \vec{x}_n, \vec{v}_n)}{\partial t} \mathrm{d}\vec{s}_n^{(q+1)} = \frac{\partial \rho^{(q)}(t, \vec{x}_q, \vec{v}_q)}{\partial t}\,. \tag{1.20}$$

For the linear operator $\mathcal{L}^{(n)}$, when integrating the flux contributions for particles $q+1, \ldots, n$, the terms disappear by the divergence theorem. For simplicity we assume that each particle's position and velocity is located in $\mathbb{R}^d$, i.e., $\mathbb{S} = \mathbb{R}^d \times \mathbb{R}^d$. For a finite state space $\mathbb{S}$ with no-flux boundary conditions, one can derive the same resulting equation but one has to be careful with regards to incoming/outgoing velocities. Therefore, for $k > q$

$$\begin{aligned}\int_{\mathbb{S}} \boldsymbol{v}_k \cdot \nabla_{\boldsymbol{x}_k} \rho^{(n)}(t, \vec{x}_n, \vec{v}_n) \mathrm{d}\boldsymbol{s}_k &= \int_{\mathbb{S}} \nabla_{\boldsymbol{x}_k} \cdot \left(\boldsymbol{v}_k \rho^{(n)}(t, \vec{x}_n, \vec{v}_n)\right) \mathrm{d}\boldsymbol{s}_k \\ &= \lim_{R\to\infty} \int_{\mathbb{R}^d} \int_{B(R)} \nabla_{\boldsymbol{x}_k} \cdot \left(\boldsymbol{v}_k \rho^{(n)}(t, \vec{x}_n, \vec{v}_n)\right) \mathrm{d}\boldsymbol{x}_k \mathrm{d}\boldsymbol{v}_k \\ &= \lim_{R\to\infty} \int_{\mathbb{R}^d} \int_{\partial B(R)} \boldsymbol{n} \cdot \boldsymbol{v}_k \rho^{(n)}(t, \vec{x}_n, \vec{v}_n) \mathrm{d}S_k \mathrm{d}\boldsymbol{v}_k \\ &= 0\,, \end{aligned} \tag{1.21}$$

for a d-dimensional ball $B(R)$ of radius R centred at the origin. Using equation (1.21), we find that

$$\int_{\mathbb{S}_{n-q}} \sum_{k=1}^{n} \boldsymbol{v}_k \cdot \nabla_{\boldsymbol{x}_k} \rho^{(n)}(t, \vec{x}_n, \vec{v}_n) \mathrm{d}\vec{s}_n^{(q+1)} = \sum_{k=1}^{q} \boldsymbol{v}_k \cdot \nabla_{\boldsymbol{x}_k} \rho^{(q)}(t, \vec{x}_q, \vec{v}_q)\,. \tag{1.22}$$

For the potential, we split the contribution into three components

$$V(\vec{x}_n) = \underbrace{\sum_{1\le i<j\le q} \Phi(\boldsymbol{x}_i - \boldsymbol{x}_j)}_{V_1(\vec{x}_q)} + \underbrace{\sum_{q+1\le i<j\le n} \Phi(\boldsymbol{x}_i - \boldsymbol{x}_j)}_{V_2(\boldsymbol{x}_{q+1}, \ldots, \boldsymbol{x}_n)} + \underbrace{\sum_{i=1}^{q} \sum_{j=q+1}^{n} \Phi(\boldsymbol{x}_i - \boldsymbol{x}_j)}_{V_3(\vec{x}_n)}\,. \tag{1.23}$$

For the first component, since $V_1 = V_1(\vec{x}_q)$ does not depend on $\boldsymbol{s}_{q+1}, \ldots, \boldsymbol{s}_n$,

$$\begin{aligned}\int_{\mathbb{S}_{n-q}} \sum_{k=1}^{n} \nabla_{\boldsymbol{x}_k} V_1(\vec{x}_q) \cdot \nabla_{\boldsymbol{v}_k} \rho^{(n)} \mathrm{d}\vec{s}_n^{(q+1)} &= \int_{\mathbb{S}_{n-q}} \sum_{k=1}^{q} \nabla_{\boldsymbol{x}_k} V_1(\vec{x}_q) \cdot \nabla_{\boldsymbol{v}_k} \rho^{(n)} \mathrm{d}\vec{s}_n^{(q+1)} \\ &= \sum_{k=1}^{q} \nabla_{\boldsymbol{x}_k} V_1(\vec{x}_q) \cdot \nabla_{\boldsymbol{v}_k} \rho^{(q)} \,. \end{aligned} \tag{1.24}$$

The second component is identically zero. The first q terms disappear by taking a gradient of a function not dependent on the first q variables $V_2 = V_2(\boldsymbol{x}_{q+1}, \ldots, \boldsymbol{x}_n)$; the final $n-q$ terms can be written as a divergence (but in velocity space). Therefore,

$$\begin{aligned}&\int_{\mathbb{S}_{n-q}} \sum_{k=1}^{n} \nabla_{\boldsymbol{x}_k} V_2(\boldsymbol{x}_{q+1}, \ldots, \boldsymbol{x}_n) \cdot \nabla_{\boldsymbol{v}_k} \rho^{(n)} \mathrm{d}\vec{s}_n^{(q+1)} \\ &= \int_{\mathbb{S}_{n-q}} \sum_{k=q+1}^{n} \nabla_{\boldsymbol{x}_k} V_2(\boldsymbol{x}_{q+1}, \ldots, \boldsymbol{x}_n) \cdot \nabla_{\boldsymbol{v}_k} \rho^{(n)} \mathrm{d}\vec{s}_n^{(q+1)} \\ &= \sum_{k=q+1}^{n} \int_{\mathbb{S}_{n-q}} \nabla_{\boldsymbol{v}_k} \cdot \left(\nabla_{\boldsymbol{x}_k} V_2(\boldsymbol{x}_{q+1}, \ldots, \boldsymbol{x}_n) \rho^{(n)} \right) \mathrm{d}\vec{s}_n^{(q+1)} \\ &= 0 \,. \end{aligned} \tag{1.25}$$

The third component uses the index permutation properties of $\rho^{(n)}$ on indices $q+1, \ldots, n$ to calculate an interaction term with the $(q+1)$-particle distribution function

$\rho^{(q+1)}$. We write

$$
\begin{aligned}
&\int_{\mathbb{S}_{n-q}} \sum_{k=1}^{n} \nabla_{\boldsymbol{x}_k} V_3(\vec{x}_n) \cdot \nabla_{\boldsymbol{v}_k} \rho^{(n)} \mathrm{d}\vec{s}_n^{(q+1)} \\
&= \int_{\mathbb{S}_{n-q}} \sum_{k=1}^{n} \nabla_{\boldsymbol{x}_k} \sum_{i=1}^{q} \sum_{j=q+1}^{n} \Phi(\boldsymbol{x}_i - \boldsymbol{x}_j) \cdot \nabla_{\boldsymbol{v}_k} \rho^{(n)} \mathrm{d}\vec{s}_n^{(q+1)} \text{ (by definition)} \\
&= \int_{\mathbb{S}_{n-q}} \sum_{k=1}^{q} \nabla_{\boldsymbol{x}_k} \sum_{j=q+1}^{n} \Phi(\boldsymbol{x}_k - \boldsymbol{x}_j) \cdot \nabla_{\boldsymbol{v}_k} \rho^{(n)} \mathrm{d}\vec{s}_n^{(q+1)} \\
&\quad + \int_{\mathbb{S}_{n-q}} \sum_{k=q+1}^{n} \nabla_{\boldsymbol{x}_k} \sum_{i=1}^{q} \Phi(\boldsymbol{x}_i - \boldsymbol{x}_k) \cdot \nabla_{\boldsymbol{v}_k} \rho^{(n)} \mathrm{d}\vec{s}_n^{(q+1)} \text{ (split up sum)} \\
&= \int_{\mathbb{S}_{n-q}} \sum_{k=1}^{q} \nabla_{\boldsymbol{x}_k} \sum_{j=q+1}^{n} \Phi(\boldsymbol{x}_k - \boldsymbol{x}_j) \cdot \nabla_{\boldsymbol{v}_k} \rho^{(n)} \mathrm{d}\vec{s}_n^{(q+1)} \\
&\quad + \sum_{k=q+1}^{n} \int_{\mathbb{S}_{n-q}} \nabla_{\boldsymbol{v}_k} \cdot \left(\nabla_{\boldsymbol{x}_k} \sum_{i=1}^{q} \Phi(\boldsymbol{x}_i - \boldsymbol{x}_k) \rho^{(n)} \right) \mathrm{d}\vec{s}_n^{(q+1)} \text{ (identify divergence)} \\
&= (n-q) \sum_{k=1}^{q} \int_{\mathbb{S}_{n-q}} \nabla_{\boldsymbol{x}_k} \Phi(\boldsymbol{x}_k - \boldsymbol{x}_{q+1}) \cdot \nabla_{\boldsymbol{v}_k} \rho^{(n)} \mathrm{d}\vec{s}_n^{(q+1)} \text{ (relabel particles)} \\
&= (n-q) \sum_{k=1}^{q} \int_{\mathbb{S}} \nabla_{\boldsymbol{x}_k} \Phi(\boldsymbol{x}_k - \boldsymbol{x}_{q+1}) \cdot \nabla_{\boldsymbol{v}_k} \left[\int_{\mathbb{S}_{n-q-1}} \rho^{(n)} \mathrm{d}\vec{s}_n^{(q+2)} \right] \mathrm{d}\boldsymbol{s}_{q+1} \text{ (rearrange)} \\
&= (n-q) \sum_{k=1}^{q} \int_{\mathbb{S}} \nabla_{\boldsymbol{x}_k} \Phi(\boldsymbol{x}_k - \boldsymbol{x}_{q+1}) \cdot \nabla_{\boldsymbol{v}_k} \rho^{(q+1)} \mathrm{d}\boldsymbol{s}_{q+1} \text{ (identify term)} \,. \qquad (1.26)
\end{aligned}
$$

Putting this altogether, we find

$$
\begin{aligned}
&\frac{\partial \rho^{(q)}}{\partial t} + \sum_{k=1}^{q} \left(\boldsymbol{v}_k \cdot \nabla_{\boldsymbol{x}_k} - \nabla_{\boldsymbol{x}_k} V_1(\vec{x}_q) \cdot \nabla_{\boldsymbol{v}_k} \right) \rho^{(q)} \\
&\qquad = (n-q) \sum_{k=1}^{q} \int_{\mathbb{S}} \nabla_{\boldsymbol{x}_k} \Phi(\boldsymbol{x}_k - \boldsymbol{x}_{q+1}) \cdot \nabla_{\boldsymbol{v}_k} \rho^{(q+1)} \mathrm{d}\boldsymbol{s}_{q+1} \,. \qquad (1.27)
\end{aligned}
$$

Equation (1.27) is called the BBGKY hierarchy. For the case where $q = 1$, equation (1.27) becomes

$$
\left(\frac{\partial}{\partial t} + \boldsymbol{v}_1 \cdot \nabla_{\boldsymbol{x}_1} \right) \rho(t, \boldsymbol{x}_1, \boldsymbol{v}_1) = (n-1) \int_{\mathbb{S}} \nabla_{\boldsymbol{x}_1} \Phi(\boldsymbol{x}_1 - \boldsymbol{x}_2) \cdot \nabla_{\boldsymbol{v}_1} \rho^{(2)}(t, \boldsymbol{x}_1, \boldsymbol{x}_2, \boldsymbol{v}_1, \boldsymbol{v}_2) \mathrm{d}\boldsymbol{s}_2 \,. \qquad (1.28)
$$

By making the mean-field closure assumption in equation (1.15), our quadratic low dimensional approximation in equation (1.16) is

$$
\bar{\mathcal{L}}^{(1)} \rho = \boldsymbol{v} \cdot \nabla_{\boldsymbol{x}} \rho - \mathcal{B}(\rho, \rho) \,, \qquad (1.29)
$$

where $\mathcal{B}(\rho,\rho)$ is the Vlasov mean-field approximation

$$\mathcal{B}(\rho,\rho) = (n-1)\left(\nabla_{\boldsymbol{x}}\Phi * \int_{\mathbb{R}^d} \rho \,\mathrm{d}\boldsymbol{v}\right)\cdot(\nabla_{\boldsymbol{v}}\rho)\ , \tag{1.30}$$

and $*$ represents the convolution operator. When there are excluded volume effects of the form

$$\mathbb{S}_n = \{(\boldsymbol{s}_1,\ldots,\boldsymbol{s}_n)\in\mathbb{S}\times\cdots\times\mathbb{S} : \|\boldsymbol{x}_i-\boldsymbol{x}_j\|\geq\epsilon \text{ for all } i\neq j\}\ , \tag{1.31}$$

one has to be careful when using the mean-field approximation (now termed the molecular chaos assumption), and one derives the famous Boltzmann collision operator

$$\mathcal{B}(\rho,\rho) = \kappa\int_{\mathbb{R}^d}\int_{S_-} B(\boldsymbol{v}'-\boldsymbol{v},\boldsymbol{n})[\rho(t,\boldsymbol{x},\boldsymbol{v}_*)\rho(t,\boldsymbol{x},\boldsymbol{v}'_*)-\rho(t,\boldsymbol{x},\boldsymbol{v})\rho(t,\boldsymbol{x},\boldsymbol{v}')]\mathrm{d}\boldsymbol{n}\mathrm{d}\boldsymbol{v}'. \tag{1.32}$$

In equation (1.32) S_- is the half unit-disc/ball of incoming particle collisions, $\kappa = (n-1)\epsilon^{d-1}$ is the Boltzmann collision constant, and $(\boldsymbol{v}_*,\boldsymbol{v}'_*)$ are the new velocities after particles with velocities $(\boldsymbol{v},\boldsymbol{v}')$ undergo a collision. The scattering kernel B and velocity variables with asterisks are determined by conservation laws, e.g., conservation of momentum and energy.

1.3.2.2 Particle Motion with Stochastic Fluctuations and Pairwise Potential Well

For particles in Section 1.3.1.2, the motion remains the same, i.e., each particle follows the stochastic position jump process in which $\boldsymbol{s}_i(t) = \boldsymbol{X}_i(t)\in\mathbb{S}\subset\mathbb{R}^d$ and

$$\mathrm{d}\boldsymbol{X}_i = \boldsymbol{\mu}_i(\boldsymbol{X}_1,\ldots,\boldsymbol{X}_n)\mathrm{d}t + \sigma\,\mathrm{d}\boldsymbol{W}_t\,, \tag{1.33}$$

where $\boldsymbol{W}_t$ is standard Brownian motion. However, we suppose that the forcing term $\boldsymbol{\mu}_i$ is due to a pairwise potential well, we write

$$\boldsymbol{\mu}_i = -\nabla_{\boldsymbol{x}_i}V(\boldsymbol{X}_1,\ldots,\boldsymbol{X}_n) = -\nabla_{\boldsymbol{x}_i}\sum_{1\leq i<j\leq n}\Phi(\boldsymbol{X}_i-\boldsymbol{X}_j)\,. \tag{1.34}$$

If $\boldsymbol{s}_i(t)$ evolves according to equation (1.33), one has the Fokker–Planck equation

$$\begin{aligned}\frac{\mathrm{d}\rho^{(n)}}{\mathrm{d}t} &= \frac{\partial\rho^{(n)}}{\partial t} + \mathcal{L}^n\rho^{(n)}\\ &= \frac{\partial\rho^{(n)}}{\partial t} + \sum_{k=1}^{n}\nabla_{\boldsymbol{x}_k}\cdot\left(\boldsymbol{\mu}_k(\boldsymbol{x}_k)-\frac{\sigma^2}{2}\nabla_{\boldsymbol{x}_k}\right)\rho^{(n)}\\ &= 0\,.\end{aligned} \tag{1.35}$$

Following the same analysis as in Section 1.3.2.1, we obtain the following BBGKY hierarchy

$$\frac{\partial \rho^{(q)}}{\partial t} - \sum_{k=1}^{q} \nabla_{\boldsymbol{x}_k} \cdot \left(\nabla_{\boldsymbol{x}_k} V_1(\vec{x}_q) + \frac{\sigma^2}{2} \nabla_{\boldsymbol{x}_k} \right) \rho^{(q)} = (n-q) \sum_{k=1}^{q} \int_{\mathbb{R}^d} \nabla_{\boldsymbol{x}_k} \Phi(\boldsymbol{x}_k - \boldsymbol{x}_{q+1}) \cdot \nabla_{\boldsymbol{x}_k} \rho^{(q+1)} \mathrm{d}\boldsymbol{x}_{q+1} \,. \tag{1.36}$$

For $q = 1$, equation (1.36) becomes

$$\left(\frac{\partial}{\partial t} - \frac{\sigma^2}{2} \nabla^2_{\boldsymbol{x}_1} \right) \rho(t, \boldsymbol{x}_1) = (n-1) \int_{\mathbb{R}^d} \nabla_{\boldsymbol{x}_1} \Phi(\boldsymbol{x}_1 - \boldsymbol{x}_2) \cdot \nabla_{\boldsymbol{x}_1} \rho^{(2)}(t, \boldsymbol{x}_1, \boldsymbol{x}_2) \mathrm{d}\boldsymbol{x}_2 \,. \tag{1.37}$$

Therefore, after making the mean-field approximation in equation (1.15), we find that the quadratic operator in equation (1.16) is

$$\bar{\mathcal{L}}^{(1)} \rho = -\frac{\sigma^2}{2} \nabla^2_{\boldsymbol{x}} \rho - (n-1) \nabla_{\boldsymbol{x}} \rho \cdot \nabla_{\boldsymbol{x}} (\rho * \Phi) \,. \tag{1.38}$$

For the case where particles have finite volume effects with the state space in equation (1.31), a low dimensional description was calculated by Bruna and Chapman [19] using matched asymptotic expansions (for small ϵ) to give

$$\bar{\mathcal{L}}^{(1)} \rho = -\frac{\sigma^2}{2} \nabla^2_{\boldsymbol{x}} \left[\rho + \alpha_d (n-1) \epsilon^d \rho^2 \right] \,, \tag{1.39}$$

for $\alpha_2 = \pi/2$ and $\alpha_3 = 2\pi/3$.

Thus far, we have used the probabilistic normalisation as opposed to the number normalisation, i.e., using the distribution ρ as opposed to distribution $f = n\rho$. In Chapter 2, it will become necessary to use f as we wish to consider systems which change size. Notice there is an $(n-1)$ coefficient to the quadratic interaction terms. Therefore, if we approximate $n \approx n - 1$, then one uses $f = n\rho$ and one has an expression in f only.

※

We have now introduced the relevant biology and mathematical concepts that will be referred to throughout the thesis. In order to develop a model of osteocyte network formation, we need a consistent mathematical framework that addresses the concerns in Section 1.1.5. In Chapter 2, we use some of the ideas from interacting particle systems in Section 1.3 to derive differential equations to investigate a wide range of

evolving network problems. In Chapter 3, we build a stochastic agent-based model of bone formation, and use the modelling framework in Chapter 2 to analyse the mean-field behaviour. In Chapter 4, we change topic to histology analysis, where we develop a method to analyse paracrine signalling based on histology slides. We then tie this back into interacting particle systems and show that our model can be seen as cells communicating via a signalling field located within the extracellular space. Finally, in Chapter 5, we discuss the work from the thesis and consider strengths, shortfalls, and the (many) future avenues that this work could take.

Chapter 2

A Mean-Field Approach to Evolving Spatial Networks

This chapter is organised as follows. In Section 2.1, we give a review on networks and models of their creation. In Section 2.2, we define the concept of a "local state degree distribution" (LSDD), which encapsulates the degree distribution of a network local to a point in state space. In Section 2.3, we give a description of our model of evolving spatial networks. In Section 2.4, we derive an equation for the LSDD when edges are created but cannot be destroyed. In Section 2.5, we incorporate edge destruction into our model. Our derivations require the use of approximations, so we use numerical simulations to explore agreement and discrepancies between theory and our derived equations in Section 2.6.

2.1 Introduction

Networks, in which entities ("nodes") interact with each other via "edges", are a useful representation of complex systems [109]. They have often been very helpful for formulating and answering questions in biology, sociology, engineering, and numerous other fields. Many systems—such as blood vasculature [74], leaf venation [15], and fungi [63, 90]—can be treated as biological transportation networks, in which edges carry resources and nodes operate as junctions. Some of these studies exploit ideas from fluid mechanics and energy minimisation to investigate flow through various media [61, 63, 68, 111]. To give another type of example, in evolutionary game theory, a node can represent a biological agent, and edges indicate interactions in a "game" between those agents [150]. Applications range from behavioural ecology [141] to investigating tumour heterogeneity in cancer [8]. Changes in node fitness can depend on, for example, a node's phenotype and its immediate neighbours [112].

Many of the above examples involve "spatial networks" [11], and spatial constraints can exert significant influence (directly and/or indirectly) on both network structure and function. In the aforementioned examples, the networks are embedded in space, and one thus can assign physical locations to the nodes and edges. This is clearly important when considering dynamical processes on those networks [40].

Some spatial networks grow in time as they form: new nodes and edges can join a spatial network, and the spatial domain can expand. For example, cities often grow outwards or arise when borders from multiple settlements coalesce [12, 46, 94]. Fungi, which are living networks, expand to reach nutrients, and such growth induces flows of mass [63, 90].

There are myriad models of network formation [109]. There are at least three possible ways of formulating such a model: (*i*) all nodes and edges are created simultaneously with a single algorithmic step (e.g., the standard Erdős–Rényi (ER) random graph $G(n, p)$ [42, 109] and standard random geometric graphs [122]); (*ii*) nodes and edges have an implicit order of creation but time is not considered explicitly (e.g., in some preferential-attachment models [106, 129]); or (*iii*) nodes and edges have an order of creation and time is considered explicitly (e.g., in some preferential-attachment models [83, 85] and in adaptive network models [56]). Because we want to incorporate time explicitly, we will consider spatial networks in category (*iii*). See also the recent work by Zuev et al. on geometric preferential-attachment models [170].

When studying a model in category (*iii*), it is common to employ kinetic approximations [83–85, 98]. Such approximations often allow one to construct a "master equation" to obtain approximate and/or asymptotic expressions for quantities such as degree distributions, component sizes, and cycle sizes [84]. These equations can take the form of an ordinary differential equation (ODE), partial differential equation (PDE), or other continuous model. By carefully constructing a general state space of the system, we derive an extension to the ODE master equations given in [83–85, 98] to obtain a master equation in the form of an integro-partial differential equation (IPDE) that incorporates this state space.

Our work illustrates how to use a master-equation approach to study spatial networks. As an illustration of its potential, we examine degree distributions in a very general model of evolving spatial networks and in Chapter 3 use our results to gain insights on osteocyte network formation in bone. An important benefit of using an explicit time-dependent kinetic approach is that it allows one to incorporate nodes that move through a state space (e.g., particles that diffuse). Note that we will often use the terms "nodes" and "particles" interchangeably (depending on the context).

When considering spatially-embedded network models, the state space corresponds to each node being located in a copy of the physical space. From a mathematical viewpoint, our approach is reminiscent of some models of social networks [17, 162], for which the state space corresponds to a latent social space described by some internal parameters; however, these models have no time dependence.

2.2 A Local State Degree Distribution

We consider networks in which each node (i.e., particle) has some number of associated properties in addition to those, such as degree distribution, that arise from network structure. For example, each node may have a spatial location and a velocity, or it may have some more abstract internal ("latent") property describing, for example, some social trait. We collect these properties together into a state vector $\boldsymbol{s}$, which belongs to a state space $\mathbb{S}$.

The density $f(t, \boldsymbol{s})$ of particles in the state space gives the expected number of particles with state[1] $\boldsymbol{s}$. However, a common way to study the properties of models of network formation is to examine the degree distribution [109]. In this chapter, we combine these ideas to consider what we call a *local state degree distribution* (LSDD) $u_k(t, \boldsymbol{s})$, which gives the expected number of particles of degree k at time t with state vector $\boldsymbol{s}$. One can write the LSDD as

$$u_k(t, \boldsymbol{s}) = p_k(t \,|\, \boldsymbol{s}) f(t, \boldsymbol{s}) \,,$$

where $p_k(t \,|\, \boldsymbol{s})$ is the conditional probability that a node at time t has degree k, given that its state is $\boldsymbol{s}$. We can recover both f and p_k from u_k via

$$f(t, \boldsymbol{s}) = \sum_{k=0}^{\infty} u_k(t, \boldsymbol{s}) \,, \quad p_k(t \,|\, \boldsymbol{s}) = \frac{u_k(t, \boldsymbol{s})}{\sum_{k=0}^{\infty} u_k(t, \boldsymbol{s})} \,. \tag{2.1}$$

The degree distribution of the whole network is given by

$$P_k(t) = \frac{\int_{\mathbb{S}} u_k(t, \boldsymbol{s}) \mathrm{d}\boldsymbol{s}}{\sum_{k=0}^{\infty} \int_{\mathbb{S}} u_k(t, \boldsymbol{s}) \mathrm{d}\boldsymbol{s}} \,. \tag{2.2}$$

2.3 Model of Evolving Spatial Networks

We now present a model for evolving spatial networks. Our model has three tuneable features. First, edges can be created and deleted. Second, new nodes can be created

[1] More precisely, $f(t, \boldsymbol{s})\mathrm{d}\boldsymbol{s}$ gives the expected number of particles that have states lying in the volume element $\mathrm{d}\boldsymbol{s}$ centred on $\boldsymbol{s}$.

(but we do not allow node deletion). Finally, we specify a model (possibly depending on network structure) for the evolution of the state $\boldsymbol{s}$ of each node.

Suppose at time t that there are $N(t)$ nodes with state vectors $\boldsymbol{s}_i$ and degrees k_i (with $i \in \{1, \ldots, N\}$). We suppose that new edges are created between each pair of nodes as independent Poisson processes, where $\mathcal{C}(\boldsymbol{s}_i, k_i, \boldsymbol{s}_j, k_j)$ is the rate of edge creation between node i and node j, so that the probability of an edge being created between node i and node j in time t to $t + \mathrm{d}t$ is $\mathcal{C}(\boldsymbol{s}_i, k_i, \boldsymbol{s}_j, k_j)\mathrm{d}t$. We suppose that $\mathcal{C}$ depends on the states and degrees of the two nodes i and j, but that it does not depend on other properties of the network (such as, for example, whether an edge between node i and node j already exists). Thus, our model allows *multiedges* (i.e., multiple edges between two distinct nodes).

Similarly, we suppose that existing nodes are deleted as independent Poisson processes, where $\mathcal{D}(\boldsymbol{s}_i, k_i, \boldsymbol{s}_j, k_j)$ is the rate of edge deletion (per edge) between node i and node j. We suppose also that new particles, which have degree 0, arrive randomly as a Poisson process with constant rate $\mathcal{J}$, and we assign to them a state drawn at random from the probability distribution $\mathcal{K}$.

The final component of our model is the equation of motion of the particles in the state space. Many possible models are available (both deterministic and stochastic); for examples of these, refer back to Section 1.3. For the examples in Section 1.3, the motion in state space is independent of network structure. Of course, it is also possible to imagine scenarios in which the motion depends on node degree or other structural features.

We summarise the model events and state update in Table 2.1, and we illustrate them in Figure 2.1. In Algorithm 1, we give pseudocode for our simulations of evolving spatial networks.

When simulating Algorithm 1, we use a small time step Δt, so $0 < \Delta t \ll 1$. We also specify the following ordering of events: edge creation; edge deletion; state update; and then new particles are allowed to enter the system. This specification is arbitrary, and obviously it is desirable that any reordering of these events becomes inconsequential as $\Delta t \to 0$. For our numerical experimentation using the examples in Section 2.6, this indeed appears to be the case. For the simulations that we report in Section 2.6, we chose a time step Δt to be sufficiently small that a reordering of events has no discernible impact.

The update rule for event (*iv*) in Table 2.1—namely, the evolution of the states of the individual nodes—depends on the particular process that we consider. We write $\boldsymbol{s}_i(t + \Delta t) = \mathscr{D}(\boldsymbol{s}_1(t), \ldots, \boldsymbol{s}_{N(t)}(t), \Delta t)$, where $\mathscr{D}$ arises from the time-discretisation of

Table 2.1: Model description: (*i*) edge creation; (*ii*) edge deletion; (*iii*) node creation; and (*iv*) evolution of node state.

(*i*) The rate of edge creation between nodes i and j is $\mathcal{C}(\boldsymbol{s}_i, k_i, \boldsymbol{s}_j, k_j)$.
(*ii*) The rate of edge deletion per edge between nodes i and j is $\mathcal{D}(\boldsymbol{s}_i, k_i, \boldsymbol{s}_j, k_j)$.
(*iii*) Nodes of degree 0 enter the system at rate $\mathcal{J}$. We assign the new node a state $\boldsymbol{s}^* \in \mathbb{S}$, where we draw $\boldsymbol{s}^*$ from the distribution $\mathcal{K}$.
(*iv*) Nodes move in the state space $\mathbb{S}$ according to some (possibly stochastic) differential equation. We specify a single differential equation for each node, and all nodes must follow the same differential equation.

the underlying process. For example, one can use an Euler–Maruyama method or the Milstein method for the SDE (1.33) [65]; and one can use Störmer–Verlet schemes for the ODEs in equation (1.17) [57].

One can devise a efficient simulation algorithm for situations in which edge creation or deletion do not depend on the state of nodes. In that case, one can use an event-driven algorithm, such as a Gillespie algorithm [51], for creation and deletion events.

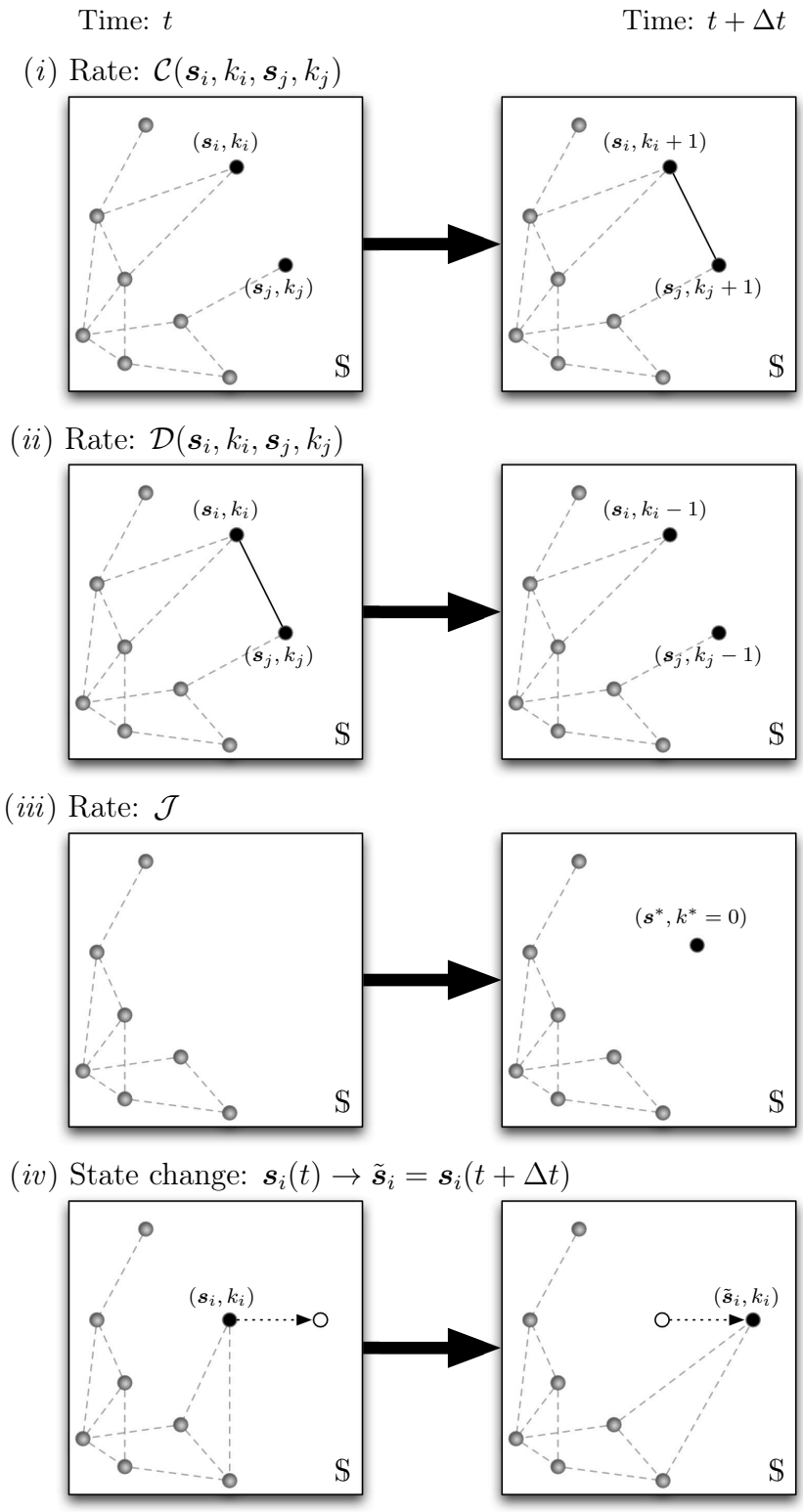

Figure 2.1: Diagrammatic illustration of our model of evolving spatial networks. In each panel, the square box represents the state space $\mathbb{S}$. In each time step of size Δt (where $0 < \Delta t \ll 1$), the following events can occur: (i) edge creation; (ii) edge deletion; (iii) node creation; and (iv) evolution of node state.

Algorithm 1: Algorithm to generate an evolving spatial network. The notation $\texttt{randperm}(X)$ signifies a permutation, selected uniformly at random, of the discrete set X.

Data: Choose an end time $T_{\text{end}} = M\Delta t$ for large $M \in \mathbb{N}$ and small $\Delta t > 0$.
Set the number of particles $N \leftarrow N_0$.
Initialise the starting state at $\boldsymbol{s}_i \leftarrow \boldsymbol{s}_0^{(i)}$ and starting degree at $k_i \leftarrow k_0^{(i)}$ for each $i \in \{1, \dots, N_0\}$.
Set time counter $m \leftarrow 0$.
while $m \leq M$ **do**
  %Edge creation update.
  for $i \leftarrow \texttt{randperm}(\{1, 2, \dots, N\})$ **do**
    for $j \leftarrow \texttt{randperm}(\{i+1, \dots, N\})$ **do**
      Draw a uniform random number r_1 from the distribution $\mathcal{U}(0,1)$.
      if $r_1 \leq \mathcal{C}(\boldsymbol{s}_j, k_j | \boldsymbol{s}_i, k_i)\Delta t$ **then**
        Create an edge between node i and node j.
  %Edge deletion update.
  for $i \leftarrow \texttt{randperm}(\{1, 2, \dots, N\})$ **do**
    for $j \leftarrow \texttt{randperm}(E_i)$ **do** *%E_i is the set nodes joined by an edge to i, counted according to multiplicity.*
      Draw a uniform random number r_2 from the distribution $\mathcal{U}(0,1)$.
      if $r_2 \leq \mathcal{D}(\boldsymbol{s}_j, k_j | \boldsymbol{s}_i, k_i)\Delta t$ **then**
        Delete an edge between node i and node j.
  %State update.
  for $i \leftarrow 1$ **to** N **do**
    Update particle state: $\boldsymbol{s}_i \leftarrow \mathscr{D}(\boldsymbol{s}_1, \dots, \boldsymbol{s}_N, \Delta t)$. *%$\mathscr{D}$ arises from the time-discretisation of the state dynamics*
  %New node creation.
  Draw a uniform random number r_3 from the distribution $\mathcal{U}(0,1)$.
  if $r_3 \leq \mathcal{J}\Delta t$ **then**
    Create node with state $\boldsymbol{s}_{N+1} \leftarrow \boldsymbol{s}^*$, where $\boldsymbol{s}^* \sim \mathcal{K}$.
    Initialise the degree $k_{N+1} \leftarrow 0$
    Update the number of particles: $N \leftarrow N + 1$.
  Update time: $m \leftarrow m + 1$.

Our model treats all nodes identically, although our methodology can be extended to heterogeneous classes of nodes or heterogeneous classes of edges. (Both of these generalisations are examples of multilayer networks [79].) To consider such cases, one can modify kinetic methodology from [14, 23].

2.4 Model Derivation: No Edge Deletion

We begin by considering the case in which there is no edge deletion. That is $\mathcal{D} = 0$ for all $\boldsymbol{s}_i, k_i, \boldsymbol{s}_j, k_j$. In the next subsection, we give a set of hierarchical master Fokker–Planck (FP) equations for the probability distribution of the state of the system. Because it is not pragmatic to work in this high-dimensional space, in Section 2.4.2,

we reduce the dimension using mean-field arguments from kinetic theory.

2.4.1 Fokker–Planck Equation

We define $\mathscr{P}_n^{\vec{k}_n}(t, \vec{s}_n)$ to be the probability that a network has n nodes with degree sequence $\vec{k}_n = \{k_1, \ldots, k_n\}$ and state vectors $\vec{s}_n = \{\boldsymbol{s}_1, \ldots, \boldsymbol{s}_n\}$. Note the normalisation

$$\sum_{n=0}^{\infty} \left\{ \sum_{K_{1,n}} \left[\int_{\mathbb{S}^n} \mathscr{P}_n^{\vec{k}_n}(t, \vec{s}_n) \, \mathrm{d}\vec{s}_n \right] \right\} = 1 \,, \tag{2.3}$$

where $K_{a,b}$ is shorthand for summing over all possible degrees for nodes $i \in \{a, a+1, \ldots, b\}$. That is,

$$\sum_{K_{a,b}} \equiv \sum_{k_a=0}^{\infty} \sum_{k_{a+1}=0}^{\infty} \cdots \sum_{k_b=0}^{\infty} . \tag{2.4}$$

We note that existence of a network with arbitrary degree sequence $\vec{k}_n$ is not guaranteed, in which case we assume that the associated probability of observing the network is zero for all state vectors $\vec{s}_n$, i.e., $\mathscr{P}_n^{\vec{k}_n}(t, \vec{s}_n) = 0$ for all $\vec{s}_n \in \mathbb{S}^n$.

We are not considering edge deletion and we have assumed that edge creation and state-space motion depend only on node state and degree, so it is possible to write down a closed equation for $\mathscr{P}_n^{\vec{k}_n}(t, \vec{s}_n)$. In contrast, when we do consider edge deletion in Section 2.5, it will not be enough simply to keep track of node degrees. We will need the full adjacency matrix.

Because the probability density function $\mathscr{P}_n^{\vec{k}_n}(t, \vec{s}_n)$ depends on the number of particles in the system (which changes when new nodes are created), we obtain a hierarchy of Fokker–Planck equations as in [31]. By considering a small time step from t to $t + \mathrm{d}t$ and partitioning over the events that can occur, we obtain

$$\begin{aligned}
&\left(\frac{\partial}{\partial t} + \mathcal{L}^{(n)} \right) \mathscr{P}_n^{\vec{k}_n}(t, \vec{s}_n) \\
&= \sum_{1 \le i < j \le n} \left(\mathcal{C}(\boldsymbol{s}_i, k_i - 1, \boldsymbol{s}_j, k_j - 1) \mathscr{P}_n^{\vec{k}_{n,-}^{i,j}}(t, \vec{s}_n) - \mathcal{C}(\boldsymbol{s}_i, k_i, \boldsymbol{s}_j, k_j) \mathscr{P}_n^{\vec{k}_n}(t, \vec{s}_n) \right) \\
&+ \sum_{i=1}^{n} \frac{1}{n} \delta_{k_i,0} \, \mathcal{J} \, \mathcal{K}(\boldsymbol{s}_i) \mathscr{P}_{n-1}^{\vec{k}_n^{i-}}(t, \vec{s}_n^{i-}) - \mathcal{J} \mathscr{P}_n^{\vec{k}_n}(t, \vec{s}_n) \,.
\end{aligned} \tag{2.5}$$

The operator on the left-hand side describes the evolution of particles in state space, and it depends on the particular model that one chooses for this evolution. For examples of these evolution operators, see Section 1.3. If the states of nodes are static, then $\mathcal{L}^{(n)} \equiv 0$.

The first term in parentheses on the right-hand side of equation (2.5) corresponds to edge-creation events between each pair, i and j, of nodes. The positive term corresponds to gaining a network with degree sequence $\vec{k}_n = \{k_1, \ldots, k_n\}$ from a network with degree sequence $\vec{k}_{n,-}^{i,j} = \{k_1, \ldots, k_i - 1, \ldots, k_j - 1, \ldots, k_n\}$ by adding an

edge between nodes i and j. The negative term corresponds to losing a network of degree sequence $\vec{k}_n$ (as it changes to a network of degree sequence $\vec{k}_{n,+}^{i,j} = \{k_1, \ldots, k_i + 1, \ldots, k_j + 1, \ldots, k_n\}$) by adding an edge between nodes i and j.

The second term on the right-hand side of equation (2.5) corresponds to gaining a network with degree sequence $\{k_1, \ldots, k_{i-1}, 0, k_{i+1}, \ldots, k_n\}$ from a network with degree sequence $\vec{k}_n^{i-} = \{k_1, \ldots, k_{i-1}, k_{i+1}, \ldots, k_{n-1}\}$ by adding a new node (of degree 0) to the system. The Kronecker delta $\delta_{k_i,0}$ ensures that this term is present only when $k_i = 0$, corresponding to the new node having degree 0. One draws the new state $\boldsymbol{s}_i$ from the probability distribution with density function $\mathcal{K}$. (The state vector of the existing nodes is $\vec{s}_n^{i-} = (\boldsymbol{s}_1, \ldots, \boldsymbol{s}_{i-1}, \boldsymbol{s}_{i+1}, \ldots, \boldsymbol{s}_n)$.) We assign the label of the new node uniformly at random from the set $\{1, \ldots, n\}$ (rather than assigning it to be the last node n) to ensure that particles are indistinguishable. Hence the factor $1/n$.

The final term on the right-hand side of equation (2.5) describes the loss of a network with degree sequence $\vec{k}_n$ because of the addition of a new node. (One thereby obtains a network with degree sequence $\{k_1, \ldots, k_{i-1}, 0, k_i, \ldots, k_n\}$ for some i.)

To save us from writing down separate equations for each case in which $k_i = 0$ for some i (because it is impossible to arrive at a state in which a node has degree 0 by adding an edge to a state in which it has degree -1), we use the convention that $\mathscr{P}_n^{\vec{k}_n}(t, \vec{s}_n) = 0$ if $n < 0$ or $k_i < 0$ for all $i \in \{0, 1, \ldots, n\}$. We also suppose that particles are indistinguishable initially, so the initial condition $\mathscr{P}_n^{\vec{k}_n}(0, \vec{s}_n)$ is invariant to index permutation. Equation (2.5) then ensures that this is true for all t.

It is not feasible to solve equation (2.5) analytically (except perhaps when the node state vectors are uncorrelated), and it is not practical to solve it numerically due to the infinite number of copies of the state space (see Section 1.3.2). In Section 2.4.2, we reduce the dimension of the equation (2.5) using mean-field approaches from kinetic theory.

2.4.2 Low-Dimensional Approximation

To derive our low-dimensional approximation, we adapt methods from kinetic theory [25, 37]. A common approach in kinetic theory is to average over the states of particles 2 to n to find an equation for the marginal distribution function of the first particle [29, 59] (the so-called "1-particle distribution function"). Because particles are indistinguishable, multiplying by n gives the probability of finding *any* particle in a given state. Here we adopt the same approach, and we average over the states and degrees of particles 2 to n. Because the number of particles itself can vary, we also need to average over this quantity. The resulting 1-particle distribution function is exactly the previously-defined LSDD $u_{k_1}(t, \boldsymbol{s}_1)$. Specifically,

$$\begin{aligned} u_{k_1}(t, \boldsymbol{s}_1) &= \sum_{n=0}^{\infty} n \sum_{k_2=0}^{\infty} \cdots \sum_{k_n=0}^{\infty} \int_{\mathbb{S}^{n-1}} \mathscr{P}_n^{\vec{k}_n}(t, \boldsymbol{s}_1, \ldots, \boldsymbol{s}_n) \, \mathrm{d}\boldsymbol{s}_2 \ldots \mathrm{d}\boldsymbol{s}_n \\ &= \sum_{n=0}^{\infty} n \sum_{K_{2,n}} \int_{\mathbb{S}^{n-1}} \mathscr{P}_n^{\vec{k}_n}(t, \vec{s}_n) \, \mathrm{d}\vec{s}_n^{(2)}, \end{aligned} \tag{2.6}$$

where we remind the reader of the shorthand notation $\mathrm{d}\vec{s}_n^{(\mu)} = \mathrm{d}\boldsymbol{s}_\mu \dots \mathrm{d}\boldsymbol{s}_n$ for $\mu \in \{1, \dots, n\}$.

To find the equation satisfied by $u_{k_1}(t, \boldsymbol{s}_1)$, we apply the same summation and integration to the Fokker–Planck equation (2.5).

Because the summation and integration commutes with the time derivative, it follows for the first term on the left-hand side (LHS) of equation (2.5) that

$$\sum_{n=0}^{\infty} n \sum_{K_{2,n}} \int_{\mathbb{S}^{n-1}} \frac{\partial \mathscr{P}_n^{\vec{k}_n}(t, \vec{s}_n)}{\partial t} \, \mathrm{d}\vec{s}_n^{(2)} = \frac{\partial u_{k_1}(t, \boldsymbol{s}_1)}{\partial t} \,. \tag{2.7}$$

For the next term on the LHS, we need to evaluate

$$\sum_{n=0}^{\infty} n \sum_{K_{2,n}} \int_{\mathbb{S}^{n-1}} \mathcal{L}^{(n)} \mathscr{P}_n^{\vec{k}_n} \, \mathrm{d}\vec{s}_n^{(2)} \,. \tag{2.8}$$

For specific examples of the resulting operator (which lack dependence on network structure), see Section 1.3. As a quick reminder, when there are pairwise interactions between particles in the state space, for each interacting pair, one can perform the integration over all other particles. Consequently, after relabelling, one can write (2.8) in terms of the 2-particle LSDD

$$u^{(2)}_{k_1,k_2}(t, \boldsymbol{s}_1, \boldsymbol{s}_2) = \sum_{n=0}^{\infty} n(n-1) \sum_{K_{3,n}} \int_{\mathbb{S}^{n-2}} \mathscr{P}_n^{\vec{k}_n}(t, \vec{s}_n) \, \mathrm{d}\vec{s}_n^{(3)}. \tag{2.9}$$

The $(n-1)$ term in equation (2.9) relates to how many particles can be placed in a configuration with state vector $\boldsymbol{s}_2$ after the first particle with state vector $\boldsymbol{s}_1$ is fixed, see also equation (1.13).

We do not have a closed equation for u_{k_1}, but the first in a series of equations (the BBGKY hierarchy) for the 1-particle, 2-particle, 3-particle, etc. LSDDs. In this case, we make the common mean-field closure assumption that

$$u^{(2)}_{k_1,k_2}(t, \boldsymbol{s}_1, \boldsymbol{s}_2) \approx u_{k_1}(t, \boldsymbol{s}_1) u_{k_2}(t, \boldsymbol{s}_2) \,. \tag{2.10}$$

Notice that in equation (2.10) the LSDD is normalised to the size of the system, not to unity (suggesting probability mass) as in equation (1.15). Therefore, one is additionally making the assumption that $n^2 \approx n(n-1)$.

We now apply the same integration and summation to the right-hand side (RHS) of equation (2.5). This gives

$$\begin{aligned} &\sum_{n=0}^{\infty} n \sum_{\vec{k}_n \in K_{2,n}} \int_{\mathbb{S}^{n-1}} \sum_{i=1}^{n} \sum_{j=i+1}^{n} \mathcal{C}(\boldsymbol{s}_i, k_i - 1, \boldsymbol{s}_j, k_j - 1) \mathscr{P}_n^{\vec{k}^{ij}_{n,-}}(t, \vec{s}_n) \, \mathrm{d}\vec{s}_n^{(2)} \\ &\qquad - \sum_{n=0}^{\infty} n \sum_{\vec{k}_n \in K_{2,n}} \int_{\mathbb{S}^{n-1}} \sum_{i=1}^{n} \sum_{j=i+1}^{n} \mathcal{C}(\boldsymbol{s}_i, k_i, \boldsymbol{s}_j, k_j) \mathscr{P}_n^{\vec{k}_n}(t, \vec{s}_n) \, \mathrm{d}\vec{s}_n^{(2)} \,. \end{aligned} \tag{2.11}$$

For $i > 1$, each individual term appears once in the positive sum and once in the negative sum; they thus cancel each other out. The remaining terms are

$$\sum_{n=0}^{\infty} n \sum_{\vec{k}_n \in K_{2,n}} \int_{\mathbb{S}^{n-1}} \sum_{j=2}^{n} \mathcal{C}(\boldsymbol{s}_1, k_1 - 1, \boldsymbol{s}_j, k_j - 1) \mathscr{P}_n^{\vec{k}^{ij}_{n,-}}(t, \vec{s}_n) \, \mathrm{d}\vec{s}_n^{(2)} \\ - \sum_{n=0}^{\infty} n \sum_{\vec{k}_n \in K_{2,n}} \int_{\mathbb{S}^{n-1}} \sum_{j=2}^{n} \mathcal{C}(\boldsymbol{s}_1, k_1, \boldsymbol{s}_j, k_j) \mathscr{P}_n^{\vec{k}_n}(t, \vec{s}_n) \, \mathrm{d}\vec{s}_n^{(2)} \,. \tag{2.12}$$

Because $\mathscr{P}_n^{\vec{k}_n}(t, \vec{s}_n)$ is invariant with respect to particle relabelling, we can relabel $(\boldsymbol{s}_j, k_j) \leftrightarrow (\boldsymbol{s}_2, k_2)$ in each term in the sum over j to obtain

$$\begin{aligned}
&\sum_{n=0}^{\infty} n \sum_{\vec{k}_n \in K_{2,n}} \int_{\mathbb{S}^{n-1}} \sum_{j=2}^{n} \mathcal{C}(\boldsymbol{s}_1, k_1, \boldsymbol{s}_j, k_j) \mathscr{P}_n^{\vec{k}_n}(t, \vec{s}_n) \, \mathrm{d}\vec{s}_n^{(2)} \\
&= \sum_{n=0}^{\infty} n \sum_{\vec{k}_n \in K_{2,n}} \int_{\mathbb{S}^{n-1}} \sum_{j=2}^{n} \mathcal{C}(\boldsymbol{s}_1, k_1, \boldsymbol{s}_2, k_2) \mathscr{P}_n^{\vec{k}_n}(t, \vec{s}_n) \, \mathrm{d}\vec{s}_n^{(2)} \\
&= \sum_{n=0}^{\infty} n(n-1) \sum_{k_2=0}^{\infty} \int_{\mathbb{S}} \mathcal{C}(\boldsymbol{s}_1, k_1, \boldsymbol{s}_2, k_2) \sum_{\vec{k}_n \in K_{3,n}} \int_{\mathbb{S}^{n-2}} \mathscr{P}_n^{\vec{k}_n}(t, \vec{s}_n) \, \mathrm{d}\vec{s}_n^{(3)} \, \mathrm{d}\boldsymbol{s}_2 \\
&= \sum_{k_2=0}^{\infty} \int_{\mathbb{S}} \mathcal{C}(\boldsymbol{s}_1, k_1, \boldsymbol{s}_2, k_2) u^{(2)}_{k_1,k_2}(t, \boldsymbol{s}_1, \boldsymbol{s}_2) \, \mathrm{d}\boldsymbol{s}_2 \,,
\end{aligned}$$

where the last line follows from equation (2.9). Consequently, we can write (2.11) as

$$\int_{\mathbb{S}} \sum_{k_2=0}^{\infty} \mathcal{C}(\boldsymbol{s}_1, k_1 - 1, \boldsymbol{s}_2, k_2 - 1) u^{(2)}_{k_1-1,k_2-1}(t, \boldsymbol{s}_1, \boldsymbol{s}_2) \, \mathrm{d}\boldsymbol{s}_2 \\ - \int_{\mathbb{S}} \sum_{k_2=0}^{\infty} \mathcal{C}(\boldsymbol{s}_1, k_1, \boldsymbol{s}_2, k_2) u^{(2)}_{k_1,k_2}(t, \boldsymbol{s}_1, \boldsymbol{s}_2) \, \mathrm{d}\boldsymbol{s}_2 \,. \tag{2.13}$$

For the remaining terms on the RHS of equation (2.5), we sum over the degrees and integrate over the states of particles 2 through n, multiply by n, and sum over n to obtain

$$\sum_{n=1}^{\infty} n \sum_{\vec{k}_n \in K_{2,n}} \int_{\mathbb{S}^{n-1}} \left(\sum_{i=1}^{n} \frac{1}{n} \delta_{k_i,0} \, \mathcal{J} \, \mathcal{K}(\boldsymbol{s}_i) \mathscr{P}_{n-1}^{\vec{k}^{i-}_n}(t, \vec{s}^{\,i-}_n) - \mathcal{J} \mathscr{P}_n^{\vec{k}_n}(t, \vec{s}_n) \right) \mathrm{d}\vec{s}_n^{(2)} \,. \tag{2.14}$$

For the term $i = 1$, we are summing and integrating over all arguments of $\mathscr{P}_{n-1}^{\vec{k}^{i-}_n}(t, \vec{s}^{\,i-}_n)$,

so

$$\begin{aligned}
&\sum_{n=1}^{\infty} n \sum_{\vec{k}_n \in K_{2,n}} \int_{\mathbb{S}^{n-1}} \frac{1}{n} \delta_{k_1,0}\, \mathcal{J}\, \mathcal{K}(\boldsymbol{s}_1) \mathscr{P}_{n-1}^{\vec{k}_n^{1-}}(t, \vec{s}_n^{1-})\, \mathrm{d}\vec{s}_n^{(2)} \\
&= \delta_{k_1,0}\, \mathcal{J}\, \mathcal{K}(\boldsymbol{s}_1) \sum_{n=1}^{\infty} \sum_{\vec{k}_n \in K_{2,n}} \int_{\mathbb{S}^{n-1}} \mathscr{P}_{n-1}^{\vec{k}_n^{1-}}(t, \vec{s}_n^{1-})\, \mathrm{d}\vec{s}_n^{(2)} \\
&= \delta_{k_1,0}\, \mathcal{J}\, \mathcal{K}(\boldsymbol{s}_1) \sum_{n=1}^{\infty} \sum_{\vec{k}_{n-1} \in K_{1,n-1}} \int_{\mathbb{S}^{n-1}} \mathscr{P}_{n-1}^{\vec{k}_{n-1}}(t, \vec{s}_{n-1})\, \mathrm{d}\vec{s}_{n-1} \\
&= \delta_{k_1,0}\, \mathcal{J}\, \mathcal{K}(\boldsymbol{s}_1)\,,
\end{aligned}$$

where the last line follows from equation (2.3). For each term $i > 1$, we use the invariance of $\mathscr{P}_n^{\vec{k}_n}(t, \vec{s}_n)$ with respect to particle relabelling to swap particle i with particle n to give

$$\begin{aligned}
&\sum_{n=1}^{\infty} n \sum_{\vec{k}_n \in K_{2,n}} \int_{\mathbb{S}^{n-1}} \sum_{i=2}^{n} \frac{1}{n} \delta_{k_i,0}\, \mathcal{J}\, \mathcal{K}(\boldsymbol{s}_i) \mathscr{P}_{n-1}^{\vec{k}_n^{i-}}(t, \vec{s}_n^{i-})\, \mathrm{d}\vec{s}_n^{(2)} \\
&= \sum_{n=1}^{\infty} n \sum_{\vec{k}_n \in K_{2,n}} \int_{\mathbb{S}^{n-1}} \sum_{i=2}^{n} \frac{1}{n} \delta_{k_n,0}\, \mathcal{J}\, \mathcal{K}(\boldsymbol{s}_n) \mathscr{P}_{n-1}^{\vec{k}_n^{n-}}(t, \vec{s}_n^{n-})\, \mathrm{d}\vec{s}_n^{(2)} \\
&= \mathcal{J} \sum_{n=1}^{\infty} (n-1) \int_{\mathbb{S}} \mathcal{K}(\boldsymbol{s}_n)\, \mathrm{d}\boldsymbol{s}_n \sum_{\vec{k}_{n-1} \in K_{1,n-1}} \int_{\mathbb{S}^{n-2}} \mathscr{P}_{n-1}^{\vec{k}_{n-1}}(t, \vec{s}_{n-1})\, \mathrm{d}\vec{s}_{n-1}^{(2)} \\
&= \mathcal{J} \sum_{n=0}^{\infty} n \sum_{\vec{k}_n \in K_{1,n}} \int_{\mathbb{S}^{n-1}} \mathscr{P}_n^{\vec{k}_n}(t, \vec{s}_n)\, \mathrm{d}\vec{s}_n^{(2)}\,,
\end{aligned}$$

which cancels with the remaining term in equation (2.14).

Therefore, by relabelling particles and using the fact that $\mathscr{P}_n^{\vec{k}_n}(t, \vec{s}_n)$ is invariant with respect to index permutation, we find that

$$\begin{aligned}
\mathrm{RHS} = &\int_{\mathbb{S}} \sum_{k_2=0}^{\infty} \mathcal{C}(\boldsymbol{s}_1, k_1 - 1, \boldsymbol{s}_2, k_2 - 1) u^{(2)}_{k_1-1,k_2-1}(t, \boldsymbol{s}_1, \boldsymbol{s}_2) \mathrm{d}\boldsymbol{s}_2 \\
&- \int_{\mathbb{S}} \sum_{k_2=0}^{\infty} \mathcal{C}(\boldsymbol{s}_1, k_1, \boldsymbol{s}_2, k_2) u^{(2)}_{k_1,k_2}(t, \boldsymbol{s}_1, \boldsymbol{s}_2) \mathrm{d}\boldsymbol{s}_2 \\
&+ \mathcal{J}\mathcal{K}(\boldsymbol{s}_1) \delta_{k_1,0}\,. \qquad (2.15)
\end{aligned}$$

We again need to use the mean-field closure assumption (2.10) to write the 2-particle LSDD in terms of the 1-particle LSDD. This gives the final closed mean-field equation

for the 1-particle LSDD in the absence of edge deletion:

$$\left[\frac{\partial}{\partial t} + \mathcal{L}^{(1)}\right] u_{k_1}(t, \boldsymbol{s}_1) = \left(\int_{\mathbb{S}} \sum_{k_2=0}^{\infty} \mathcal{C}(\boldsymbol{s}_1, k_1 - 1, \boldsymbol{s}_2, k_2 - 1) u_{k_2-1}(t, \boldsymbol{s}_2)\, \mathrm{d}\boldsymbol{s}_2\right) u_{k_1-1}(t, \boldsymbol{s}_1)$$
$$- \left(\int_{\mathbb{S}} \sum_{k_2=0}^{\infty} \mathcal{C}(\boldsymbol{s}_1, k_1, \boldsymbol{s}_2, k_2) u_{k_2}(t, \boldsymbol{s}_2)\, \mathrm{d}\boldsymbol{s}_2\right) u_{k_1}(t, \boldsymbol{s}_1) + \mathcal{J}\mathcal{K}(\boldsymbol{s}_1)\delta_{k_1,0}\,, \tag{2.16}$$

where $u_{k_1} \equiv 0$ if $k_1 < 0$ by convention. When $\mathcal{C}$ is a constant and $\mathbb{S}$ is a point, equation (2.16) reduces to master equations previously found [84]. The quadratic terms in equation (2.16) are analogous to the mean-field term in the Vlaslov equation, where a test particle feels the effect of a "cloud" of points [29, 45, 59].

2.5 Model Derivation: Edge Deletion

The state space $\{(\vec{s}_n, \vec{k}_n) : n > 0\}$ that we used in Section 2.4 is not sufficient when we allow edge deletion. With edge deletion, it is crucial to know whether an edge exists between each pair of nodes, so we must consider the underlying adjacency matrix. For undirected networks with multiedges, the adjacency matrix $A_n = A_n^T$ has entries $(A_n)_{i,j}$ for $i \neq j$ and $i, j \in \{1, \ldots, n\}$, where $(A_n)_{i,j} \in \mathbb{N}_0$ gives the number of edges between nodes i and j.

Because we consider probability distributions over A_n, the most efficient representation is to restrict attention to the independent entries of A_n. We thus change convention slightly and set $(A_n)_{i,j} = 0$ for $i \geq j$, and we will retain the term "adjacency matrix" to indicate the resulting matrix.

2.5.1 Fokker–Planck Equation

Let $\mathcal{P}_n^{A_n}(t, \vec{s}_n)$ denote the probability that a network has adjacency matrix A_n and n nodes with state vectors $\vec{s}_n = \{\boldsymbol{s}_1, \ldots, \boldsymbol{s}_n\}$. The normalisation condition is

$$\sum_{n=1}^{\infty} \left\{ \sum_{A_n \in S_n} \left[\int_{\mathbb{S}^n} \mathcal{P}_n^{A_n}(t, \vec{s}_n)\, \mathrm{d}\vec{s}_n \right] \right\} = 1\,, \tag{2.17}$$

where

$$S_n = \left\{ A_n : \begin{array}{ll} (A_n)_{ij} \in \mathbb{N}_0\,, & 1 \leq i < j \leq n \\ (A_n)_{ij} = 0\,, & \text{otherwise} \end{array} \right\}, \tag{2.18}$$

so that

$$\sum_{A_n \in S_n} \equiv \sum_{(A_n)_{12}=0}^{\infty} \cdots \sum_{(A_n)_{1n}=0}^{\infty} \sum_{(A_n)_{23}=0}^{\infty} \cdots \sum_{(A_n)_{n-1,n}=0}^{\infty}\,.$$

For fixed n, one can calculate the degree k_i of node i from the adjacency matrix using

$$k_i = \sum_{j=i+1}^{n} (A_n)_{ij} + \sum_{j=1}^{i-1} (A_n)_{ji}\,.$$

Therefore, we can relate the distributions $\mathscr{P}$ and $\mathcal{P}$ via

$$\mathscr{P}_n^{\vec{k}_n}(t,\vec{s}_n) = \sum_{A_n\in S_n}\left[\prod_{i=1}^{n}\delta\left(k_i,\sum_{j=i+1}^{n}(A_n)_{ij}+\sum_{j=1}^{i-1}(A_n)_{ji}\right)\right]\mathcal{P}_n^{A_n}(t,\vec{s}_n)\,, \tag{2.19}$$

where $\delta(a,b)$ is the Kronecker delta (which is usually written as δ_{ab}). When we include edge deletion, the hierarchical Fokker–Planck equation (2.5) becomes

$$\begin{aligned}
&\left(\frac{\partial}{\partial t}+\mathcal{L}^{(n)}\right)\mathcal{P}_n^{A_n}(t,\vec{s}_n)\\
&=\sum_{1\le i<j\le n}\left(\mathcal{C}(\boldsymbol{s}_i,k_i-1,\boldsymbol{s}_j,k_j-1)\mathcal{P}_n^{A_{n,-}^{ij}}(t,\vec{s}_n)-\mathcal{C}(\boldsymbol{s}_i,k_i,\boldsymbol{s}_j,k_j)\mathcal{P}_n^{A_n}(t,\vec{s}_n)\right)\\
&+\sum_{1\le i<j\le n}\left((A_{n,+}^{ij})_{ij}\mathcal{D}(\boldsymbol{s}_i,k_i+1,\boldsymbol{s}_j,k_j+1)\mathcal{P}_n^{A_{n,+}^{ij}}(t,\vec{s}_n)-(A_n)_{ij}\mathcal{D}(\boldsymbol{s}_i,k_i,\boldsymbol{s}_j,k_j)\mathcal{P}_n^{A_n}(t,\vec{s}_n)\right)\\
&+\frac{1}{n}\sum_{i=1}^{n}\left[\prod_{j=1}^{i-1}\delta(0,(A_n)_{ji})\right]\left[\prod_{j=i+1}^{n}\delta(0,(A_n)_{ij})\right]\mathcal{J}\mathcal{K}(\boldsymbol{s}_i)\mathcal{P}_{n-1}^{A_n^{i-}}(t,\vec{s}_n^{\,i-})-\mathcal{J}\mathcal{P}_n^{A_n}(t,\vec{s}_n)\,,
\end{aligned} \tag{2.20}$$

where

$$(A_{n,\pm}^{ij})_{lm} = \begin{cases} (A_n)_{lm}\pm 1\,, & \text{if } (i,j)=(l,m)\,,\\ (A_n)_{lm}\,, & \text{otherwise}\,. \end{cases} \tag{2.21}$$

The first term on the RHS of equation (2.20) corresponds to edge-creation events between nodes i and j as before (see Section 2.4). The first part of the second term corresponds to gaining a network with adjacency matrix A_n from a network with adjacency matrix $A_{n,+}^{ij}$ by deleting an edge between i and j. Note that $\mathcal{D}$ is the rate of deletion per edge, so we multiply by the number of edges (which is equal to $(A_n)_{ij}+1$) between i and j. The second part of this term corresponds to losing a network with adjacency matrix A_n by deleting an edge between i and j (to produce a network with adjacency matrix $A_{n,-}^{ij}$).

The third term on the RHS of equation (2.20) corresponds to gaining a network with adjacency matrix

$$\begin{pmatrix}
0 & A_{12} & \dots & A_{1,i-1} & 0 & A_{1,i+1} & A_{1,i+2} & \dots & A_{1n}\\
0 & 0 & \dots & A_{2,i-1} & 0 & A_{2,i+1} & A_{2,i+2} & \dots & A_{2n}\\
\vdots & & & & \vdots & & & & \vdots\\
0 & 0 & 0 & \dots & 0 & A_{i-1,i+1} & A_{i-1,i+2} & \dots & A_{i-1,n}\\
0 & 0 & 0 & \dots & 0 & 0 & 0 & \dots & 0\\
0 & 0 & 0 & \dots & 0 & 0 & A_{i+1,i+2} & \dots & A_{i+1,n}\\
0 & 0 & 0 & \dots & 0 & 0 & \dots & 0 & A_{n-1,n}\\
0 & 0 & 0 & \dots & 0 & 0 & \dots & 0 & 0
\end{pmatrix},$$

from an adjacency matrix

$$A_n^{i-} = \begin{pmatrix} 0 & A_{12} & \dots & A_{1,i-1} & A_{1,i+1} & A_{1,i+2} & \dots & A_{1n} \\ 0 & 0 & \dots & A_{2,i-1} & A_{2,i+1} & A_{2,i+2} & \dots & A_{2n} \\ \vdots & & & & & & & \vdots \\ 0 & 0 & 0 & \dots & A_{i-1,i+1} & A_{i-1,i+2} & \dots & A_{i-1,n} \\ 0 & 0 & 0 & \dots & 0 & A_{i+1,i+2} & \dots & A_{i+1,n} \\ 0 & 0 & 0 & \dots & 0 & \dots & 0 & A_{n-1,n} \\ 0 & 0 & 0 & \dots & 0 & \dots & 0 & 0 \end{pmatrix},$$

by relabelling nodes $j \to j+1$ for $j \geq i$ and adding a new unconnected node with label i (which we choose uniformly at random from the set $\{1, \dots, n\}$). The Kronecker δ ensures that this term is present only when $(A_n)_{ij} = (A_n)_{ji} = 0$. As in Section 2.4, the uniformly random choice of the label for the new node ensures that $\mathcal{P}_n^{A_n}(t, \vec{s}_n)$ is invariant with respect to index permutations.

2.5.2 Low-Dimensional Approximation

In kinetic theory, the first question to address when deriving a reduced model is which variables to retain in the model and over which to integrate. In Section 2.4, each variable was associated with a node in a network, and it was natural to integrate over all nodes but the first. We thus retained the state and degree of node 1 as independent variables. We could have reduced the model further by subsequently integrating over either the state or degree of node 1.

When considering edge deletion, it is much more difficult to associate the independent variables with individual nodes, since each entry of an adjacency matrix is associated with a pair of nodes. Consequently, it is not obvious which variables are natural to retain in a reduced model and which variables should be integrated out. To facilitate a direct comparison of the reduced model including edge deletion with the reduced model of Section 2.4, we again retain the state and degree of node 1 as independent variables. We thus sum over all entries of the adjacency matrix for which node 1 has degree k_1. Additionally, as before, we integrate over $\vec{s}_n^{(2)}$, multiply by n, and sum over n.

Because the operators $\mathcal{L}^{(n)}$ that we are considering do not depend on network structure, the approximation of the LHS of equation (2.20) proceeds as in Section 2.4.2. This modelling assumption is done for simplicity only; the approach would be equally valid if $\mathcal{L}^{(n)}$ depended on network structure — this possibility is discussed in the conclusion chapter (Chapter 5).

For the edge-creation term on the RHS of equation (2.20) we find, as in Section 2.4.1, that for $i > 1$, each term appears once in the positive sum and once in the negative sum; these terms thus cancel. For the remaining terms (for which $i = 1$), we exploit the invariance of $\mathcal{P}_n^{A_n}(t, \vec{s}_n)$ with respect to particle relabelling. Specifically, we relabel $j \leftrightarrow 2$ in each term in the sum over j (i.e., swapping rows and columns of

A_n) to obtain

$$\sum_{n=0}^{\infty} n \sum_{A_n \in S_n} \int_{\mathbb{S}^{n-1}} \delta\left(k_1, \sum_{j=2}^{n} (A_n)_{1j}\right) (n-1)\mathcal{C}(\boldsymbol{s}_1, k_1 - 1, \boldsymbol{s}_2, k_2 - 1)\mathcal{P}_n^{A^{12}_{n,-}}(t, \vec{s}_n)\, \mathrm{d}\vec{s}_n^{(2)}$$
$$- \sum_{n=0}^{\infty} n \sum_{A_n \in S_n} \int_{\mathbb{S}^{n-1}} \delta\left(k_1, \sum_{j=2}^{n} (A_n)_{1j}\right) (n-1)\mathcal{C}(\boldsymbol{s}_1, k_1, \boldsymbol{s}_2, k_2)\mathcal{P}_n^{A_n}(t, \vec{s}_n)\, \mathrm{d}\vec{s}_n^{(2)}\,, \tag{2.22}$$

where the Kronecker δ enforces the degree condition. The 2-particle LSDD is

$$\begin{aligned} &u^{(2)}_{k_1,k_2}(t, \boldsymbol{s}_1, \boldsymbol{s}_2) \\ &= \sum_{n=0}^{\infty} n(n-1) \sum_{A_n \in S_n} \delta\left(k_1, \sum_{j=2}^{n} (A_n)_{1j}\right) \delta\left(k_2, (A_n)_{12} + \sum_{j=3}^{n} (A_n)_{2j}\right) \\ &\quad \times \int_{\mathbb{S}^{n-2}} \mathcal{P}_n^{A_n}(t, \vec{s}_n)\, \mathrm{d}\vec{s}_n^{(3)}\,, \end{aligned} \tag{2.23}$$

so one can write equation (2.22) as equation (2.13), and the analysis proceeds as in Section 2.4.2.

Let us now consider the edge-deletion terms. As with the edge-creation terms, for $i > 1$, each term appears once in the positive sum and once in the negative sum; these terms thus cancel each other. For the remaining terms (for which $i = 1$), relabelling $j \leftrightarrow 2$ in each term in the sum over j yields

$$\begin{aligned} &\sum_{n=0}^{\infty} n(n-1) \sum_{A_n \in S_n} \delta\left(k_1, \sum_{j=2}^{n} (A_n)_{1j}\right) \\ &\quad \times \int_{\mathbb{S}^{n-1}} (A^{12}_{n,+})_{12}\mathcal{D}(\boldsymbol{s}_1, k_1 + 1, \boldsymbol{s}_2, k_2 + 1)\mathcal{P}_n^{A^{12}_{n,+}}(t, \vec{s}_n)\, \mathrm{d}\vec{s}_n^{(2)} \\ &- \sum_{n=0}^{\infty} n(n-1) \sum_{A_n \in S_n} \delta\left(k_1, \sum_{j=2}^{n} (A_n)_{1j}\right) \\ &\quad \times \int_{\mathbb{S}^{n-1}} (A_n)_{12}\mathcal{D}(\boldsymbol{s}_1, k_1, \boldsymbol{s}_2, k_2)\mathcal{P}_n^{A_n}(t, \vec{s}_n)\, \mathrm{d}\vec{s}_n^{(2)} \\ &= \sum_{k_2=0}^{\infty} \int_{\mathbb{S}} \mathcal{D}(\boldsymbol{s}_1, k_1 + 1, \boldsymbol{s}_2, k_2 + 1) U^{(2)}_{k_1+1,k_2+1}(t, \boldsymbol{s}_1, \boldsymbol{s}_2)\, \mathrm{d}\boldsymbol{s}_2 \\ &- \sum_{k_2=0}^{\infty} \int_{\mathbb{S}} \mathcal{D}(\boldsymbol{s}_1, k_1, \boldsymbol{s}_2, k_2) U^{(2)}_{k_1,k_2}(t, \boldsymbol{s}_1, \boldsymbol{s}_2)\, \mathrm{d}\boldsymbol{s}_2\,, \end{aligned} \tag{2.24}$$

where

$$
\begin{aligned}
&U^{(2)}_{k_1,k_2}(t,\boldsymbol{s}_1,\boldsymbol{s}_2)\\
&=\sum_{n=0}^{\infty} n(n-1)\sum_{A_n\in S_n}\delta\left(k_1,\sum_{j=2}^{n}(A_n)_{1j}\right)\delta\left(k_2,(A_n)_{12}+\sum_{j=3}^{n}(A_n)_{2j}\right)\\
&\quad\times\int_{\mathbb{S}^{n-2}}(A_n)_{12}\mathcal{P}_n^{A_n}(t,\vec{s}_n)\,\mathrm{d}\vec{s}_n^{(3)}\,,
\end{aligned}
\tag{2.25}
$$

note that the $(A_n)_{12}$ factor in equation (2.25) determines the difference between $u^{(2)}_{k_1,k_2}$ and $U^{(2)}_{k_1,k_2}$.

There is now a new closure problem, as we need to relate $U^{(2)}_{k_1,k_2}(t,\boldsymbol{s}_1,\boldsymbol{s}_2)$ to known variables. One choice is to relate $U^{(2)}_{k_1,k_2}$ to $u^{(2)}_{k_1,k_2}$ via

$$
U^{(2)}_{k_1,k_2}(t,\boldsymbol{s}_1,\boldsymbol{s}_2)=\alpha u^{(2)}_{k_1,k_2}(t,\boldsymbol{s}_1,\boldsymbol{s}_2)\,,
$$

where α is the expected number of edges between nodes 1 and 2, given then these nodes have degrees k_1 and k_2, respectively.

If there are m edges in total, there are $2m$ stubs (ends of edges, or "half edges"), of which k_1 are at node 1 and k_2 at node 2. In the configuration model, one specifies a desired degree sequence $\vec{k}_n=\{k_1,\ldots,k_n\}$, assigns the appropriate number of stubs to the nodes in question, and then connects edges between pairs of stubs chosen uniformly at random. The resulting graphs can then have self-loops and multiedges. Nonetheless, we use this to approximate the probability that a given edge connects nodes 1 and 2 as

$$
2\times\frac{k_1}{2m}\times\frac{k_2}{2m}\,.
$$

Therefore a reasonable closure assumption for the expected number of edges between nodes 1 and 2 is

$$
\alpha\approx\frac{k_1k_2}{2m}=\frac{k_1k_2}{E[N]\langle k\rangle}=\frac{k_1k_2}{\int_{\mathbb{S}}\sum_{k_1=0}^{\infty}k_1u_{k_1}(t,\boldsymbol{s}_1)\,\mathrm{d}\boldsymbol{s}_1}\,,
$$

where $E[N]$ is the expected number of nodes and $\langle k\rangle$ is the mean degree. This assumption is valid for large networks where node degrees and states are uncorrelated. Whilst this assumption is obviously incorrect, it allows us to close the system of equations.

Using a mean-field approximation for $u^{(2)}_{k_1,k_2}(t,\boldsymbol{s}_1,\boldsymbol{s}_2)$, we can then close the edge deletion term by writing

$$
U^{(2)}_{k_1,k_2}(t,\boldsymbol{s}_1,\boldsymbol{s}_2)=\frac{k_1k_2u_{k_1}(t,\boldsymbol{s}_1)u_{k_2}(t,\boldsymbol{s}_2)}{\int_{\mathbb{S}}\sum_{k_1=0}^{\infty}k_1u_{k_1}(t,\boldsymbol{s}_1)\,\mathrm{d}\boldsymbol{s}_1}\,.
$$

Finally, we consider the node-creation term. The term $i = 1$ gives

$$\begin{aligned}
&\sum_{n=0}^{\infty} n \sum_{A_n \in S_n} \int_{\mathbb{S}^{n-1}} \delta\left(k_1, \sum_{j=2}^{n} (A_n)_{1j}\right) \frac{1}{n} \left[\prod_{j=2}^{n} \delta(0, (A_n)_{1j})\right] \mathcal{J}\mathcal{K}(\boldsymbol{s}_1) \mathcal{P}_{n-1}^{A_n^{1-}}(t, \vec{s}_n^{\,1-}) \, \mathrm{d}\vec{s}_n^{\,(2)} \\
&= \delta_{k_1,0} \, \mathcal{J} \, \mathcal{K}(\boldsymbol{s}_1) \sum_{n=1}^{\infty} \sum_{A_n^{1-} \in S_{n-1}} \int_{\mathbb{S}^{n-1}} \mathcal{P}_{n-1}^{A_n^{1-}}(t, \vec{s}_{n-1}) \, \mathrm{d}\vec{s}_{n-1} \\
&= \delta_{k_1,0} \, \mathcal{J} \, \mathcal{K}(\boldsymbol{s}_1) \,,
\end{aligned}$$

where the last equality follows by equation (2.17). For each term with $i > 1$, we can use the invariance of $\mathscr{P}_n^{\vec{k}_n}(t, \vec{s}_n)$ with respect to particle relabelling to swap particle i with particle n. As in our prior calculations, we then find that all of these terms cancel each other out.

Our low-dimensional approximation to (2.20) is thus

$$\begin{aligned}
&\left[\frac{\partial}{\partial t} + \mathcal{L}^{(1)}\right] u_{k_1}(t, \boldsymbol{s}_1) \\
&= u_{k_1-1}(t, \boldsymbol{s}_1) \left(\int_{\mathbb{S}} \sum_{k_2=0}^{\infty} \mathcal{C}(\boldsymbol{s}_1, k_1 - 1, \boldsymbol{s}_2, k_2 - 1) u_{k_2-1}(t, \boldsymbol{s}_2) \, \mathrm{d}\boldsymbol{s}_2\right) \\
&\quad - u_{k_1}(t, \boldsymbol{s}_1) \left(\int_{\mathbb{S}} \sum_{k_2=0}^{\infty} \mathcal{C}(\boldsymbol{s}_1, k_1, \boldsymbol{s}_2, k_2) u_{k_2}(t, \boldsymbol{s}_2) \, \mathrm{d}\boldsymbol{s}_2\right) \\
&+ \frac{(k_1 + 1) u_{k_1+1}(t, \boldsymbol{s}_1)}{\int_{\mathbb{S}} \sum_{k_1=0}^{\infty} k_1 u_{k_1}(t, \boldsymbol{s}_1) \, \mathrm{d}\boldsymbol{s}_1} \left(\int_{\mathbb{S}} \sum_{k_2=0}^{\infty} \mathcal{D}(\boldsymbol{s}_1, k_1 + 1, \boldsymbol{s}_2, k_2 + 1)(k_2 + 1) u_{k_2+1}(t, \boldsymbol{s}_2) \, \mathrm{d}\boldsymbol{s}_2\right) \\
&\quad - \frac{k_1 u_{k_1}(t, \boldsymbol{s}_1)}{\int_{\mathbb{S}} \sum_{k_1=0}^{\infty} k_1 u_{k_1}(t, \boldsymbol{s}_1) \, \mathrm{d}\boldsymbol{s}_1} \left(\int_{\mathbb{S}} \sum_{k_2=0}^{\infty} \mathcal{D}(\boldsymbol{s}_1, k_1, \boldsymbol{s}_2, k_2) k_2 u_{k_2}(t, \boldsymbol{s}_2) \, \mathrm{d}\boldsymbol{s}_2\right) \\
&+ \mathcal{J}\mathcal{K}(\boldsymbol{s}_1) \delta_{k_1,0} \,. \qquad (2.26)
\end{aligned}$$

2.6 Numerical Examples

We now carry out Monte Carlo simulations of our stochastic network evolution process to illustrate the validity of equations (2.16) and (2.26) for sufficiently large networks.

First, in Section 2.6.1, we investigate numerically the validity of the mean-field assumption for our model when the state space is a point. Second, in Section 2.6.2, we use an example scenario to demonstrate that a numerical solution of equations (2.16) and (2.26) matches well with a full Monte Carlo simulation of the underlying process. Third, in Section 2.6.3, we adapt the example scenario to consider the convergence of a network's degree distribution in the limit of large networks. Fourth, Section 2.6.4, we show that one can use our kinetic approximation as an alternative to some one-step network creation models proposed by Boguñá *et al.* [17]. Finally, in Section 2.6.5, we briefly consider some further approximations that one can make to equations (2.16) and (2.26).

2.6.1 Accuracy of Our Mean-Field Assumption

In the absence of a network structure, the validity of the mean-field approximation depends on the choice of $\mathcal{L}^{(n)}$, and it has been studied widely [19, 29, 37, 45, 59]. In this chapter, we focus on evolving network structure. In our exploration of the validity of the mean-field approximation in the network evolution model, we suppose that there is no state dependence in either the node creation rate $\mathcal{C}$ or the node deletion rate $\mathcal{D}$.

The 2-particle degree distribution $P^{(2)}_{k_1,k_2}$ is the probability that two nodes selected uniformly at random without replacement have degrees k_1 and k_2. In our mean-field closure, we approximate this quantity by the product $P_{k_1}P_{k_2}$, where P_{k_1} is the probability that a single node selected uniformly at random has degree k_1 (and P_{k_2} is defined analogously). In Figure 2.2, we compare the empirical distributions $P^{(2)}_{k_1,k_2}(t)$ and $P_{k_1}(t)P_{k_2}(t)$ generated from 100 realisations of Algorithm 1 using 125 particles (and no node creation). The specific choices of $\mathcal{C}$ and $\mathcal{D}$ shown in the figure are $\mathcal{C}(k_i,k_j) = 2$ and $\mathcal{D}(k_i,k_j) = k_i + k_j$, but many choices were tested including $\mathcal{C},\mathcal{D} \propto 1, k_1, k_2, k_1+k_2$ with similar results.

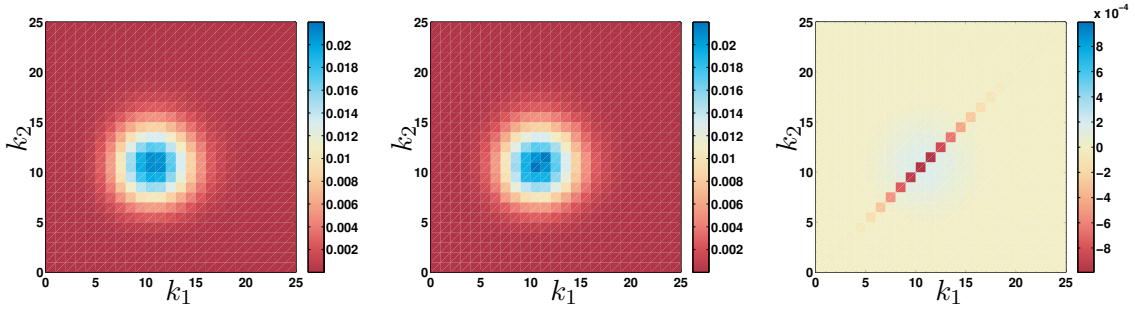

Figure 2.2: Numerical illustration of the validity of the mean-field assumption (2.10). We average over 100 realisations of Algorithm 1 using $n = 125$ particles and a time step of $\Delta t = 10^{-3}$. No new particles enter the system ($\mathcal{J} = 0$), the edge creation rate is $\mathcal{C}(k_i,k_j) = 2$, and the edge deletion rate is $\mathcal{D}(k_i,k_j) = k_i + k_j$. We show (left) the 2-particle distribution $P^{(2)}_{k_1,k_2}(t)$, (middle) the product $P_{k_1}(t)P_{k_2}(t)$ of the 1-particle distributions, and (right) the difference $P^{(2)}_{k_1,k_2}(t) - P_{k_1}(t)P_{k_2}(t)$ at time $t = 1/10$.

We see that our mean-field approximation does well on this example, and the main error occurs when $k_1 = k_2$, for which the product $P_{k_1}(t)P_{k_2}(t)$ of 1-particle distributions is slightly larger than the 2-particle distribution $P^{(2)}_{k_1,k_2}(t)$. This discrepancy arises because one cannot select the same node twice when evaluating the correlation function $P^{(2)}_{k_1,k_2}(t)$, so the probability of finding two nodes with the same degree is lower than that estimated by $P_{k_1}(t)P_{k_2}(t)$ (which corresponds to choosing two nodes uniformly randomly with replacement). The difference should therefore tend to 0 as $1/n$ as the number n of nodes becomes infinite.

One way to evaluate the difference between two probability distributions is the Kolmogorov–Smirnov (KS) test [120], which gives the probability ρ_{KS} that one rejects the hypothesis that the two distributions are equal. For $P^{(2)}_{k_1,k_2}(t)$ and $P_{k_1}(t)P_{k_2}(t)$, we

find that $\rho_{\mathrm{KS}} \approx 2.0 \times 10^{-3}$. This probability is very small, corresponding to a 0.2% chance that the two distributions are not equal.

2.6.2 Example Scenario: Local State Degree Distribution

The example in Section 2.6.1 was particularly simple, as it focused only on the network aspect of the model. We now want to compare Monte Carlo simulations of a much more complicated evolving spatial network with a numerical solution of the reduced equation (2.26). We select our new example to illustrate and evaluate all of the model components described in Table 2.1. It does not represent any particular physical or biological process.

Let us consider noninteracting point particles contained in the unit square, so one can describe the state of each particle by its position vector $\boldsymbol{s}_i = (x_i, y_i) \in [0,1]^2$. We suppose that these positions evolve according to the SDEs [113]

$$\mathrm{d}X_i = \mu \,\mathrm{d}t + \sigma \,\mathrm{d}W_t \,, \quad \mathrm{d}Y_i = \sigma \,\mathrm{d}W_t \,, \tag{2.27}$$

where as before we use capital letters $\boldsymbol{S}_i = (X_i, Y_i)$ to distinguish random variables from the values that they take. We assume that the drift coefficient $\mu > 0$ and volatility coefficient $\sigma > 0$ are constant (corresponding to a constant diffusion coefficient $\sigma^2/2$). To initialise, we place 1000 particles with degree 0 uniformly at random in the rectangle $(X_i, Y_i) \in [0, 1/10] \times [0, 1]$. We impose reflective boundary conditions at $x = 0$ and $x = 1$, and we impose periodic boundary conditions at $y = 0$ and $y = 1$. To generate some spatial heterogeneity, we suppose that the rate of edge creation between nodes depends both on the distance between nodes and on the spatial coordinates of each node. We take

$$\mathcal{C}(\boldsymbol{S}_i, k_i, \boldsymbol{S}_j, k_j) = \left\{ \begin{array}{cc} X_i + X_j \,, & \text{if } ||\boldsymbol{S}_i - \boldsymbol{S}_j|| \leq \epsilon \,, \\ 0 \,, & \text{otherwise} \end{array} \right\}. \tag{2.28}$$

In contrast, we suppose that the rate of edge deletion per edge between nodes i and j depends on the degrees of nodes i and j but is independent of position. Specifically, we take

$$\mathcal{D}(\boldsymbol{S}_i, k_i, \boldsymbol{S}_j, k_j) = \frac{k_i + k_j}{10} \,. \tag{2.29}$$

We introduce new nodes of degree 0 at a rate $\mathcal{J}$ uniformly at random in the rectangle $(x, y) \in [0, 1/10] \times [0, 1]$. Therefore,

$$\mathcal{K}(x, y) = \left\{ \begin{array}{ll} 10 \,, & \text{if } x < 1/10 \,, \\ 0 \,, & \text{otherwise} \,. \end{array} \right. \tag{2.30}$$

We give a schematic illustration of these processes in Figure 2.3. We simulate the system using Algorithm 1 until final time $T_{\mathrm{end}} = 1/2$.

Having defined the stochastic process that we are simulating, we now turn to the reduced model (2.26). Because $\mathcal{C}(\boldsymbol{s}_1, k_1, \boldsymbol{s}_2, k_2)$ and $\mathcal{D}(\boldsymbol{s}_1, k_1, \boldsymbol{s}_2, k_2)$ are independent of y_1 and y_2, and $\mathcal{K}(x, y)$ is independent of y, we expect a solution in which $u_{k_1}(t, \boldsymbol{s}_1)$ is independent of y_1. Integrating over y_1 gives

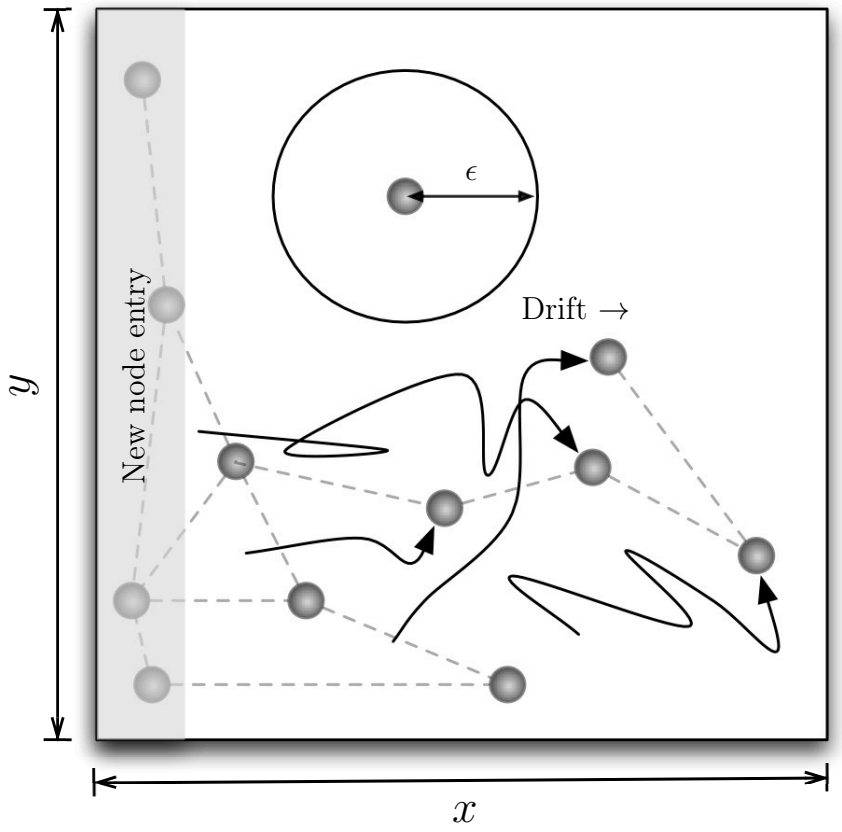

Figure 2.3: Illustration of the example scenario in Section 2.6.2. Nodes enter the system in a strip on the left-hand side of the unit square and then diffuse and drift to the right through equation (2.27). There are reflective boundary conditions at $x = 0$ and $x = 1$ and periodic boundary conditions at $y = 0$ and $y = 1$. We create edges between nearby nodes according to equation (2.28). Edges are deleted at the rate given by equation (2.29).

$$\begin{aligned}
&\frac{\partial u_{k_1}}{\partial t}(t,x_1) + \mu\frac{\partial u_{k_1}}{\partial x_1}(t,x_1) - \frac{\sigma^2}{2}\frac{\partial^2 u_{k_1}}{\partial x_1^2}(t,x_1) \\
&= \left(\sum_{k_2=0}^{\infty}\int_0^1 \hat{\mathcal{C}}(x_1,x_2)u_{k_2}(t,x_2)\,\mathrm{d}x_2\right)\left(u_{k_1-1}(t,x_1) - u_{k_1}(t,x_1)\right) \\
&\quad + \frac{\int_0^1\sum_{k_2=0}^{\infty}k_2^2 u_{k_2}(t,x_2)\,\mathrm{d}x_2}{10\int_0^1\sum_{k_2=1}^{\infty}k_2 u_{k_2}(t,x_2)\,\mathrm{d}x_2}\left((k_1+1)^2 u_{k_1+1}(t,x_1) - k_1^2 u_{k_1}(t,x_1)\right) \\
&\quad + \mathcal{J}\mathcal{K}(x_1)\delta_{k_1,0}\,,
\end{aligned} \tag{2.31}$$

where

$$\hat{\mathcal{C}}(x_1,x_2) = \left\{ \begin{array}{ll} 2(x_1+x_2)\sqrt{\epsilon^2 - |x_1-x_2|^2}\,, & \text{if } |x_1-x_2| \le \epsilon\,, \\ 0\,, & \text{otherwise} \end{array} \right\}. \tag{2.32}$$

We solve (2.31) with no-flux conditions at $x = 0$ and $x = 1$ and initial condition

$$u_{k_1}(t = 0, x_1) = \begin{cases} 10^4 \delta_{k,0}\,, & x_1 \in [0, 1/10]\,, \\ 0 & \text{otherwise}\,, \end{cases} \tag{2.33}$$

because initially there are 10^3 particles placed uniformly at random in $[0, 1/10] \times [0, 1]$.

In Figure 2.4, we show a comparison between a Monte Carlo simulation of $u_k(t, x)$ using Algorithm 1 and a numerical solution of equation (2.31) using a second-order central difference finite-volume method (FVM) in space and a fourth-order Runge–Kutta scheme in time (see Appendix B). We use the parameter values $\mu = 3/4$, $\sigma = 1/4$, $\mathcal{J} = 500$, and $\epsilon = 0.1$.

We observe that the distribution function $u_k(t, x_1)$ is non-trivial, and that the reduced model does a good job of capturing the empirical distribution that we obtain from Monte Carlo simulations. The KS probability for the distributions in Figure 2.4 is $\rho_{\text{KS}} \approx 3.2 \times 10^{-2}$.

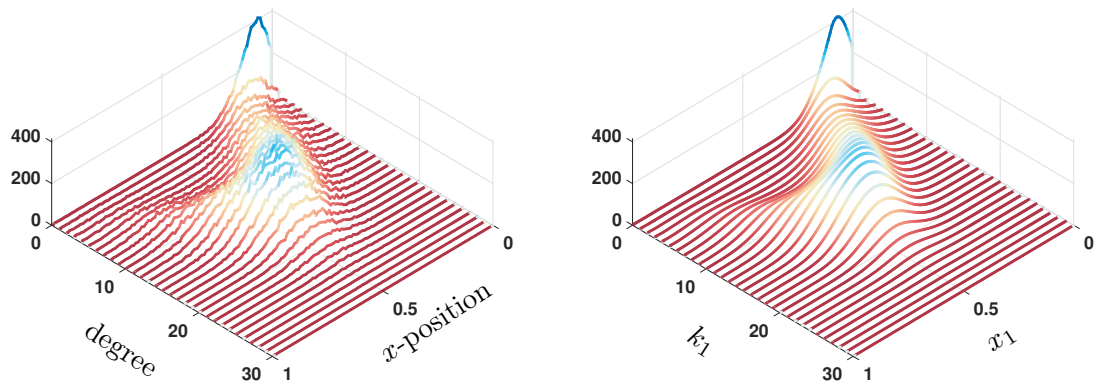

Figure 2.4: Comparison of (left) the mean of 200 Monte Carlo simulations using Algorithm 1 binned into compartments of size 1/100 along the x-axis and (right) $u_{k_1}(1/2, x_1)$ obtained from the numerical solution of equation (2.31). The parameter values are $\mathcal{J} = 500$, $\mu = 3/4$, $\sigma = 1/4$, and $\epsilon = 0.1$; and the time step in the stochastic (i.e., Monte Carlo) simulations is $\Delta t = 10^{-4}$. We initialise the simulations with 10^3 particles placed uniformly randomly in the domain $[0, 1/10] \times [0, 1]$. We show results at the final time $T_{\text{end}} = 1/2$.

2.6.3 Limit of Large Networks

We expect our mean-field assumption to be more accurate for larger networks. We now briefly investigate this hypothesis in the context of degree distributions. (Naturally, it is also relevant to consider this hypothesis for other quantities.)

For a network with n nodes, $u_k = \mathcal{O}(n)$, so we see that all the terms in equation (2.26) have the same order as $n \to \infty$ if $\mathcal{C} = \mathcal{O}(1/n)$ and $\mathcal{D} = \mathcal{O}(1)$. To investigate the convergence for large n, we consider networks in which the number of nodes is constant in time (i.e., $\mathcal{J} \equiv 0$). We first consider networks in which there is no edge

deletion (i.e., $\mathcal{D} \equiv 0$). We take the edge-creation rate to be $500/n$ times that given in equation (2.28). We choose all other parameters as in Section 2.6.2.

In the left panel of Figure 2.5, we show the mean degree distribution sampled over $10^6/n$ realisations of Algorithm 1 for $n = 125$, $n = 500$, $n = 2000$, and $n = 8000$. We also show the degree distribution calculated by solving the IPDE (2.31). Qualitatively, this figure supports the hypothesis that, at least in terms of degree distribution, the mean-field approximation is more accurate for larger networks.

We now introduce edge deletion and choose $\mathcal{D}$ to be given by equation (2.29). We increase the rate of edge creation slightly by taking the edge-creation rate to be $750/n$ times that given in equation (2.28). We show the resulting mean degree distribution sampled over $10^6/n$ realisations of Algorithm 1 for $n = 125$, $n = 500$, $n = 2000$, and $n = 8000$ in the right panel of Figure 2.5 along with the degree distribution that we calculated by solving the IPDE (2.31).

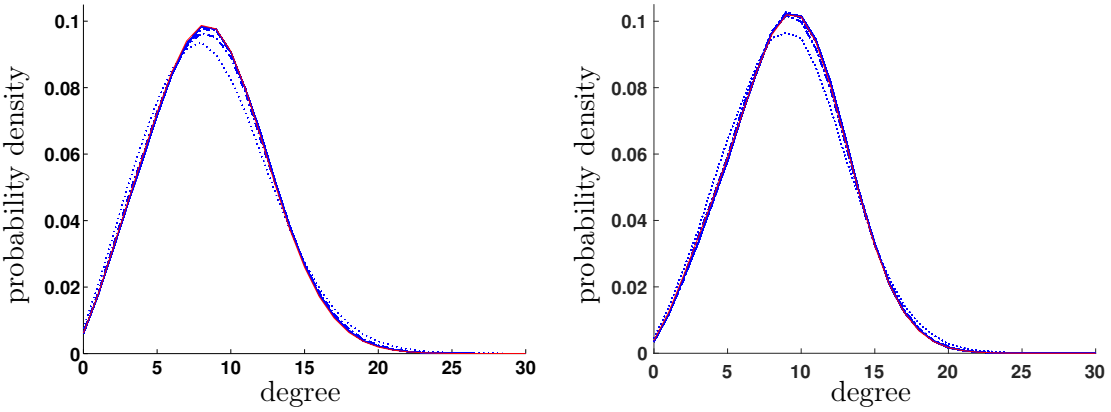

Figure 2.5: Comparison of degree distribution at time $T_{\text{end}} = 1/2$ determined from solution to mean field model [equation (2.31)] (red) and from a mean over multiple Monte Carlo simulations using Algorithm 1 with a time step of $\Delta t = 10^{-3}$ (blue). With n nodes (constant in time; $\mathcal{J} \equiv 0$), we average the simulations are over $10^6/n$ realisations, where $n = 125$ (dotted curve), $n = 500$ (dash-dotted curve), $n = 2000$ (dash-dotted curve), and $n = 8000$ (solid curve). (Left) No edge deletion (i.e., $\mathcal{D} \equiv 0$), and the edge-creation rate is $500/n$ times that given in equation (2.28). (Right) The edge deletion is given by equation (2.29), and the edge creation rate $750/n$ times that given in equation (2.28). The other parameter values are as in Section 2.6.2.

2.6.4 One-Step Network Creation Versus Kinetic Approximations

Dynamic models of network creation can provide an alternative to one-step network creation. For example, in the standard $G(n, p)$ Erdős–Rényi (ER) model [109], one specifies that a network has n nodes and that each pair of nodes is connected with independent, constant probability $p \in (0, 1)$. This leads to a binomial degree distribution $\text{Bin}(n - 1, p)$, which becomes the Poisson distribution $\text{Pois}(np)$ in the limit $n \to \infty$ with fixed np. Reference [84] discussed an alternative, dynamic approach

to the ER model in which an initially unconnected network has n nodes and each node connects to other nodes uniformly at random at a specified rate. In the $n \to \infty$ limit, one can solve a master equation to obtain a Poisson degree distribution, which coincides with the standard model when halted at a specific time (depending on the edge-creation rate). We note also the work by Krioukov and Ostilli [86], who showed that certain equilibrium ensembles create the same distribution of graphs as non-equilibrium ensembles.

References [16, 17] discussed a one-step network-creation model that allows nodes to have an associated state. Nodes i and j have randomly distributed latent social variables $\boldsymbol{s}_i$ and $\boldsymbol{s}_j$, and these nodes are adjacent to each other with probability $r(\boldsymbol{s}_i, \boldsymbol{s}_j)$. References [16, 17] then used a mean-field approximation to derive a formula for the degree distribution (depending on the probability distribution of the social variables and on the function r) of the network as the number of nodes tends to infinity.

One can use our kinetic approach as an alternative to one-step creation to examine such a scenario. To demonstrate this, we consider the case investigated in [17], where the latent social variable is a positive scalar $\boldsymbol{s} = h \in [0, h_{\max}]$ and

$$r(h_i, h_j) = \frac{1}{1 + (b^{-1}|h_i - h_j|)^{\alpha}}\,, \tag{2.34}$$

for constants b and α. We solve equation (2.16) with an initial condition corresponding to n unconnected nodes that are distributed uniformly at random in a state space $[0, h_{\max}]$. No new nodes enter the system (i.e., $\mathcal{J} \equiv 0$), there is no edge deletion (i.e., $\mathcal{D} \equiv 0$), and the edge-creation rate is $\mathcal{C} = r(h_i, h_j)$. Thus, at time $T_{\text{end}} = 1$, the expected number of edges between node i and node j is $r(h_i, h_j)$. In Figure 2.6, we see for parameter values $n = 1000$, $\alpha = 3$, and $b = 1/2$ that the degree distribution given by our mean-field model at $t = T_{\text{end}}$ matches very closely with the analytical formula of [17]. We solved the IPDE using a method of lines with a spatial discretisation of $\Delta h = 1/4$ and a fourth-order Runge–Kutta scheme in time.

2.6.5 Final Remarks: Moment Closure

Despite the fact that equations (2.16) and (2.26) are of much lower dimension than equations (2.5) and (2.20), each of the former equations is still an infinite system of IPDEs, and they may still be too expensive to solve numerically. One can make further approximations by considering moments of the density $u_k(t, \boldsymbol{s})$ with respect to the degree k:

$$\mathcal{M}_r(t, \boldsymbol{s}) = \sum_{k=0}^{\infty} k^r u_k(t, \boldsymbol{s})\,. \tag{2.35}$$

In particular, $\mathcal{M}_0$ gives the number density of nodes (for which we obtain a closed equation if $\mathcal{J} \equiv 0$ and $\mathcal{L}^{(1)}$ does not depend on the network structure), and $\mathcal{M}_1$ gives the number density multiplied by the mean degree of a node with state vector $\boldsymbol{s}$. Therefore, $\mathcal{M}_1/2$ gives the number of edges per unit area. It is only possible to obtain a closed system of equations for particular choices of $\mathcal{C}$ and $\mathcal{D}$. In general, one

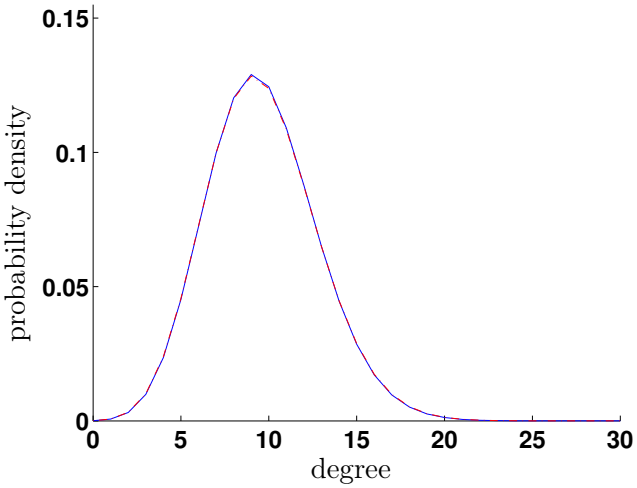

Figure 2.6: Analytical approximation to the degree distribution (solid blue curve) of the latent social-space model [17] versus the result from a kinetic formulation (red dash-dotted curve) using equation (2.16). We uniformly distribute nodes with a social parameter $h \in [0, 125]$. We use the parameter values $n = 1000$, $\alpha = 3$, and $b = 1/2$. The probability of connection and choice of $\mathcal{C}$ is given by equation (2.34). There is no edge deletion (i.e., $\mathcal{D} \equiv 0$), and the system is of constant size (i.e., $\mathcal{J} \equiv 0$). We solve the kinetic equation until final time $T_{\text{end}} = 1$.

needs to truncate the hierarchy of moment equations and then apply another closure assumption by positing an expression for a high-order moment in terms of lower-order moments [66, 67, 89].

※

In the next chapter, we shall pose a model for osteocyte network formation. The work in this chapter serves as the mathematical framework used to analyse the model.

Chapter 3

Modelling Osteocyte Network Formation

To model osteocyte network formation, we have a developed a simple stochastic agent-based model. Our model builds on the mathematical framework by Buenzli to describe osteocyte generation [20]. In Buenzli's original work, osteocytes are located within a growing domain that represents the presence of mineralised bone; osteoblasts are located on the surface of the bone substrate. There are two constitutive processes: (*i*) the bone surface moves with a speed proportional to the surface density of osteoblasts; and (*ii*) osteoblasts differentiate into osteocytes. This work utilised a rate equation approach to hypothesise a relationship between osteocyte number density and rate of osteoblast bone secretion to estimate the differentiation rate of osteoblasts around a Haversian canal[1].

We add to the Buenzli model by allowing for extra structure relating to the osteocyte's dendritic network. We allow for osteocytes to extend dendrites towards the osteoblast layer to signal osteoblast differentiation (we assume these processes occur concurrently). Osteoblasts are also allowed to proliferate and move along the bone surface. We have created this model to investigate the properties of cancer induced bone formation. Here we aim to link osteocyte density and network structure to measurable quantities that may impact these, such as: the rate of osteoid secretion; the rate of osteocyte dendrite growth; the rate of osteoblast to osteocyte differentiation; and the surface density of osteoblasts.

This chapter is arranged as follows. In Section 3.1, we specify our model of bone formation. In Section 3.2, we utilise the approach from Chapter 2 to write down mean-field equations. In Section 3.3, we give details on model parameterisation. In Section 3.4, we give results on two key topics: first, we investigate possible mechanisms for osteoblast differentiation and discuss model selection; and second, we consider model based predictions and put these within the context of zoledronate therapy.

[1] A specific bone formation event observed within cortical bone, and not in trabecular bone as is the case in our work.

3.1 Agent-Based Model Description

Our model is a stochastic agent-based model for the bone formation phase only. The agents are osteocytes or osteoblasts occupying nodes within a spatial network. We model mobile (pre-)osteoblasts (disconnected from the osteocyte network) in front of the deposition front that proliferate and secrete osteoid; (mature) osteoblasts that secrete osteoid and are connected to the osteocyte network; and osteocytes that form dendrites with osteoblasts. The spatial network has pairwise edges between nodes, representing the ability for two cells to communicate; physically this communication is mediated through dendrites. The model consists of the following processes: (*i*) bone secretion; (*ii*) osteoblast differentiation; (*iii*) dendrite growth; (*iv*) (pre-)osteoblast migration; and (*v*) (pre-)osteoblast proliferation (see Figure 3.1). Agents of the same type (osteocytes or osteoblasts) follow the same rules, although each agent may have different properties, e.g., position, number of edges, in addition to type.

The first two processes were accounted for in Buenzli, although network structure was not considered [20]. Bone secretion is carried out by osteoblasts secreting bone in a small region around themselves, resulting in movement of the bone surface. Osteoblasts can also differentiate into osteocytes and become buried, the rate of osteoblast differentiation may depend on how the osteoblast is in communication with the osteocyte network in bone.

For dendrite growth, our model follows the observation in Refs. [76, 116] that dendrites grow away from osteocytes within bone and towards the osteoblast layer on the bone surface. Therefore, osteocytes create edges to osteoblasts, and edges between pairs of osteoblasts are not allowed.

Movement and cell division are included for (pre-)osteoblasts that are disconnected from the osteocyte network. Osteoblasts can move along the bone surface, this is assumed to be approximated by diffusion and is incorporated into the model by means of a position jump process. They are also able to proliferate and divide into two daughter cells.

We make the model description more precise through the introduction of mathematical concepts and notation. Osteoblasts and osteocytes act as nodes in a spatial network. Between pairs of nodes, undirected unweighted edges represent dendrites growing away from osteocytes. The osteocytes occupy an expanding domain $\Omega(t) \subset \mathbb{R}^d$, and osteoblasts are located on sections of the boundary of the domain $B(t) \subset \partial\Omega(t)$. The boundary $B(t)$ moves in the outward normal direction $\boldsymbol{n}(t, \boldsymbol{x})$ for $\boldsymbol{x} \in B(t)$ at velocity $\boldsymbol{u}(t, \boldsymbol{x})$. In Figure 3.2, we give a schematic of a general domain.

For all times $t > 0$, the whole system is described completely by 4 (multidimensional) quantities. First, one must know how many nodes n are present. Second, we specify the cell type ϱ_i for each node $i = 1, \ldots, n$. We must know whether it is an osteoblast (Ob) or an osteocyte (Ocy). Third, each node $i = 1, \ldots, n$ must have an associated position, we write $\boldsymbol{x}_i = (x_1, \ldots, x_d) \in \Omega(t) \cup B(t) \subset \mathbb{R}^d$. Finally, we must know the adjacency matrix of the underlying network (defined in Chapter 2). For our framework in Chapter 2 to be applicable, we allow for the existence of multiedges (multiple edges between the same two nodes) for mathematical tractability. Although as the size of the network becomes large, the probability of multiedges occurring ap-

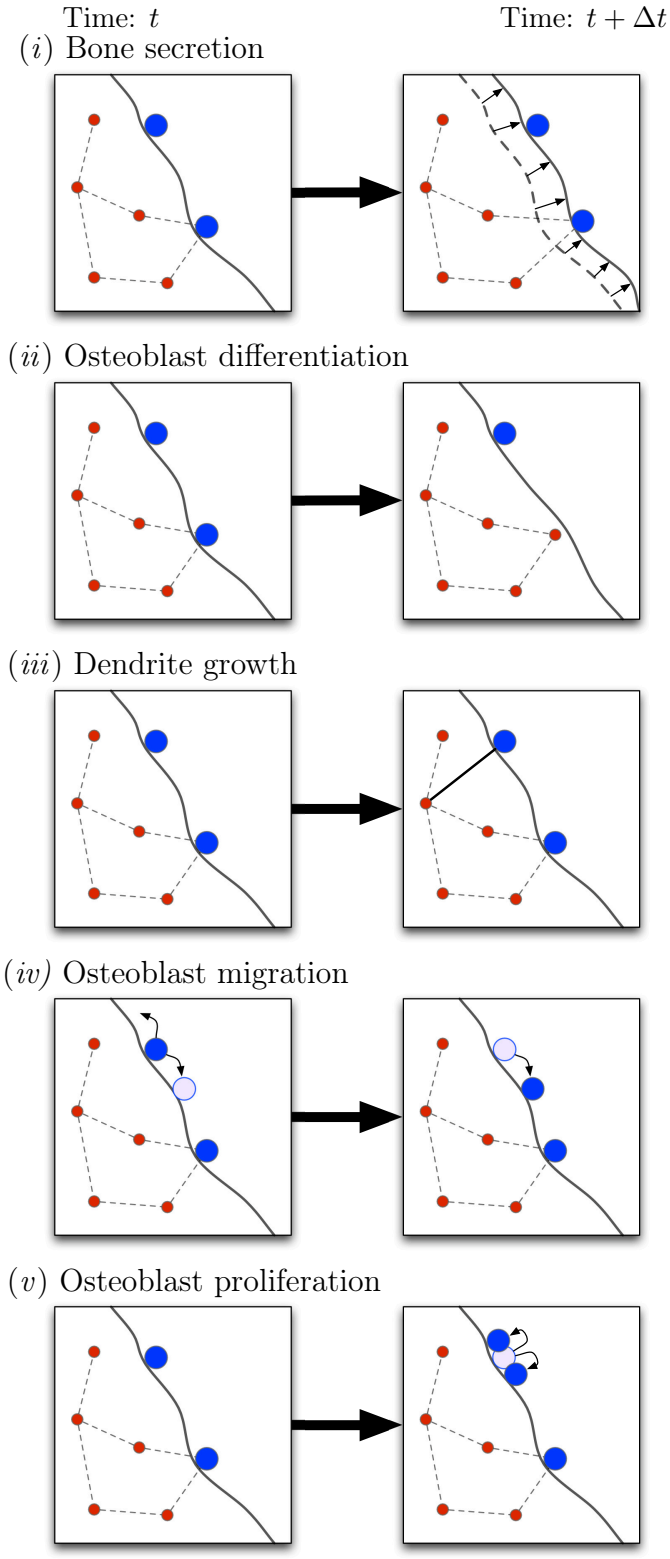

Figure 3.1: Diagrammatic illustration of our model of osteocyte network formation. Osteoblasts are coloured in blue and osteocytes are coloured in red. In a small time step, the following events can occur: (i) bone secretion; (ii) osteoblast differentiation; (iii) dendrite growth; (iv) osteoblast migration; and (v) osteoblast proliferation.

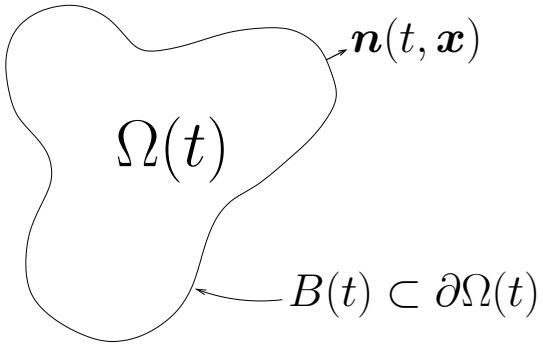

Figure 3.2: Diagram of the domain $\Omega(t)$ in our model of a growing osteocyte network.

proaches zero. Additionally, the mean degree for each node is *a priori* likely to be low, e.g., we estimated the mean osteoblast degree to be ~ 1 (see parameter estimation, Section 3.3).

We now respecify the model given in Figure 3.1 with extra mathematical details. We frequently make use of the phrasing that *events occur at some rate*. This rate will always then refer to the probability of an event happening per unit time (also known as a Poisson process).

(i) *Bone secretion.* The bone surfaces move with normal speed ν depending on the number of nearby osteoblasts. For the diagram shown in Figure 3.2, we write

$$\nu(t,\boldsymbol{x}) = \sum_{i\,:\,\varrho_i=\mathrm{Ob}} S(\boldsymbol{x},\boldsymbol{x}_i) \;\text{ for }\; \boldsymbol{x} \in B(t)\,, \tag{3.1}$$

where the function S specifies the rate of secretion at position $\boldsymbol{x}$ due to an osteoblast at position $\boldsymbol{x}_i$. As osteoblasts can only secrete bone locally, the function $S(\boldsymbol{x},\boldsymbol{y})$ decays for $||\boldsymbol{x}-\boldsymbol{y}|| \gg \iota$ for some characteristic length scale ι. For simplicity, we choose the function

$$S(\boldsymbol{x},\boldsymbol{y}) = \eta\, \exp\left(-\frac{1}{2}\iota^{-2}||\boldsymbol{x}-\boldsymbol{y}||^2\right). \tag{3.2}$$

(ii) *Osteoblast differentiation.* An osteoblast with degree k (or k dendrite structures attached to it), differentiates into an osteocyte at rate D_k. The precise choice of the form of D_k is discussed in Section 3.4.1.

(iii) *Dendrite growth.* Connections are created from osteocytes in $\Omega(t)$ towards the osteoblast layer $B(t)$. We specify that osteocytes at position $\boldsymbol{x} \in \Omega(t)$ can create edges to osteoblasts at position $\boldsymbol{y} \in B(t)$ at rate $\mathcal{C}(\boldsymbol{x},\boldsymbol{y})$. We make the assumption that the rate is proportional to a Gaussian with the argument of distance between $\boldsymbol{x}$ and $\boldsymbol{y}$. An edge is only able to form provided there exists a straight line path within the bone domain $\Omega(t)$ between both nodes. Therefore

$$\mathcal{C}(\boldsymbol{x},\boldsymbol{y}) = \begin{cases} \alpha\, \exp\left(-\frac{1}{2}\beta^{-2}||\boldsymbol{x}-\boldsymbol{y}||^2\right) & (\boldsymbol{x},\boldsymbol{y}) \in P\,, \\ 0 & (\boldsymbol{x},\boldsymbol{y}) \notin P\,, \end{cases} \tag{3.3}$$

Table 3.1: Model functions.

Function name	Symbol and form	Units
Rate of dendrite growth	$\mathcal{C}(\boldsymbol{x},\boldsymbol{y}) = \alpha \exp\left(-\frac{1}{2}\beta^{-2}\|\|\boldsymbol{x}-\boldsymbol{y}\|\|^2\right)$	day^{-1}
See equation (3.3). *Assumption that ability to dendrites from osteocyte to osteoblast is normally distributed.*		
Rate of bone secretion	$S(\boldsymbol{x},\boldsymbol{y}) = \eta \exp\left(-\frac{1}{2}\iota^{-2}\|\|\boldsymbol{x}-\boldsymbol{y}\|\|^2\right)$	$\text{mm}\,\text{day}^{-1}$
See equation (3.1).		
I.C Ob. surface den.	$v_k(t=0) = \tilde{p}\mathbb{1}[\boldsymbol{x} \in \{\omega_0\} \times (0, L_y)]\delta_{k,0}$	mm^{-2}
I.C Ocy. number den.	$w_k(t=0,\boldsymbol{x}) \equiv 0$	mm^{-3}

for constants $\alpha, \beta > 0$, and

$$P := \{(\boldsymbol{x},\boldsymbol{y}) \in \Omega(t) \times B(t) \,|\, s\boldsymbol{x} + (1-s)\boldsymbol{y} \in \Omega \text{ for } s \in [0,1]\}\ . \tag{3.4}$$

(*iv*) *Osteoblast migration.* Osteoblasts disconnected from the network (preosteoblasts, osteoblasts of degree 0) are allowed to move on the bone surface manifold $B(t)$. We model this movement using Brownian motion on the manifold $B(t)$ with corresponding diffusion constant $\kappa_{\text{diff}} > 0$.

(*v*) *Osteoblast proliferation.* Osteoblasts disconnected from the network (preosteoblasts, osteoblasts of degree 0) are allowed to proliferate on the bone surface manifold $B(t)$. As we are not modelling finite volume effects, the new daughter osteoblast will be located at the same position as the parent cell[2]. We specify that once an osteoblast is buried, a proliferation event occurs elsewhere on the bone surface. This new osteoblast has no network structure. Therefore, the total number of osteoblasts is conserved and the mean osteoblast surface density is approximately constant provided there are no large surface deformations. One can interpret this scenario as the case in which (pre-)osteoblasts are in abundance in front of the bone–tissue interface. New osteoblasts then move into the gaps on the bone surface as space becomes available. In the mean-field description, we call the proliferation rate $\mu(t)$.

We list the functional forms underpinning our model in Table 3.1; in the case of the rate of osteoblast differentiation, D_k, we investigate possible choices that represent different dependences on network structure later in Section 3.4.1. Parameter selection is discussed later in Section 3.3.

Our simulation is carried out in two dimensions, but represents a three-dimensional slice, in which the vertical height L_z is the typical distance between osteocyte centres ($L_z \approx 40\,\mu\text{m}$), projected onto two dimensions, see Figure 3.3. The x-direction is the main direction of bone growth, and the area occupied by the bone increases in time. We impose periodicity in the y-direction (orthogonal to bone growth) to avoid artificial boundary effects.

[2]Whilst osteoblasts are tightly packed, they can deform and move around each other. Therefore we do not focus on finite volume effects.

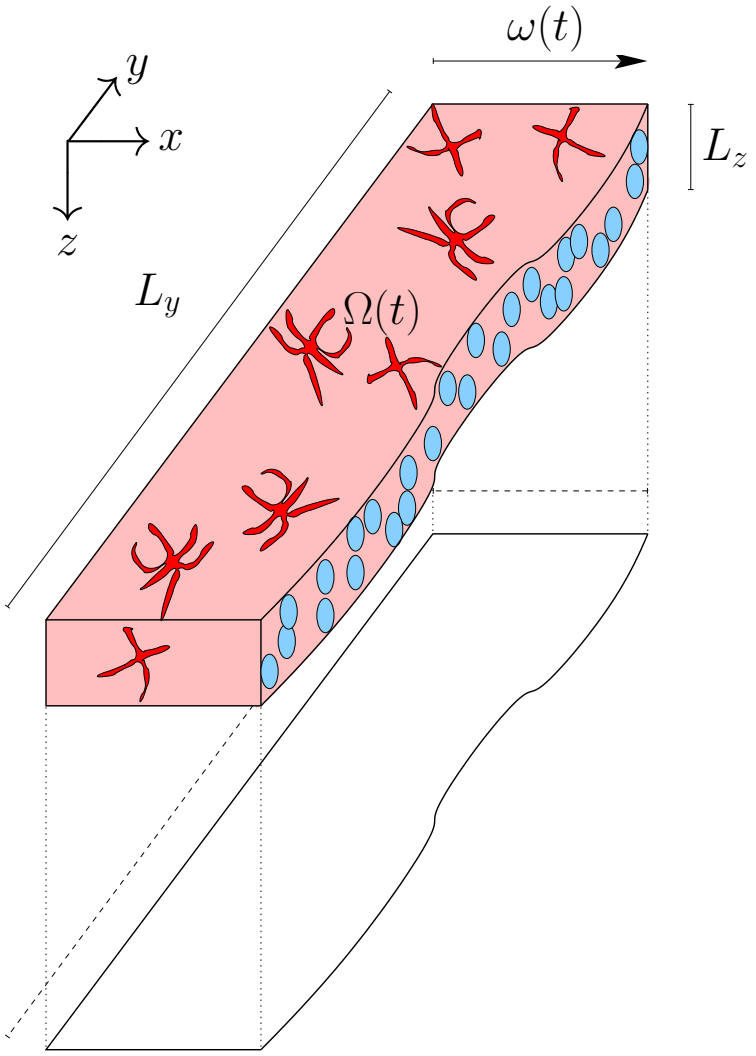

Figure 3.3: Bone slice domain in three dimensions. Osteoblasts are depicted in light blue, osteocytes are shown in red. Two dimensional projection shown below.

In all the simulations, we consider growing a piece of bone after a cement line has been deposited. A cement line is a 1-5 μm region of hypermineralised (and collagen deficient) bone [140] that occurs during the reversal of the bone formation process: when osteoclasts stop resorbing bone, and bone producing osteoblasts start rebuilding. When this cement line is deposited, osteocytes from deep within the bone are not necessarily in communication with osteoblasts on the other side of the cement line [130].

We use the initial condition that there are no old osteocytes with which to communicate (no initial network structure) and there is an initial surface density of $6 \times 10^3\,\mathrm{mm}^{-2}$ osteoblasts that do not have any network structure. Realisations of our stochastic agent-based model are possible via a fixed time step Monte Carlo algorithm (see Appendix C). A single realisation of our model is shown in Figure 3.4.

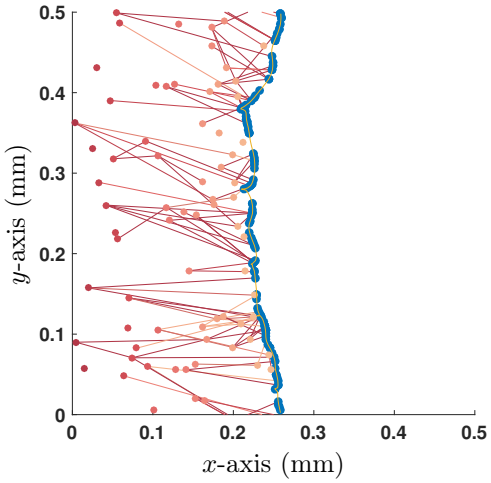

Figure 3.4: Realisation of an osteocyte network formation event (at 365 days) using the Monte Carlo algorithm in Appendix C. Parameters chosen are found in Table 3.2 and Section 3.4.2.

3.2 Mean-Field Description

A single realisation is unrepresentative of the stochastic process, so many simulations must be carried out to work out statistics of the process along with parameterisation. This can be computationally demanding, especially as the system grows in size.

As an alternative to large numbers of simulations, we can utilise mean-field equations. It was shown in Chapter 2 that in the limit as the number of nodes in the network becomes large, one is able to derive a mean-field partial integro-differential equation for the expected number of nodes at a particular position in the domain connected to a fixed number of cells, the Local State Degree Distributions. By solving the IPDE, one can also calculate the degree distribution of the network. Mean-field equations are then amenable to tools from calculus.

Simulations of the stochastic mathematical model suggest that the system is approximately homogeneous in the direction orthogonal to bone growth (see Figure 3.4). In that case, the mean-field equations depend only on x (the direction of bone growth). The solutions of these equations provide spatial profiles perpendicularly to the bone surface of the densities of osteocytes and their network structure. We now derive these mean-field equations, before solving them in Section 3.2.2.

3.2.1 Derivation of Mean-Field Equations

From earlier work in Chapter 2, we can write down differential equations for the LSDD. Previously, we used the expression $u_k(t, \boldsymbol{s})$ as the expected number of particles with degree k and state vector $\boldsymbol{s}$. For the model contained in Section 3.2, our state vector is described by position and cell type, so $\boldsymbol{s} = (\boldsymbol{x}, \varrho)$, and $\varrho \in \{\mathrm{Ob}, \mathrm{Ocy}\}$.

For notational convenience, we write $v_k(t, \boldsymbol{x})$ is the expected number of osteoblasts of degree k with position $\boldsymbol{x}$ at time t, and $w_k(t, \boldsymbol{x})$ as the expected number of osteocytes of degree k with position $\boldsymbol{x}$ at time t. We write the number density of osteoblasts

and osteocytes (respectively) as

$$p(t,\boldsymbol{x}) = \sum_{k=0}^{\infty} v_k(t,\boldsymbol{x})\,, \quad q(t,\boldsymbol{x}) = \sum_{k=0}^{\infty} w_k(t,\boldsymbol{x})\,. \tag{3.5}$$

The osteocytes are present in domain $\Omega(t) \subset \mathbb{R}^d$, and the osteoblasts are present on (a subset of) the boundary of this domain $B(t) \subset \partial\Omega(t)$. The domain boundary moves with normal velocity

$$\boldsymbol{u}(t,\boldsymbol{x}) = \nu(t,\boldsymbol{x})\boldsymbol{n}(t,\boldsymbol{x})\,, \tag{3.6}$$

where $\boldsymbol{n}$ is the normal to $\partial\Omega$. Adapting Stone's derivation of surfactants on moving interfaces [146], our equations become

$$\begin{aligned}\frac{\partial v_k(t,\boldsymbol{x})}{\partial t} + \nabla_S \cdot (\boldsymbol{u}(t,\boldsymbol{x})v_k(t,\boldsymbol{x})) &= -D_k v_k(t,\boldsymbol{x}) \\ &+ \left(\int_{\Omega(t)} \mathcal{C}(\boldsymbol{x},\boldsymbol{y})q(t,\boldsymbol{y})\mathrm{d}\boldsymbol{y}\right)[v_{k-1}(t,\boldsymbol{x}) - v_k(t,\boldsymbol{x})] \\ &+ \delta_{k,0}\left(\kappa_{\text{diff}}\nabla_S^2 v_0(t,\boldsymbol{x}) + \mu(t)v_0(t,\boldsymbol{x})\right)\,,\end{aligned} \tag{3.7}$$

in $B(t)$, and

$$\begin{aligned}\frac{\partial w_k(t,\boldsymbol{x})}{\partial t} &= D_k v_k(t,\boldsymbol{x})\delta_{B(t)}(\boldsymbol{x}) \\ &+ \left(\int_{B(t)} \mathcal{C}(\boldsymbol{x},\boldsymbol{y})p(t,\boldsymbol{y})\mathrm{d}\boldsymbol{y}\right)[w_{k-1}(t,\boldsymbol{x}) - w_k(t,\boldsymbol{x})]\,,\end{aligned} \tag{3.8}$$

in $\Omega(t)$, where $\nabla_S := (I_d - \boldsymbol{n}\boldsymbol{n}^T)\nabla$ is the surface gradient operator[3]. The coupling between equations (3.7) and (3.8) then occurs through the integral terms. Taking the continuum limit in equation (3.1), then

$$\nu(t,\boldsymbol{x}) = \int_{B(t)} S(\boldsymbol{x},\boldsymbol{y})p(t,\boldsymbol{y})\mathrm{d}\boldsymbol{y}\,. \tag{3.9}$$

Assuming a solution homogenous in the y and z directions, we can write the system's domain as: $\Omega(t) = (-\infty, \omega(t)]$; the normal vector as $\boldsymbol{n} = \boldsymbol{e}_x$; and then

$$v_k(t,\boldsymbol{x}) \equiv v_k(t,\omega(t)) \equiv v_k(t)\,, \quad w_k(t,\boldsymbol{x}) \equiv w_k(t,x)\,. \tag{3.10}$$

Under these assumptions, equations (3.7) and (3.8) become

$$\begin{aligned}\frac{\mathrm{d}v_k(t)}{\mathrm{d}t} &= -D_k v_k(t) + \delta_{k,0}\mu(t)v_0(t) \\ &+ \left(\int_{-\infty}^{\omega(t)} K(\omega(t),y)\,q(t,y)\mathrm{d}y\right)[v_{k-1}(t) - v_k(t)]\,,\end{aligned} \tag{3.11}$$

[3]We use standard convention that I_d is the d-dimensional identity matrix.

on the bone surface $B(t) = \{\omega(t)\}$ for kernel $K(x,y) = \alpha\beta L_z\sqrt{2\pi}\exp\left\{-\frac{1}{2}\beta^{-2}|x-y|^2\right\}$, and

$$\frac{\partial w_k(t,x)}{\partial t} = D_k v_k(t)\delta(\omega(t)-x) + K(\omega(t),x)\,p(t)\left[w_{k-1}(t,x) - w_k(t,x)\right], \tag{3.12}$$

in the bone volume $\Omega(t)$. The velocity given by equation (3.9) is then interpreted as an ODE for the position of $\omega(t)$, which is

$$\frac{\mathrm{d}\omega(t)}{\mathrm{d}t} = \kappa_{\text{form}} p(t) = \nu(t), \tag{3.13}$$

for secretion rate $\kappa_{\text{form}} = \eta\iota\sqrt{2\pi}L_z$, which represents the volume of bone secreted per osteoblast per unit time.

3.2.2 Solution Method

We now need to solve equations (3.11)–(3.13). We consider two different scenarios. In the first case (Section 3.2.2.1), we turn the differential equations for $w_k(t,x)$ into integral equations involving the solution to $v_k(t)$ so that we only need to construct a numerical scheme for the ODEs in $v_k(t)$. In the second case (Section 3.2.2.2), we choose the rate of proliferation μ to conserve mass [see equation (3.34)], allowing a travelling wave solution which can be solved analytically. Such a solution is useful both to parameterise the model and to investigate the qualitative effects of perturbations to parameters. We denote the travelling wave solution with a tilde.

3.2.2.1 Time Dependent Problem.

Analysing equations with a moving boundary can be challenging, so we change our coordinate system to fix the location of this boundary by moving from (x,t) to (z,τ), where $z = x - \omega(t)$ and $\tau = t$. Therefore we write equation (3.12) as

$$\frac{\partial w_k(\tau,z)}{\partial \tau} - \omega'(\tau)\frac{\partial w_k(\tau,z)}{\partial z} = K(\omega(\tau),\omega(\tau)+z)\,p(\tau)\left[w_{k-1}(\tau,z) - w_k(\tau,z)\right], \tag{3.14}$$

on $(z,\tau) \in \mathbb{R}_- \times \mathbb{R}_+$ with initial condition

$$w_k(\tau = 0, z) = f_k^{(0)}(z). \tag{3.15}$$

Additionally, we turn the delta function in equation (3.12) into the boundary condition

$$w_k(\tau, z = 0) = \frac{D_k v_k(\tau)}{\omega'(\tau)} = g_k^{(0)}(\tau). \tag{3.16}$$

Using the method of characteristics, with ζ as the characteristic variable, we find

$$\frac{\mathrm{d}\tau}{\mathrm{d}\zeta} = 1, \tag{3.17}$$

$$\frac{\mathrm{d}z}{\mathrm{d}\zeta} = -\omega'(\tau), \tag{3.18}$$

$$\frac{\mathrm{d}w_k}{\mathrm{d}\zeta} = K(\omega(\tau),\omega(\tau)+z)\,p(\tau)\left[w_{k-1} - w_k\right]. \tag{3.19}$$

When $\zeta = 0$, we specify initial and boundary data as a function of ξ. We write

$$\tau = \tau_0(\xi) = \begin{cases} \xi & \text{if} \quad \xi > 0\,, \\ 0 & \text{if} \quad \xi < 0\,, \end{cases} \tag{3.20}$$

$$z = z_0(\xi) = \begin{cases} 0 & \text{if} \quad \xi > 0\,, \\ \xi & \text{if} \quad \xi < 0\,, \end{cases} \tag{3.21}$$

$$w = w_k^{(0)}(\xi) = \begin{cases} g_k^{(0)}(\xi) & \text{if} \quad \xi > 0\,, \\ f_k^{(0)}(\xi) & \text{if} \quad \xi < 0\,. \end{cases} \tag{3.22}$$

Solving equations (3.17)–(3.18), we find that

$$\tau = \begin{cases} \zeta + \xi & \text{if} \quad \xi > 0\,, \\ \zeta & \text{if} \quad \xi < 0\,, \end{cases} \tag{3.23}$$

$$z = \begin{cases} \omega(\xi) - \omega(\zeta + \xi) & \text{if} \quad \xi > 0\,, \\ \omega_0 - \omega(\zeta) + \xi & \text{if} \quad \xi < 0\,. \end{cases} \tag{3.24}$$

Writing

$$\epsilon(\zeta, \xi) = \begin{cases} \int_0^\zeta K(\omega(y+\xi), \omega(\xi)) p(y+\xi) \mathrm{d}y & \text{if} \quad \xi > 0\,, \\ \int_0^\zeta K(\omega(y), \omega_0 + \xi) p(y) \mathrm{d}y & \text{if} \quad \xi < 0\,, \end{cases} \tag{3.25}$$

then

$$w_k(\zeta, \xi) = e^{-\epsilon(\zeta,\xi)} \sum_{j=0}^{k} w_{k-j}^{(0)}(\xi) \frac{\epsilon(\zeta, \xi)^j}{j!}\,. \tag{3.26}$$

Inverting equations (3.23) and (3.24), we obtain

$$\zeta = \begin{cases} \tau - \omega^{-1}[\omega(\tau) + z] & \text{if} \quad z > \omega_0 - \omega(\tau)\,, \\ \tau & \text{if} \quad z < \omega_0 - \omega(\tau)\,, \end{cases} \tag{3.27}$$

$$\xi = \begin{cases} \omega^{-1}[\omega(\tau) + z] & \text{if} \quad z > \omega_0 - \omega(\tau)\,, \\ z + \omega(\tau) - \omega_0 & \text{if} \quad z < \omega_0 - \omega(\tau)\,, \end{cases} \tag{3.28}$$

$$\tag{3.29}$$

and therefore the solution as a function of (z, τ) is given by inserting equations (3.27) and (3.28) into equation (3.26). For the exponent term $\epsilon(z, \tau)$, we can use a change of variables and write

$$\epsilon(z, \tau) = \begin{cases} \int_{\omega^{-1}[\omega(\tau)+z]}^{\tau} K(\omega(h), \omega(\tau) + z) p(h) \mathrm{d}h & \text{if} \quad z > \omega_0 - \omega(\tau)\,, \\ \int_0^\tau K(\omega(h), \omega(\tau) + z) p(h) \mathrm{d}h & \text{if} \quad z < \omega_0 - \omega(\tau)\,. \end{cases} \tag{3.30}$$

and we have also therefore solved our equations for $w_k(t, x)$ given $\omega(t)$ and $v_k(t)$. To solve equation (3.11) for $v_k(t)$, we need to evaluate the integral

$$F(t) := \int_{-\infty}^{\omega(t)} K(\omega(t), y)\, q(t, y) \mathrm{d}y\,. \tag{3.31}$$

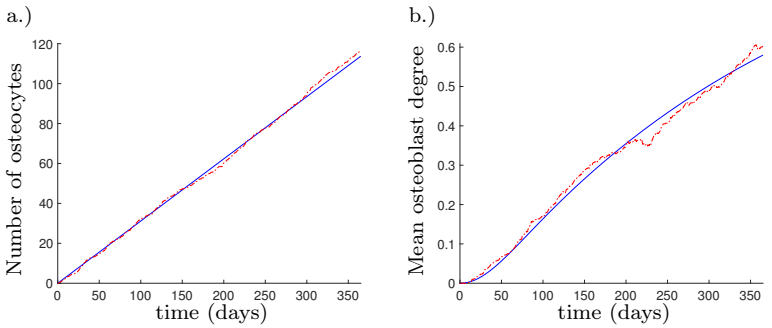

Figure 3.5: a.) Number of osteocytes over time, b.) Mean osteoblast degree over time. Match between solution to mean-field equations (blue) and the average of 5 Monte Carlo simulations (red) after 365 days. Uses null model, details of model set up in Section 3.4.1.1.

By noting that

$$q(t,x) = \sum_{k=0}^{\infty} \begin{cases} g_k^{(0)}(\omega^{-1}(x)) & \text{if} \quad x > \omega_0\,, \\ f_k^{(0)}(x-\omega_0) & \text{if} \quad x < \omega_0\,, \end{cases} \tag{3.32}$$

then we can calculate F as the contribution from the initial condition $f_k^{(0)}$ and the boundary condition $g_k^{(0)}$, therefore

$$\begin{aligned} F(t) = &\sum_{k=0}^{\infty} \int_{-\infty}^{\omega_0} K(\omega(t),x) f_k^{(0)}(x-\omega_0)\mathrm{d}x \\ &+ \sum_{k=0}^{\infty} \int_{\omega_0}^{\omega(t)} K(\omega(t),x) g_k^{(0)}(\omega^{-1}(x))\mathrm{d}x\,. \end{aligned} \tag{3.33}$$

Referring back to the definition of $g_k^{(0)}$ in equation (3.16), we note that our ODEs have become integro-differential equations. These can be solved via finite differences. To demonstrate that we obtain a match between the mean-field equations and Monte Carlo algorithm in Appendix C, in Figure 3.5 we show the match between the average of 5 simulations when compared to the mean-field solution.

3.2.2.2 Osteoblast Mass Conserving Travelling Waves

We now solve the travelling wave problem in the case where the osteoblasts have a constant surface density. This is used to obtain analytic expressions for the dependencies between parameters, the mechanism for osteoblast differentiation (D_k), and variables including: the osteocyte number density, the mean osteoblast degree, and the mean osteocyte degree. These relationships are then later used with experimental measurements to parameterise our model in Sections 3.3 and 3.4.1. To maintain a constant surface density of osteoblasts, we must choose the proliferation rate (of degree zero osteoblasts) as

$$\mu = \mu(\{v_k(t)\}_{k=0}^{\infty}) = \frac{\sum_{k=0}^{\infty} D_k v_k(t)}{v_0(t)}\,, \tag{3.34}$$

where the $v_0(t)$ denominator cancels with the $v_0(t)$ term in equation (3.11) so that

$$\frac{\mathrm{d}p(t)}{\mathrm{d}t} = \sum_{k=0}^{\infty} \frac{\mathrm{d}v_k(t)}{\mathrm{d}t} = 0\,, \tag{3.35}$$

and the total number of osteoblasts does not change over time.

Our system of ODEs then admits a travelling wave solution corresponding to uniform bone growth. We write the travelling wave speed as $\tilde{\nu}$. The solutions of the ODEs now correspond to the constant value $\tilde{v}_k$ with sum $\tilde{p} = \sum_k \tilde{v}_k$. The solutions for the degree k osteocytes have travelling wave profile $\tilde{w}_k(x)$ where $x \to -\infty$ corresponds to the back of the wave (away from the osteoblast front) and $x = \omega_0$ is the front of the wave (where the osteoblasts are located). The total osteocyte density $\tilde{q} = \sum_k \tilde{w}_k(x)$ is then a constant by equation (3.32) as the initial condition $f_k^{(0)}$ does not enter into the solution.

From equation (3.13), the wave speed is given by the relation

$$\tilde{\nu} = \eta\iota L_z\sqrt{2\pi}\tilde{p}\,. \tag{3.36}$$

We now have to solve the algebraic system of equations

$$-D_k\tilde{v}_k + \delta_{k,0}\sum_{l=0}^{\infty} D_l\tilde{v}_l + \tilde{F}[\tilde{v}_{k-1} - \tilde{v}_k] = 0\,. \tag{3.37}$$

Equation (3.37) has recursive solution

$$\tilde{v}_k = \tilde{v}_0\prod_{j=1}^{k}\frac{\tilde{F}}{\tilde{F} + D_j} \quad \text{for } k \geq 1. \tag{3.38}$$

The solution for $\tilde{v}_0$ is then found by asserting

$$\tilde{p} = \sum_{k=0}^{\infty}\tilde{v}_k \tag{3.39}$$

once a specific choice in D_k has been made. The constant $\tilde{F}$ in equation (3.37) can be calculated from equation (3.31) by

$$\begin{aligned}\tilde{F} &= \left[\int_{-\infty}^{\omega_0} K(\omega_0, x)\mathrm{d}x\right]\tilde{q} \\ &= \left[\frac{1}{2}\int_{-\infty}^{\infty}\alpha\beta L_z\sqrt{2\pi}\exp\left(-\frac{x^2}{2\beta^2}\right)\mathrm{d}x\right]\tilde{q} \\ &= \alpha\beta^2\pi L_z\tilde{q}\,.\end{aligned} \tag{3.40}$$

Summing equation (3.16) over k and using equation (3.36), $\tilde{q}$ is given by

$$\tilde{q} = \frac{\sum_{k=0}^{\infty} D_k\tilde{v}_k}{\eta\iota\sqrt{2\pi}L_z\tilde{p}}\,. \tag{3.41}$$

For a given choice in D_k, the mean osteoblast degree can be found by solving equations (3.37) and calculating

$$\langle\tilde{k}\rangle_{\mathrm{Ob}} = \frac{\sum_k k\tilde{v}_k}{\tilde{p}}\,. \tag{3.42}$$

We can also calculate the solution to $\tilde{w}_k(x)$ by using equation (3.26) and assuming steady-state bone formation, that is

$$\tilde{w}_k(x) = e^{-\tilde{\epsilon}(x)} \sum_{j=0}^{k} \tilde{g}_{k-j} \frac{\tilde{\epsilon}(x)^j}{j!}\,, \tag{3.43}$$

where

$$\tilde{g}_k = \frac{D_k \tilde{v}_k}{\tilde{\nu}}\,, \tag{3.44}$$

and

$$\tilde{\epsilon}(x) = \frac{\tilde{p}}{\tilde{\nu}} \int_x^{\omega_0} K(y,x)\mathrm{d}y\,. \tag{3.45}$$

With a solution to $\{\tilde{v}_k\}_{k=0}^{\infty}$, then the mean osteocyte degree can be calculated away from the osteoblast front as

$$\begin{aligned}
\langle \tilde{k} \rangle_{\mathrm{Ocy}} &= \lim_{x\to-\infty} \frac{\sum_{k=0}^{\infty} k\tilde{w}_k(x)}{\tilde{q}} \\
&= \lim_{x\to-\infty} \frac{e^{-\tilde{\epsilon}(x)} \sum_{k=0}^{\infty} k \sum_{j=0}^{k} \tilde{g}_{k-j} \frac{\tilde{\epsilon}(x)^j}{j!}}{\tilde{q}} \\
&= \lim_{x\to-\infty} \frac{e^{-\tilde{\epsilon}(x)} \sum_{k=0}^{\infty} \tilde{g}_k \sum_{j=0}^{\infty} (k+j) \frac{\tilde{\epsilon}(x)^j}{j!}}{\tilde{q}} \\
&= \lim_{x\to-\infty} \frac{\sum_{k=0}^{\infty} k\,\tilde{g}_k + \tilde{q}\,\tilde{\epsilon}(x)}{\tilde{q}} \\
&= \frac{\sum_{k=0}^{\infty} k D_k \tilde{v}_k}{\sum_{k=0}^{\infty} D_k \tilde{v}_k} + \frac{\alpha\beta^2}{\eta\iota}\sqrt{\frac{\pi}{2}}\,.
\end{aligned} \tag{3.46}$$

We then use equations (3.41), (3.42) and (3.46) with different choices in D_k to aid with parameterisation.

3.3 Parameter Estimation

We now parameterise our model, see Table 3.2. Some parameters are model specific depending on D_k, in which case they will be discussed in Section 3.4.1. Parameters were found using data from previously conducted experiments. In cases where the parameter choice was not immediately clear, we provide extra details in the following subsections.

3.3.1 Osteoblast Diffusion Constant, $\kappa_{\mathbf{diff}}$

In the work by Araujo *et. al.* [7], a cellular automaton model was proposed in which migrating osteoblasts were allowed to move on a lattice every time step. With time steps of 6 mins, in the absence of any chemical signalling, osteoblasts moved either up, down, left or right with equal probability. Additionally, it was stated that (from experiments), the speed of a migrating osteoblast was $0.1470\,\mathrm{mm\,day^{-1}}$.

Table 3.2: Model parameters.

Parameter name	Symbol and value	Units	Reference
Osteoblast diffusion constant	$\kappa_{\text{diff}} = 4.5 \times 10^{-5}$	$\text{mm}^2\text{day}^{-1}$	[7]
Value obtained from an interpretation of Araujo et. al. *[7] using the method from Taylor-King* et. al. *[153], see Section 3.3.1.*			
Domain size	$L_y = 0.5$, $L_z = 0.04$.	mm	–
L_y is chosen such that $L_y \gg \beta$. L_z is chosen to be the diameter of an osteoblast (15×10^{-3} mm) plus the mean distance between osteocytes (25×10^{-3} mm). Also note that $\omega_0 = 0$.			
Bone secretion rate parameter	$\eta = 7.27 \times 10^{-5}$	$\text{mm}\,\text{day}^{-1}$	[7]
Parameter estimated by steady-state analysis, see Section 3.3.2			
Dendrite growth shape parameter	$\beta = 25 \times 10^{-3}$	mm	[58]
This value is essentially the standard deviation of the normally distributed rate function [equation (3.3)]. Chosen to be typical distance between osteocytes. The typical distance measured between osteocytes was reported in Ref. [58] to be between 10–40 μm; we use the midpoint in this range. More details in Section 3.3.3			
Bone secretion shape parameter	$\iota = 15 \times 10^{-3}$	mm	[7]
This value is essentially the standard deviation of the normally distributed bone secretion function. Chosen to be the typical diameter of an osteoblast.			
Travelling wave parameters.			
Travelling wave speed	$\tilde{\nu} = 6.56 \times 10^{-4}$	$\text{mm}\,\text{day}^{-1}$	[7]
Used in steady-state travelling wave regime.			
Mean osteoblast degree	$\langle \tilde{k} \rangle_{\text{Ob}} = 1$	No units	[76]
Used in steady-state travelling wave regime. See Section 3.3.4			
Osteoblast surface density	$\tilde{p} = 6 \times 10^3$	mm^{-2}	[21]
Osteoblast surface densities observed within the range 2–10 $\times 10^3$ mm^{-2}. This value was chosen to be the midpoint in this range.			
Osteocyte density	$\tilde{q} = 2.375 \times 10^4$	mm^{-3}	[22]
Used in steady-state travelling wave regime. Osteocyte densities observed within the range 1.90–2.85 $\times 10^4$ mm^{-3}. This value was chosen to be the midpoint in this range.			
Model dependent parameters (see Section 3.4.1).			
Dendrite growth rate	α (model dependent)	day^{-1}	–
See equation (3.3). Free parameter of the model, chosen to maintain constant w_k and v_k profiles, see Section 3.4.1.			
Intrinsic differentiation rate	λ (model dependent)	day^{-1}	–
Free parameter of the model, chosen to maintain constant w_k and v_k profiles, see Section 3.4.1.			
Extrinsic differentiation rate	γ (model dependent)	day^{-1}	–
Free parameter of the model, chosen to maintain constant w_k and v_k profiles, see Section 3.4.1.			

Using the results from Taylor-King[4] *et. al.* [153], it was shown that, for a velocity jump process in n-dimensions with fixed speed S_T, exponentially distributed runs of mean length μ_τ, and with uniformly random selection of new directions, the large time effective diffusion constant is

$$\kappa_{\text{diff}} = \frac{S_T^2 \mu}{n} = \frac{(0.1470)^2(\frac{6}{60}\frac{1}{24})}{2} = 4.50 \times 10^{-5}\,\text{mm}^2\,\text{day}^{-1}\,. \tag{3.47}$$

3.3.2 Bone Secretion Rate Parameter, η

Through analysis of the travelling wave case (see Section 3.2.2.2), one can choose η such that one obtains the (experimentally observed [7]) travelling wave speed of $\tilde{\nu} = 0.656\,\mu\text{m}\,\text{day}^{-1}$. This is done by noting that for a constant wave speed $\tilde{\nu}$, by equation (3.13), we choose that

$$\eta = \frac{\tilde{\nu}}{\iota L_z \tilde{p}\sqrt{2\pi}}\,. \tag{3.48}$$

3.3.3 Dendrite Growth Shape Parameter, β

This value is essentially the standard deviation of the normally distributed rate function [equation (3.3)]. Note that we are not selecting the length of dendrites with this parameter, it specifies how likely a dendrite is to form from an osteocyte within the bone to an osteoblast on the bone surface. The length of the dendrite may change while the osteoblast is located on the bone surface, once it differentiates into an osteocyte, the edge length is fixed.

We choose β to be the typical distance between osteocytes. The typical distance measured between osteocytes was reported in Ref. [58] to be between 10–40 μm; we use the midpoint in this range.

3.3.4 Mean Osteoblast Degree, $\langle\tilde{k}\rangle_{\text{Ob}}$

The only network structure property that we deduced from experimental data was the average number of distinct osteocytes to which a single osteoblast connects. This corresponds to the average node degree of osteoblasts in our connectivity network, $\langle\tilde{k}\rangle_{\text{Ob}}$. We assumed this number to be $\langle\tilde{k}\rangle_{\text{Ob}} = 1$ based on the following estimate. We divide the total number of dendritic processes of an osteoblast, by the redundancy of the physiological network, i.e. by the number of dendritic processes connecting the same osteoblast and osteocyte. Kamioka *et. al.* [76] measured the number of dendritic processes coming from an osteoblast to be 4.8. The redundancy of osteocyte–osteoblast connections can be estimated by dividing the number of processes running from an osteocyte to osteoblasts (26.05) by the number of osteoblasts reached by a single osteocyte (5.7), giving a redundancy of 4.57 [76]. This provides the estimate $\langle\tilde{k}\rangle_{\text{Ob}} \approx 4.8/4.57 \approx 1$. This value is consistent with Kamioka *et. al.*'s observation that they rarely observed osteoblasts that had connections with more than one osteocyte.

[4]Earlier work, not in thesis.

We note here that there are not many studies reporting these kinds of measurements. Marotti *et. al.* [100] have reported the number of dendrites coming from an osteoblast to range from 9.4 to 20.9 in four osteoblasts (so ~ 13.6 on average). If this figure is used instead, $\langle \tilde{k} \rangle_{\mathrm{Ob}} \sim 3$.

3.4 Results and Predictions

3.4.1 Selection of Differentiation Mechanism

We wish to investigate the effects of different model choices for the rate of osteoblast to osteocyte differentiation, D_k. Currently we wish to determine the implication of this rate depending on the degree k (recall this corresponds to the number of osteocytes in communication with the osteoblast).

For a given surface density of osteoblasts, the volumetric density of inclusions embedded in a tissue during appositional growth is determined by two dynamic processes: the rate of differentiation and the tissue growth rate [20]. If the rate of osteoblast burial is identical for all osteoblasts at a given location, i.e., D_k is independent of k ($D_k \equiv \hat{D}$), then the density of osteocytes generated is given by

$$\tilde{q} \equiv \frac{\hat{D}\,\tilde{p}}{\tilde{\nu}} = \frac{\hat{D}}{\kappa_{\mathrm{form}}}, \tag{3.49}$$

where $\hat{D}$ is the burial rate, i.e., the probability per unit time for a single osteoblast to become embedded as an osteocyte, and $\tilde{\nu} = \kappa_{\mathrm{form}}\tilde{p}$ is the normal velocity of the bone interface [20] where κ_{form} is the rate of bone deposition per osteoblast. If the rate of osteoblast burial depends additionally on the number of connections k they have with osteocytes, the density of osteocytes generated sums up the contributions of all k-degree osteoblasts

$$\tilde{q} \equiv \sum_{k=0}^{\infty} \frac{D_k \tilde{v}_k}{\tilde{\nu}}. \tag{3.50}$$

In contrast to equation (3.49), the density of osteocytes given by equation (3.50) depends explicitly on the population of osteoblasts that generated it, through the proportions $v_k/\tilde{p}$ of k-degree osteoblasts. Notice that this expression determines the density of osteocytes created at the moving bone deposition front. It does not account for subsequent bulk processes such as osteocyte apoptosis, nor for bone resorption or remodelling, which may remove and replace osteocytes. Modelling such processes would lead to further spatio-temporal dependences of $\tilde{q}$ [92]. In the present work, we only consider an uninterrupted bone formation process.

Many parameters we assume to be "fixed" for the purpose of model selection. This is because these parameters refer to length scales that impact the bone formation process independently of the differentiation mechanism. To explore different differentiation mechanisms we alter both: the rate of dendrite growth, α, and the mechanism behind the rate of osteoblast differentiation, D_k. We discuss the differences between differentiation mechanisms in Section 3.4.1.4.

3.4.1.1 No Network Influence: Null Model

Our null hypothesis specifies that there is no feedback between network structure and osteoblast to osteocyte differentiation. Mathematically speaking, the degree of each osteoblast (the number of osteocytes each osteoblast is in communication with) does not impact the rate of osteoblast differentiation; we write

$$D_k^{(\text{null})} \equiv \hat{D}\,, \tag{3.51}$$

for all values of $k = 0, 1, \ldots, \infty$.

When considering the parameters in Table 3.2, and our choice of osteoblast differentiation, $D_k = D_k^{(\text{null})}$, we have two undefined (free) parameters in our model $(\hat{\alpha}, \hat{D})$ and two unused observations: the mean degree of an osteoblast $\langle \tilde{k} \rangle_{\text{Ob}} = 1$; and the number density of osteocytes $\tilde{q} = 2.375 \times 10^4\,\text{mm}^{-3}$. By carrying out mathematical analysis in the travelling wave regime, one can insert the choice of D_k in equation (3.51) into equations (3.38)–(3.39) to then solve equations (3.41) and (3.42).

First, we solve equations (3.38)–(3.39) to find that the osteoblast degree is geometrically distributed

$$\tilde{v}_k = \tilde{p}(1-r)r^k\,, \qquad \text{for } r = \frac{\tilde{F}}{\tilde{F} + \hat{D}}\,. \tag{3.52}$$

The osteocyte density is calculated from equation (3.41) as

$$\tilde{q} = \frac{\sum_{k=0}^{\infty} D_k \tilde{v}_k}{\eta\iota\sqrt{2\pi}L_z\tilde{p}} = \frac{\hat{D}}{\eta\iota\sqrt{2\pi}L_z}\,, \tag{3.53}$$

which is restating equation (3.49). Using the definition in equation (3.42), we calculate

$$\begin{aligned}
\langle \tilde{k} \rangle_{\text{Ob}} &= \frac{1}{\tilde{p}} \sum_{k=0}^{\infty} k\tilde{v}_k = (1-r)\sum_{k=0}^{\infty} kr^k \\
&= \frac{r}{1-r} \\
&= \frac{\tilde{F}}{\hat{D}} \\
&= \frac{\alpha\beta^2\pi L_z \tilde{q}}{\hat{D}} \\
&= \frac{\hat{\alpha}\beta^2}{\eta\iota}\sqrt{\frac{\pi}{2}}\,,
\end{aligned} \tag{3.54}$$

using equations (3.52), (3.40) and (3.53). We can then determine the parameters $\hat{\alpha} = 1.39 \times 10^{-3}\,\text{day}^{-1}$ and $\hat{D} = 2.59 \times 10^{-3}\,\text{day}^{-1}$.

For completeness, we can also calculate the mean osteocyte degree, starting from

equation (3.46) and substituting in $D_k^{(\text{null})}$

$$\begin{aligned}\langle\tilde{k}\rangle_{\text{Ocy}} &= \frac{\sum_{k=0}^{\infty} kD_k\tilde{v}_k}{\sum_{k=0}^{\infty} D_k\tilde{v}_k} + \frac{\alpha\beta^2}{\eta\iota}\sqrt{\frac{\pi}{2}} \\ &= \frac{\hat{D}\sum_{k=0}^{\infty} k\tilde{v}_k}{\hat{D}\sum_{k=0}^{\infty} \tilde{v}_k} + \frac{\alpha\beta^2}{\eta\iota}\sqrt{\frac{\pi}{2}} \\ &= \langle\tilde{k}\rangle_{\text{Ob}} + \frac{\alpha\beta^2}{\eta\iota}\sqrt{\frac{\pi}{2}} = \frac{\hat{\alpha}\beta^2}{\eta\iota}\sqrt{2\pi}\,. \end{aligned} \tag{3.55}$$

Quite remarkably when D_k is independent of k, for any values of the other parameters $\langle\tilde{k}\rangle_{\text{Ocy}} = 2\langle\tilde{k}\rangle_{\text{Ob}}$.

By changing the rate of osteoblast to osteocyte differentiation, $\hat{D}$, we observe a linear relationship with the number density of osteocytes buried, $\tilde{q}$ [see equation. (3.49)]. Changing the rate of dendrite formation, $\hat{\alpha}$, leads to a linear relationship with the mean osteoblast degree, $\langle\tilde{k}\rangle_{\text{Ob}}$, and the mean osteocyte degree, $\langle\tilde{k}\rangle_{\text{Ocy}}$. These effects are decoupled — changing the rate of osteoblast to osteocyte differentiation rate, $\hat{D}$, has no effect on the network structure, and changing the rate of dendrite formation, $\hat{\alpha}$, has no effect on the osteocyte density, $\tilde{q}$. This will not be the case when osteoblast burial is coordinated by the osteocyte network.

The null hypothesis is contestable due to the following experimental observations. First, as reviewed in Ref. [53], osteoblasts can be signalled to adhere to the mineral matrix and grow dendrites (subsequently differentiating) via the insulin-like growth factor 1 (IGF-1). Second, sclerostin secreted by osteocytes has been shown to act briefly as an inhibitory signal to prevent excessive osteoblast differentiation and allowing for coordinated osteocyte network formation [127]. Note that in Ref. [127], sclerostin was stained for and observable within the osteocyte's dendritic protrusions. These experiments, along with the three-dimensional scans taken by Kamioka *et. al.* [76], strongly suggest that osteocytes signal osteoblast differentiation through the extension of dendrites towards the osteoblast layer. This corresponds to a rejection of the null hypothesis. However, one cannot rule out some intrinsic differentiation ability of mature osteoblasts. The reason being due to the existence of cement lines where osteocytes on either side may not be in communication. Therefore, when regarding the rate at which osteoblasts differentiate into osteocytes, one should expect an intrinsic differentiation rate, and an additional contribution from other osteocytes.

3.4.1.2 Modelling Network Effects

Depending on the varying contribution between intrinsic osteoblast differentiation signals, and extrinsic differentiation signals from the osteocyte network, the extrinsic network can either have an excitatory or inhibitory effect on osteoblast differentiation.

We consider differentiation rates of the form

$$D_k = \begin{cases} \lambda & \text{if} \quad k = 0\,, \\ \lambda + f(k) & \text{if} \quad k \geq 1\,, \end{cases} \tag{3.56}$$

where λ is the intrinsic rate of osteoblast differentiation and $f = f(k)$ is the contribution to osteoblast differentiation for an osteoblasts connected to k osteocytes. When $f > 0$ the network has an excitatory effect on osteoblast differentiation, and when $f < 0$ the network has an inhibitory effect on osteoblast differentiation. To prevent negative differentiation rates, we require that

$$\lambda > 0\,, \text{ and } \lambda + f(k) \geq 0\,, \quad \forall k \geq 1. \tag{3.57}$$

In the main text, we consider only the case where f is a constant (see Section 3.4.1.3). Other very simple choices in f that only have 1 free parameter are considered in Appendix D (we call this free parameter γ). It should be noted that choices of f that have non-monotonic behaviour (i.e., a local maximum/minimum exists) can lead to non-monotonic profiles in q.

Our technique for parameter identification relies on the use of our mean-field equations and is as follows. We choose a base rate of intrinsic osteoblast differentiation such that $\lambda \neq \hat{D}$, leaving 2 free parameters α and γ. We then determine the free parameters by asserting that $\langle \tilde{k} \rangle_{\mathrm{Ob}} = 1$ and $\tilde{q} = 2.375 \times 10^4\,\mathrm{mm}^{-3}$ in the travelling wave regime. By making these assertions, if $\lambda < \hat{D}$, then the network contribution will always have an excitatory effect on osteoblast differentiation; and if $\lambda > \hat{D}$, then the network contribution will always inhibit osteoblast differentiation.

3.4.1.3 Proposed Mechanism: Switch-like Influence

Switch-like mechanisms are frequently found in biology [32]; at a cellular level this includes mechanisms for proliferation and differentiation [163]. For a switch-like contribution to the osteoblast differentiation rate, we proposed the form of D_k as

$$D_k^{(\mathrm{swt})} = \begin{cases} \lambda & \text{if} \quad k = 0\,, \\ \lambda + \gamma & \text{if} \quad k \geq 1\,, \end{cases} \tag{3.58}$$

where γ is a constant. The interpretation of equation (3.58) is that: if the osteoblast on the bone surface is not in communication with any other osteocytes ($k = 0$) then it has an intrinsic differentiation rate λ; alternatively if osteoblasts are contact with one or more osteocytes, there is an induced differentiation rate $\lambda + \gamma$, where γ is the contribution from the dendritic network.

First, we solve equations (3.38)–(3.39) to using our choice of D_k in equation (3.58). As in the null model, we find that the osteoblast degree is geometrically distributed

$$\tilde{v}_k = \tilde{p}(1-r)r^k\,, \qquad \text{for } r = \frac{\tilde{F}}{\tilde{F} + \lambda + \gamma}\,. \tag{3.59}$$

Using the solution for $\tilde{v}_k$, we find that the mean osteoblast degree is linearly related

to the osteocyte number density

$$\begin{aligned}\langle\tilde{k}\rangle_{\mathrm{Ob}} &= \frac{r}{1-r}\\ &= \frac{\tilde{F}}{\lambda+\gamma}\\ &= \frac{\alpha\beta^2\pi L_z\tilde{q}}{\lambda+\gamma}\,,\end{aligned} \tag{3.60}$$

by equations (3.59) and (3.40). We now use the choice of D_k in equation (3.58) to calculate $\tilde{q}$ from equation (3.41)

$$\begin{aligned}\tilde{q} &= \frac{\sum_{k=0}^{\infty} D_k\tilde{v}_k}{\eta\iota\sqrt{2\pi}L_z\tilde{p}}\\ &= \frac{\lambda\tilde{v}_0+(\lambda+\gamma)(\tilde{p}-\tilde{v}_0)}{\eta\iota\sqrt{2\pi}L_z\tilde{p}}\\ &= \frac{\lambda(1-r)+(\lambda+\gamma)r}{\eta\iota\sqrt{2\pi}L_z}\\ &= \frac{\lambda(\lambda+\gamma)+(\lambda+\gamma)\tilde{F}}{(\eta\iota\sqrt{2\pi}L_z)(\tilde{F}+\lambda+\gamma)}\\ &= \frac{\lambda(\lambda+\gamma)+(\lambda+\gamma)\alpha\beta^2\pi L_z\tilde{q}}{(\eta\iota\sqrt{2\pi}L_z)(\alpha\beta^2\pi L_z\tilde{q}+\lambda+\gamma)}\,,\end{aligned} \tag{3.61}$$

by equations (3.58), (3.60), (3.59) and (3.40). Thus we have a quadratic equation for $\tilde{q}$. Using (3.60), the corresponding quadratic equation for $\langle k\rangle_{\mathrm{Ob}}$ is

$$\langle\tilde{k}\rangle_{\mathrm{Ob}}^2+(1-a)\langle\tilde{k}\rangle_{\mathrm{Ob}}-ab=0\,,\quad \text{for}\quad a=\frac{\alpha\beta^2}{\eta\iota}\sqrt{\frac{\pi}{2}}\,,\quad b=\frac{\lambda}{\lambda+\gamma}\,, \tag{3.62}$$

and by equation (3.60) one can find the corresponding equation for $\tilde{q}$. Note that since $a>0$ and $0<b<1$, there is exactly one positive real root to the quadratic in equation (3.62) (we do not give the resulting formula).

Suppose one now asserts that the intrinsic differentiation rate λ contributes half the total rate of osteoblast to osteocyte differentiation rate of the null model (so $\lambda=\hat{D}/2$). Then one is able to determine that $\alpha=2.08\times10^{-3}\,\mathrm{day}^{-1}$ and $\gamma=2.59\times10^{-3}\,\mathrm{day}^{-1}$. Another option would be for an inhibitory contribution, in which case we can set $\lambda=3\hat{D}/2$, and then $\alpha=6.96\times10^{-3}\,\mathrm{day}^{-1}$ and $\gamma=-2.60\times10^{-3}\,\mathrm{day}^{-1}$.

Note that we can use the formula for $\tilde{F}$ in equation (3.40) to calculate the mean osteocyte degree as

$$\begin{aligned}\langle\tilde{k}\rangle_{\mathrm{Ocy}} &= \frac{\sum_{k=0}^{\infty} kD_k\tilde{v}_k}{\sum_{k=0}^{\infty} D_k\tilde{v}_k}+\frac{\alpha\beta^2}{\eta\iota}\sqrt{\frac{\pi}{2}}\\ &= \frac{(\lambda+\gamma)\tilde{p}(1-r)\sum_{k=1}^{\infty} kr^k}{\lambda(1-r)\tilde{p}+(\lambda+\gamma)r\tilde{p}}+\frac{\alpha\beta^2}{\eta\iota}\sqrt{\frac{\pi}{2}}\\ &= \frac{\tilde{F}(\lambda+\gamma+\tilde{F})}{(\lambda+\gamma)(\lambda+\tilde{F})}+\frac{\alpha\beta^2}{\eta\iota}\sqrt{\frac{\pi}{2}}\,.\end{aligned} \tag{3.63}$$

Note there is consistency that the solutions to equations (3.61)–(3.63) agree with the solutions to equations (3.53)–(3.55) when $\gamma = 0$.

3.4.1.4 Discussion on Differentiation Mechanism

In Figure 3.6, we plot the osteocyte density profile, the mean osteoblast degree over time, and the mean osteocyte degree over time using equations (3.11)–(3.13) for 3 proposed choices of D_k: the null model, excitatory network contributions, and inhibitory network contributions. We note that in the right panel of Figure 3.6 (showing mean osteocyte degree), the mean osteocyte degree decreases at the bone deposition front as new edges are being created at this location.

Figure 3.6 shows that when considering all 3 models, it takes approximately 1 year to get to the desired osteocyte density. Although this timescale is too long (one would expect it to be in the order of months), it is the correct order of magnitude. We see similar results for the mean osteoblast degree, except that inhibitory contributions to osteoblast differentiation require more time for the osteoblasts to reach the steady-state degree distribution. The main means for differentiation between models is the resulting mean osteocyte degree profile. Keeping $\tilde{p}$, $\tilde{q}$, $\langle\tilde{k}\rangle_{\text{Ob}}$ fixed, excitatory network contributions to osteoblast differentiation leads to more connected osteocyte networks, and inhibitory network contributions lead to less connected networks.

Capturing network structure and choosing a model that is "correct" seems to be difficult. For instance, the mean osteoblast degree profile seems to take a long period of time before settling to the steady-state mean osteoblast degree of $\langle\tilde{k}\rangle_{\text{Ob}} = 1$. One assumption we have made throughout our model selection process was that the osteoblast surface density was approximately constant. It may be the case is that this surface density changes in time. Were it the case that the surface density of osteoblasts was initially at a higher density before decreasing, in the context of our model, it would speed up the timescales until a steady-state travelling wave profile was reached.

3.4.2 Changing Model Parameters and Visualisations

By varying the parameters of the model, we are able to alter the osteocyte network morphology. Using the analytic expressions in Section 3.2.2.2 for the travelling wave solutions, we summarise the results of single parameter changes in Table 3.3. A few specific examples of realisations of the stochastic process are shown in Figure 3.7. For these, we use the Monte Carlo algorithm in Appendix C, the parameters given in Table 3.2, and the function forms in Table 3.1. The choice in osteoblast differentiation uses the switch mechanism in Section 3.4.1.3 ($D_k = D_k^{(\text{swt})}$) with the inhibitory parameter choice.

Of particular interest is the observation that changing model parameters can have different effects depending on whether the network contribution activates or inhibits osteoblast differentiation. From our discussion in Section 3.4.1.1, inhibitory network contributions to osteoblast differentiation seem more likely in the presence of sclerostin, and excitatory network contributions may also be possible via IGF-1. Un-

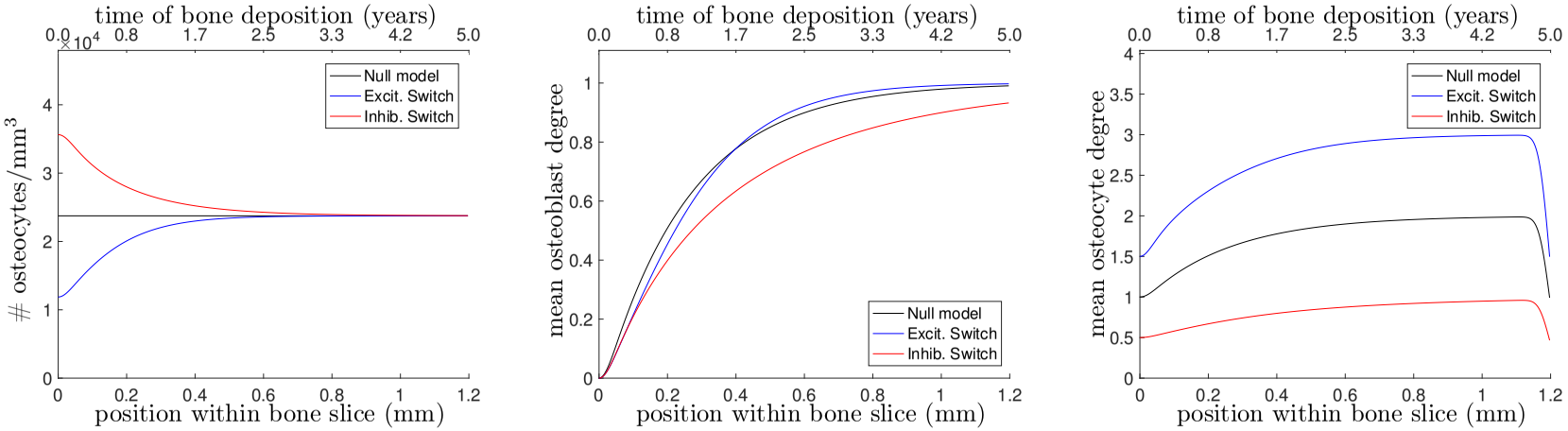

Figure 3.6: (Left) Osteocyte density profile $[q(t, x = \tilde{\nu}t)]$, (middle) mean osteoblast degree over time $[\langle k(t = \tilde{\nu}t)\rangle_{\mathrm{Ob}}]$, and (right) mean osteocyte degree over time $[\langle k(t = \tilde{\nu}t)\rangle_{\mathrm{Ocy}}]$ when solving equations (3.7)–(3.8). The black line shows the null model, the blue line shows the excitatory switch model, and the red line shows the inhibitory switch model.

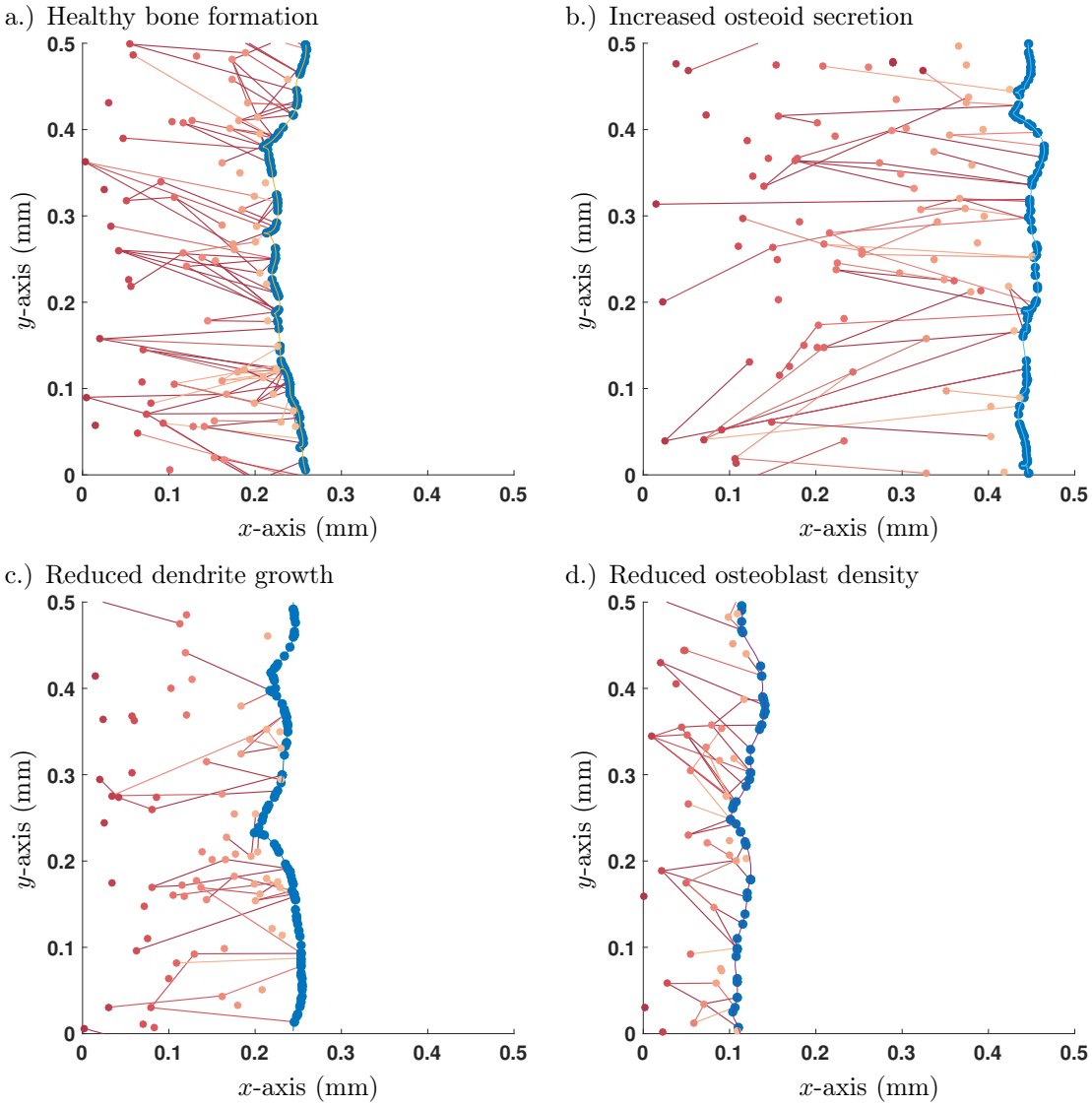

Figure 3.7: Single simulation visualisations of bone growth model with different parameter choices: a.) Healthy parameter set (as shown in Table 3.2); b.) Increased osteoid secretion ($\eta \to 2\eta$); c.) Reduced dendrite growth ($\alpha \to \alpha/2$); d.) Reduced osteoblast surface density ($\tilde{p} \to \tilde{p}/2$). Osteoblast are colored in blue and osteocytes (and their network connections) are in red; darker shades of red denote osteocytes that were buried earlier in time. All simulations are shown after 365 days.

fortunately at this juncture, it is not yet known to what extent each mechanism contributes to network signalling of osteoblast differentiation, therefore we consider both excitatory and inhibitory scenarios.

Whilst many parameters change the density of osteocytes, only α (the rate of dendrite growth) and η (the rate of bone formation) can change the mean osteocyte degree. Therefore, altering the rate of osteoblast differentiation (parameters λ and γ) changes the osteocyte density (variable $\tilde{q}$), but not the degree of these newly formed osteocytes (variable $\langle\tilde{k}\rangle_{\mathrm{Ocy}}$).

In Table 3.3, we also show the results for the first moment $\widetilde{\mathcal{M}}_1 = \tilde{q} \times \langle\tilde{k}\rangle_{\mathrm{Ocy}}/2$ which is the number of edges per unit area[5]. With India ink stained histology slides (providing the stain takes to the sample), dendrites will appear as a black blur. The intensity of the stain is then a measure of $\widetilde{\mathcal{M}}_1$. Therefore, even if the resolution of the histology image is not high enough to estimate the mean number of dendrites per osteocyte, $\langle k\rangle_{\mathrm{Ocy}}$ (or a proxy like the lacunae shape), it may still be possible to obtain an estimate of $\widetilde{\mathcal{M}}_1$.

3.4.3 Zoledronate Study

Breast cancer is known to be osteolytic and suppresses osteoblast proliferation and maturation. When applied as a therapy for breast cancer, the zoledronate treatment allows for recovery of osteocyte number density. The zoledronate treatment is known to improve osteoblast proliferation and maturation while simultaneously killing osteoclasts. We remind the reader that the zoledronated treated bone is brittle compared to healthy bone, which is suggestive of poor osteocyte network formation.

Changing the proliferation ability of osteoblasts will change the osteoblast surface density. Our analysis suggests this will change the quantity of bone produced, but not the network structure. In our model, changing the process of maturation corresponds to changing either: the mechanism behind osteoblast differentiation (parameters λ, γ), or changing the rate of dendrite growth (parameter α).

From our discussion in Section 1.1.4, under (BCa) cancerous conditions osteocytes have fewer dendritic connections to the remaining osteocyte network structure (and lower osteocyte density) — and therefore the mean osteocyte degree is reduced.

To achieve a simultaneous decrease in osteocyte density and mean osteocyte degree, one would either have to: decrease the rate of dendrite growth if excitatory switch model configuration; or increase the rate of bone secretion per osteoblast. Drastically increasing the rate of bone secretion per osteoblast seems unlikely from a mechanistic point of view as there are physical limits on the rate of bone synthesis. This suggests that reducing the rate of dendrite growth may be the most likely mechanism.

Given that the zoledronate treatment only partially restores healthy bone, it seems likely that either the intrinsic or extrinsic rate of osteoblast differentiation is targeted. Exactly which is not possible to specify at this juncture without extensive experimental data regarding the osteocyte network.

[5]Note the factor of 2 compared to the use of $\mathcal{M}_1$ in Chapter 2.

Table 3.3: Prediction summary. In the far left hand column, we list parameters that we consider increasing and in the right hand columns, we list observables responding to the parameter change. We use the notation that ($\uparrow$) denotes an increase, ($\downarrow$) denotes a decrease and ($-$) signifies no change. Decreasing the parameters in the far left hand column will reverse the directions of the arrows.

Increased parameter ($\uparrow$)	Symbol	$\tilde{q}$	$\tilde{\nu}$	$\langle\tilde{k}\rangle_{\mathrm{Ob}}$	$\langle\tilde{k}\rangle_{\mathrm{Ocy}}$	$\widetilde{\mathcal{M}}_1$
Rate of bone secretion	η	$\downarrow$	$\uparrow$	$\downarrow$	$\downarrow$	$\downarrow$
Surface osteoblast density	$\tilde{p}$	$-$	$\uparrow$	$-$	$-$	$-$
Osteoblast migration speed	κ_{diff}	$-$	$-$	$-$	$-$	$-$
Excitatory switch model configuration.						
Intrinsic rate of osteoblast differentiation	λ	$\uparrow$	$-$	$\uparrow$	$-$	$\uparrow$
Network contribution rate of osteoblast differentiation	γ	$\uparrow$	$-$	$\downarrow$	$-$	$\uparrow$
Rate of dendrite growth	α	$\uparrow$	$-$	$\uparrow$	$\uparrow$	$\uparrow$
Inhibitory switch model configuration.						
Intrinsic rate of osteoblast differentiation	λ	$\uparrow$	$-$	$\downarrow$	$-$	$\uparrow$
Network contribution rate of osteoblast differentiation	γ	$\uparrow$	$-$	$\downarrow$	$-$	$\uparrow$
Rate of dendrite growth	α	$\downarrow$	$-$	$\uparrow$	$\uparrow$	$\uparrow$

To summarise, using our model along with biological reasoning suggest that: breast cancer alters how dendrites form; and zoledronate therapy is partially restorative by targeting the osteoblast to osteocyte differentiation mechanism.

3.4.4 Final Remarks: Implications for Cancerous Bone Growth

When one observes cancerous osteocyte networks, it appears osteocytes are either over differentiated (excessive dendrite growth) or underdeveloped (diminished dendrite growth). Additionally, the osteocyte number density tends to decrease.

With experimental data that give information about network structure (e.g., transmission electron microscopy, India ink histology stains), one should be able to approximately measure at least 2 of 3 quantities: the number of osteocytes present (quantitative estimate); whether the osteocytes are over-differentiated or underdeveloped (qualitative estimate); and finally the density of dendrites (quantitative estimate). Therefore, we should be able to compare a pathological bone slide to a (healthy) control slide and determine differences between: the osteocyte number density (q); the mean osteocyte degree ($\langle \tilde{k} \rangle_{\mathrm{Ocy}}$); and the density of dendrites ($\widetilde{\mathcal{M}}_1$).

Our model predicts that:

a.) If all 3 quantities (osteocyte number density, mean osteocyte degree, and dendrite area) have increased (resp. decreased), this corresponds to either: osteoblasts on the bone surface producing too little (resp. too much) osteoid when compared healthy bone; or that the rate of dendrite growth has increased (resp. decreased) in the excitatory switch model configuration. Distinguishing between these two effects will likely be difficult. However, when it is the case that osteoblasts are producing too little osteoid, one would expect to see greater quantities of mineralisation because the bone formation process occurred slower. It seems unlikely the rate of bone secretion could be drastically increased much due to limits on the rate of bone synthesis.

b.) If the osteocyte number density has increased (resp. decreased) with an opposing decrease (resp. increase) in $\langle \tilde{k} \rangle_{\mathrm{Ocy}}$ or $\widetilde{\mathcal{M}}_1$, then this must correspond to the rate of dendrite growth changing but in the inhibitory switch model configuration.

c.) If the osteocyte density increases (or decreases), but then the level of cell differentiation is approximately the same, our model suggests this relates to a change in the rate of osteoblast differentiation.

Chapter 4

Simulated Ablation for Detection of Cells Impacting Paracrine Signalling in Histology

We now depart from spatial networks and cancerous bone formation, and move onto the topic of histology analysis. After posing an approach to quantify paracrine signalling, we interpret our method in the context of a toy model where cells are agents in an interacting particle system. Previously, we used mean-field approaches to calculate summary statistics of the underlying system. This is no longer appropriate as we are now considering heterogeneous agents where the fluctuations indicate interesting behaviour.

※

Using mathematical modelling, we present a quantitative approach to calculate how each cell alters the local microenvironment using only histological images. Our approach allows us to determine two things. First, to what degree a cell is either absorbing from, or secreting into, a local diffusible signalling environment; and second, how much of the observed staining intensities are explainable via diffusion. Thus given a histology slide stained to measure the expression of a specific protein, we are able to quantify the extent to which that protein contributes to microenvironmental signalling. The method presented is based on postulating that expression levels (as determined by staining intensity) of targets of analyses are determined by a field of secreted environmental signalling molecules. This signalling field (SF) abstraction integrates all of the secreted factors that impact the expression of a particular phenotypic trait in a paracrine manner (cytokines, gases, metabolites). Our approach ignores physical interactions between cells (e.g., force interactions through the ECM) and relies on availability of multi-channel staining data.

Substantial mathematical modelling efforts have been focused on understanding the impact of the microenvironment on phenotypic heterogeneity using biophysical principles; common themes include diffusion of cytokines, and construction of chemical reaction networks. Efforts at modelling the microenvironment in a spatial setting

have largely been focused on forward modelling, where one makes assumptions and rules for a model, initiates the model in some starting configuration, and then evolves it forward in time. Due to the complexity of the models involved, cellular automaton approaches have often been utilised [3–5, 13, 125]. Such approaches, depending on the complexity of the rules built into the model, are able to reproduce many experimental/clinical observations, and in some cases are capable of making experimentally validated predictions [7]. Unfortunately, mathematical modelling approaches are limited by: the frequent need for model iteration, where model components are added and removed; the complexity of rules needed to describe the behaviour of biological systems, such that underlying assumptions may often be untestable; and the experimental difficulty of obtaining relevant measurements required for adequate parametrisation of the underlying mathematical model. Our method should aid with future modelling as then one can "rule in"/"rule out" critical determinants.

Our approach is centred on mimicking the process of *ablation* within the fields of neuroscience [18, 157, 165] and embryonic development [10]; this is where one kills or disables a single neuron to observe how the remaining system behaves. Each cell is considered a *functional unit* that changes the SF from an implied *baseline* value, to the *observed* value of the staining intensity. The *baseline* value we calculate as the SF at the cell's location *were the cell not present*; this calculation is performed by solving a steady-state diffusion equation (Poisson's equation) with decay. We calculate the signal staining intensities that we expect based on the postulate of all of the variability coming from the impact of the signalling field. We then compare the expected (*baseline*) staining intensity of each cell with the experimentally measured (*observed*) values. Differences between the *baseline* and *observed* values are interpreted as *cell impact*: how a cell alters the SF. We test applicability of our approach using histological samples of breast cancer.

The chapter is structured as follows: in Section 4.1, we present the mathematical details behind our method including assumptions made and parameter selection. Section 4.2 discusses our method applied to a multi-channel immunofluorescence *in situ* hybridisation (iFISH) stained breast cancer data set, in which the *HER2* gene and *HER2* protein expression were studied concurrently. Section 4.3 presents the approach in the context of an interacting particle system. We also give a toy problem to demonstrate our approach when one uses artificially generated data.

4.1 Method Applied To Paracrine Signalling

Our approach consists of two stages: a mathematical modelling step (Section 4.1.1), and a parameter selection step (Section 4.1.2). We first pose a class of diffusion models governed by a PDE for the description of SF in the extracellular space. This class of models has a number of free parameters: the effective diffusion constant; the rate of decay and the type of boundary condition posed on the cell surfaces. We then consider model selection by asking: what is the discrepancy between the expression of the target being analysed (the *observed* staining intensity) and the expected SF *were the cell absent from the histological slide* (the *baseline* staining intensity). Using

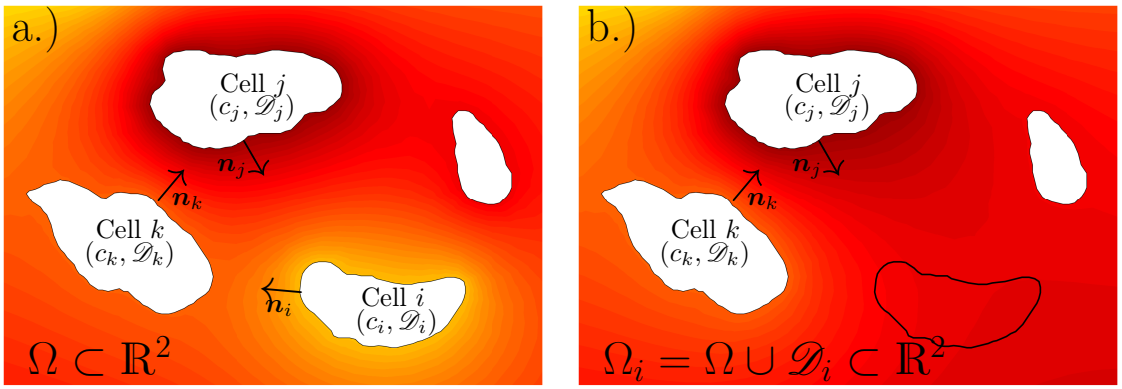

Figure 4.1: Mathematical idealisation of cells on a pathology slice. Cells are shown in white and the Signalling Field occupies the space between them at varying concentrations. (a.) Original domain Ω, and (b.) modified domain $\Omega_i = \Omega \cup \mathscr{D}_i$. See text for details.

the assumption that the SF should account for most of the variance in signal that the cell produces, we carry out model selection over the space of possible model parameterisations. Finally, we then have a *baseline* staining signal intensity and an *observed* signal intensity for each cell.

4.1.1 Mathematical Modelling

To model paracrine signalling, we assume that cells communicate via a diffusible species present in the extracellular domain called the Signalling Field (SF), with concentration profile $u = u(\boldsymbol{x})$, which degrades at rate $\lambda > 0$. Cells are stained with a probe that binds internally: the chromogenic or fluorescent intensity is not necessarily representative of the SF. However we specify that production of the SF is linearly related to the stain intensity. We do not model other signalling processes such as direct signalling or forces exerted between cells via direct contact (such as adherent or gap junctions) or indirect contact via the ECM.

A histology slide is a 2-dimensional slice though a 3-dimensional tissue. In reality, the cells visible on this slide would be interacting with cells above and below the side (before sectioning the tissue). However, for the purposes of our reconstruction we consider only cells visible in the slide, and consider the signalling field to diffuse in 2-dimensions only. Whilst the validity of this assumption has not been tested, it is frequently made use of in the literature. In principle a 3-dimensional analysis could be performed by considering multiple adjacent pathology slides.

We consider N non-overlapping cells labelled $i \in \mathcal{N} = \{1, \ldots, N\}$ that occupy volumes[1] $\mathscr{D}_i \subset \mathbb{R}^2$ (see Figure 4.1(a)), so that extracellular domain is $\Omega = \mathbb{R}^2 \backslash \bigcup_{i=1}^{N} \mathscr{D}_i$. We consider the case in which the timescale of diffusion is faster than any other timescale of interest so that the SF is in steady-state. The concentration profile u is

[1]Thus $\mathscr{D}_i \cap \mathscr{D}_j = \emptyset$ for $i \neq j$.

then governed by

$$\nabla^2 u - \alpha^2 u = 0 \text{ in } \Omega\,, \tag{4.1}$$

where $\alpha^2 = \lambda/\kappa$ and $\kappa > 0$ is the diffusion coefficient.

We suppose that the production/absorption of the SF is proportional to the difference in the average cellular stain intensity c_i (averaged over the cell) and the concentration of the SF at the cell boundary. Thus we write[2]

$$\boldsymbol{n}_i \cdot \nabla u = \gamma(c_i - u) \text{ on } \boldsymbol{x} \in \partial\mathscr{D}_i\,. \tag{4.2}$$

The parameter $\gamma \in (0, \infty)$ is a measure of how strong the cellular response is to a difference between the local SF field and the "target" value c_i. When $\gamma = 0$, the cell does not react to the signalling field at all; as $\gamma \to \infty$ the cell actively absorbs/secretes the SF as fast as it needs to in order to maintain the interior of the cell at the fixed *observed* staining intensity c_i.

The problem defined by equations (4.1)–(4.2) is well-posed[3] and would allow us to recreate the extracellular SF were parameters (α, γ) known. However, it was our aim to learn how each cell modifies the SF. To this end, for each cell $i \in \mathcal{N}$, we will determine the difference between the *observed* staining intensity (c_i) and the expected signal *were the cell not present*. Therefore, we define a new SF problem with cell i removed. Denoting the resulting concentration profile by u_i, we then have

$$\nabla^2 u_i - \alpha^2 u_i = 0 \text{ in } \Omega_i\,, \tag{4.3}$$

and $\Omega_i = \Omega \cup \mathscr{D}_i = \mathbb{R}^2 \setminus \bigcup_{j \neq i} \mathscr{D}_j$. Thus the SF now diffuses in the region occupied by cell i also; the boundary conditions on the remaining cells stay the same

$$\boldsymbol{n}_j \cdot \nabla u_i = \gamma(c_j - u_i) \text{ on } \boldsymbol{x} \in \partial\mathscr{D}_j\,, \tag{4.4}$$

for all $j = 1, \ldots, i-1, i+1, \ldots, N$. The domain for the modified problem is illustrated in Figure 4.1(b). The problem is also well posed (see Appendix E.1). The *baseline* SF were cell i not present is then defined as the mean value of the SF over the cell

$$b_i := \frac{1}{|\mathscr{D}_i|} \int_{\mathscr{D}_i} u_i(\boldsymbol{x}) \mathrm{d}\boldsymbol{x}\,. \tag{4.5}$$

We could have chosen to average over the cell boundary rather than its area, however this gives no qualitative difference in our results. We define the *cell impact* to be

$$f_i := c_i - b_i\,, \tag{4.6}$$

which can be interpreted as follows: if $f_i > 0$, the cell is secreting factors locally into the SF; and if $f_i < 0$, then the cell is absorbing factors from the SF.

We solve the PDE systems (4.3)–(4.4) using a finite element method; see Appendix E.2 for details.

[2]In principle, we could use the spatially varying stain intensity in equation (4.2) rather than averaging over the cell. Measuring and quantifying a heterogeneous protein concentration within a cell would be experimentally demanding and may require extra analysis, e.g., location of internal cell apparatus. This spatial averaging is often done automatically by WSI software.

[3]We also implicitly assume that as $\|x\| \to \infty$, there is a free boundary.

4.1.2 Parameter Selection

Parameter selection is the biggest challenge to implementation of our method. For metabolic processes, diffusion constants and decay rates are frequently known, for example, for oxygen, glucose, etc. However, in our case, the specific chemicals comprising the signalling field are unknown (we note again that this is not the chemical stained for, but a hypothesised downstream factor).

Rather than trying to estimate $\vec{p} = (\alpha, \gamma)$ from experiments, we choose $\vec{p}$ to give a best fit to the data in the following sense. For each stain, we measure the *observed* staining intensities for each cell $\vec{c} = \{c_1, \ldots, c_N\}$. For a fixed set of model parameters $\vec{p}$, the method described above can be used to generate the *baseline* intensities $\vec{b} = \{b_1(\vec{p}), \ldots, b_N(\vec{p})\}$.

The parameters $\vec{p}_*$ are then chosen such that the coefficient of determination (denoted R^2) is maximised, i.e.,

$$\vec{p}_* = \arg\max_{\vec{p}=(\alpha,\gamma)} R^2 \,, \tag{4.7}$$

where

$$R^2 = 1 - \frac{\sum_{i=1}^{N}(c_i - b_i)^2}{\sum_{i=1}^{N}(c_i - \bar{c})^2} \,, \tag{4.8}$$

with

$$\bar{c} = \frac{1}{N}\sum_{i=1}^{N} c_i \,. \tag{4.9}$$

The R^2 coefficient for a model (with fixed parameters) measures the proportion of the variance that is explainable by the model. When $R^2 \leq 0$ the model does not describe any of the observed data, and as R^2 increases ($R^2 \to 1$) the model becomes an exact fit.

Therefore in equation (4.8), the R^2 coefficient measures the fraction of the variance of the stain intensities that can be accounted for by our signalling field model. The variance in stain intensities can be accounted for by epigenetic, stochasticity, and environmental inputs. By maximising the R^2 value, we obtain an upper bound for the paracrine signalling variance contribution.

4.2 Experimental Data

We apply our approach to the analysis of breast cancer tissue sections stained with nuclear stain *DAPI* that reflects cellular DNA content, and two important proteins targets: *HER2*, a receptor tyrosine kinase that is amplified in a subset of breast cancers and is considered to be a potent "driver" gene [105], and *Oestrogen Receptor (ER)*, a nuclear receptor that mediates cellular response to oestrogen signalling[4]. Both *HER2* and *ER* staining are expected to have a profound influence on cell phenotype

[4]These were done with Immunohistochemistry (IHC) derived methods.

and overall tumour aggression. Additionally, using fluorescence *in situ* hybridization (FISH), data regarding the amplification status of the *HER2* gene are available.

The cell outlines were found using the GoIFISH software [154], the pixels that formed the cell outlines were down sampled by a factor of 8, so that the cell edges were given by polygons. For the FEM scheme, nodes within domain Ω were placed using Halton node placing[5] [43]. To simplify parameter searches in $\gamma \in (0, \infty)$ (which crosses many orders of magnitude) we mapped it to the bounded variable $\beta = \gamma/(\gamma + 1) \in (0, 1)$.

From the method in Section 4.1, we maximise R^2 given in equation (4.8) for each of the 3 stains for 3 histology slides. The corresponding values of α_* and γ_* are found in Table 4.1. From Table 4.1, we see that the $R^2_{\max}$ is small for *DAPI* as expected: DNA content should be independent of diffusible signalling components. In contrast, for the *HER2* and *ER* stains, Table 4.1 suggests that the majority of the variance in the *observable* data set can be explained by SF.

Stain	**Region**	**Sample 1,** $N = 479$			**Sample 2,** $N = 381$			**Sample 3,** $N = 524$		
		α_*	γ_*	$R^2_{\max}$	α_*	γ_*	$R^2_{\max}$	α_*	γ_*	$R^2_{\max}$
DAPI	Nucleus	0.008	0.15	17%	0.006	0.04	12%	0.006	0.05	21%
HER2	Membrane	0.000	∞	61%	0.023	∞	60%	0.010	6.75	67%
ER	Nucleus	0.012	0.14	51%	0.012	1.11	45%	0.003	0.07	50%

Table 4.1: Maximum variance reduction possible for each stain and corresponding parameters for BCA data set.

Note that the large values of γ_* indicate a strong coupling between the *HER2* staining intensity and the SF. It is reassuring that $R^2_{\max}$ and α_* are similar for the same stain across different slides. The range of values of γ_* are less consistent.

In Figure 4.2, we plot the *observed*, *baseline* and *cell impact* spatial staining patterns for the *DAPI*, *HER2* and *ER* stains for sample 1. Additionally, we also plot the solution to equation (4.1) using the $\vec{p}_*$ parameter set (without removing any cells). This allows us to visualise the hypothesised SF. Plots relating to the same stain use the same scaled colour bar. The general trend one finds is that the *observed* data set is very heterogeneous with regards to staining intensity, the *baseline* data set looks like a smoothed version of the *observed* data set, and the *cell impact* data set shows variations around the *baseline*.

4.2.1 Possible Identification of Microenvironmental Niches

For Sample 1, ignoring the *DAPI* stain, we plot the *baseline HER2* and *baseline ER* data sets as a scatter graph in Figure 4.3(a). One observes approximately 3

[5]Halton node placing is a quasi-random (deterministic) mesh generation technique that covers domains in a uniformly distributed manner without clustering of nodes. One advantage over equal spaced node points is that more nodes can be added without needing to move the locations of previously placed nodes.

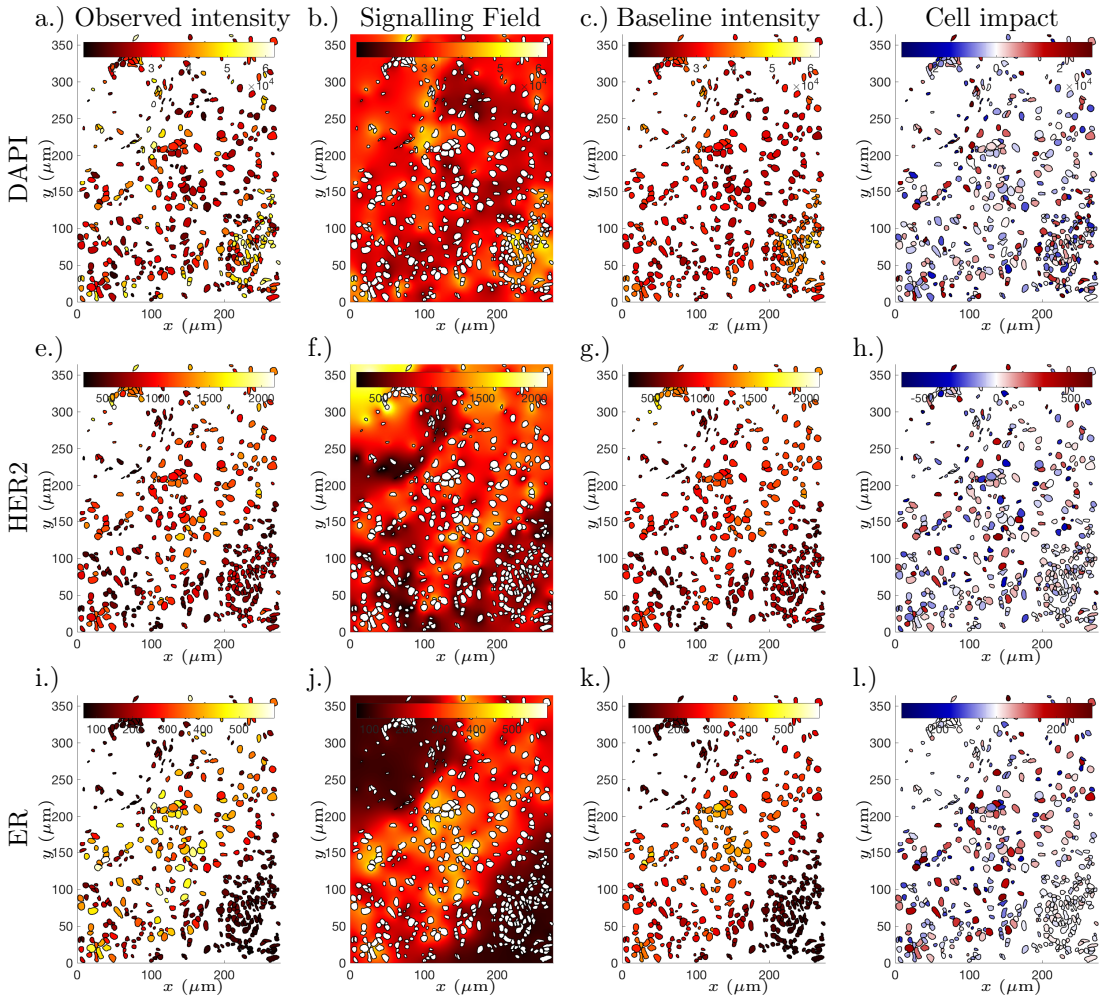

Figure 4.2: Pathology slide with outlines plotted. Figures showing stain intensity for: (left column) *observed* intensities $\vec{c}$; (left centre column) the exterior signalling field — the solution to equation (4.1); (right centre column) *baseline* intensities $\vec{b}$; (right column) *cell impact* $\vec{f}$ — for this column red colours correspond to secreting cells, blue colours correspond to absorbing cells. The rows correspond to: (top row) *DAPI* stain; (middle row) *HER2* stain; and (bottom row) *ER* stain.

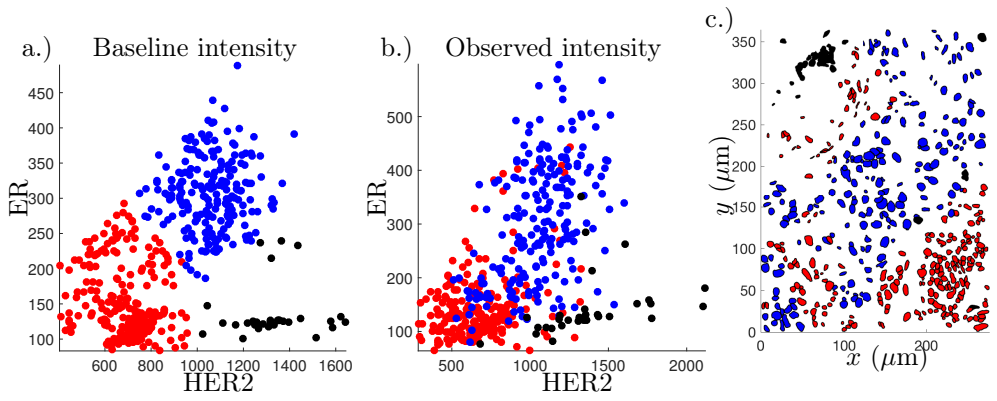

Figure 4.3: Figure to show possible existence of microenvironmental niches. a.) k-means clustering applied to *HER2* and *ER baseline* intensities; b.) The labelling from the k-means clustering shown on the *HER2* and *ER observed* data sets; and c.) the k-means clustering labels applied spatially.

clusters of points, which can be found using k-means clustering[6]. When looking at the *observed* staining intensities, these clusters of points appear as less distinct entities, see Figure 4.3(b). An interpretation of this finding is that there are 3 distinct microenvironmental niches on the slide. Viewing these clusters spatially, one can see that cells with approximately the same microenvironment are located in adjacent locations, see Figure 4.3(c). Samples 2 and 3 seemed to also have niches, but without such immediately identifiable groups.

4.2.2 Use of Centromeric Probes to Investigate *HER2* Gene Amplification Status

Using the FISH experimental procedure, a *HER2* gene specific probe was used in conjunction with a centromeric probe to identify the copy number of the *HER2* gene for each cell. The GoIFISH software package is then able to count the number of subcellular probes. We write the copy number of cell i as

$$A_i = \frac{\text{BAC}}{\text{CEP}} = \frac{\#\text{ Number of } \textit{HER2} \text{ gene probes detected}}{\#\text{ Number of centromeres detected}}\,. \tag{4.10}$$

As the data are noisy, we are conservative and discard data points that may be biologically unreasonable, i.e., correspond to an amplification ratio that is infinite ($A_i = \infty$), or less than a single specific probe detected per centromere ($A_i < 1$). Additionally, we remove a small number of cells that are not tumourous, e.g., lymphocytes, fibroblasts. We then put the data into two ordinal sets, either unamplified wild type (WT) cells where the *HER2* gene has not been upregulated ($A_i = 1$), or where the cell has amplified the *HER2* gene ($A_i > 1$). For the 3 data sets, after invalid data have been discarded, amplified *HER2* cells account for 34%, 9% and

[6]The optimal value of k for k-means clustering was confirmed using the Davies-Bouldin index, which was maximised for $k = 3$ [36].

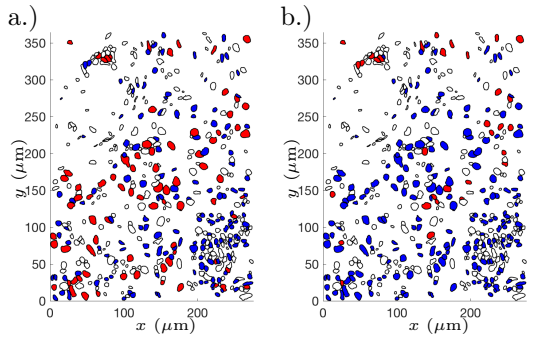

Figure 4.4: Figure to show the *HER2* status of cells. a.) Status found from GoIFISH software analysis, b.) results of logistic regression using $\vec{c}$. Colour labels are as follows: clear/white labelled cells were unidentifiable/non-tumour; blue labelled cells denote wild type; and red cells had the *HER2* gene amplified.

20% (respectively) of the cells on the slide. In Figure 4.4(a), we spatially visualise the *HER2* status of the cells in Sample 1.

For the first data set, using a logistic regression, one can use the measured *HER2* staining intensities $\vec{c}$ to predict whether the *HER2* gene is amplified $\vec{A} = \{A_1, \ldots, A_N\}$. This logistic regression is correct with 66% accuracy (see Figure 4.5), and can be seen in Figure 4.4(b). Analysing the binary classified data sets for staining intensity (either low or high staining intensity with the threshold determined by the logistic regression), we find that for high staining intensity cells tend to be net secretors of the SF ($f_i > 0$), and cells with low staining intensity tend to be net absorbers of the SF ($f_i < 0$).

However, when looking at cells with low *HER2* staining intensity, but with amplified *HER2* gene, we find that the *cell impact* for the *HER2* stain is greater than the mean for all low *HER2* stain intensity cells (see Figure 4.5). By use of z-tests (used for $n > 30$ samples), we reject the null hypothesis that: *the mean* cell impact *for cells with low* HER2 *stain intensity and amplified* HER2 *gene is the same as the population mean* cell impact *for all cells with low* HER2 *stain intensity*; compared to the alternative hypothesis that the means are not the same. This is found to be statistically significant with $p < 0.05$. The interpretation of this is that when cells have a low staining intensity, but with an amplified *HER2* gene, the cells may not necessarily stain brightly but are net secretors into the SF (and therefore they likely stain *comparatively* more intensely than their immediate neighbours).

Additionally, it should be noted for cells with low staining intensity: for amplified *HER2* copy number, cells are net producers of the SF impacting *ER* intensity; and for unamplified *HER2* cells, cells are net absorbers of the SF impacting *ER* intensity (for both cases using z-tests, $p < 0.05$).

4.3 Method Motivation via Toy System

In this section we evaluate the efficacy of our method on synthetic data (where we know the exact mathematical representation of the heterogeneity). We generate this data with the following simple model. For each cell i, we suppose that there is measurable quantity $y_i = y_i(t)$ corresponding to the staining intensity. We suppose that there are a number of cell phenotypes, labelled by τ in set $\mathcal{T}$. We suppose that each cell produces a signalling field from other cells as well as to some internal

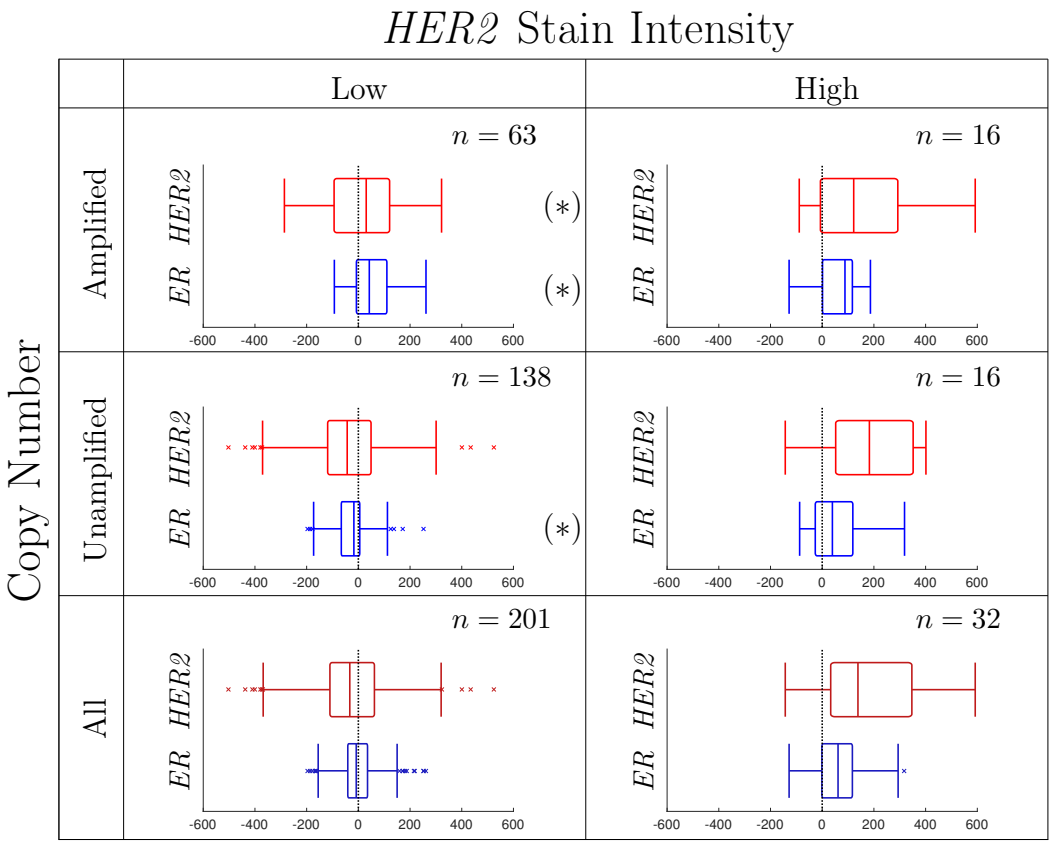

Figure 4.5: Tukey box plots for *cell impact* data sets $\vec{f}$ for *HER2* (red) and *ER* (blue) separated by low/high *HER2* staining intensity ($\vec{c}$) and unamplified/amplified *HER2* gene expression ($\vec{A}$). The concatenated data sets are shown on the bottom row. Asterisks denote statistically significant differences between the data set denoted and the mean low/high *HER2*/*ER* cell action (mean of the box plot shown in the bottom row). The black dotted line corresponds to $f = 0$.

dynamical system within the cell. Thus we write

$$\frac{\mathrm{d}y_i}{\mathrm{d}t} = \mu_i(y_i) + \phi_i(y_i, u)\,. \tag{4.11}$$

Here μ_i represents the internal dynamics, and will account for the cell's phenotype τ, and ϕ_i represents the forcing by the signalling field u. As before we suppose that the dynamics of y_i are slower than the diffusion of the SF, so that u is in quasi-steady-state. In the method described in Section 4.1, this had the form

$$\phi_i(y_i(t), u(\boldsymbol{x})) = \frac{\beta}{|\mathscr{D}_i|}\int_{\partial\mathscr{D}_i} (u(\boldsymbol{x}) - y_i(t))\,\mathrm{d}S\,, \tag{4.12}$$

where β is a scaling constant with units length over time, and $u = u(\boldsymbol{x})$ obeys equations (4.1)–(4.2). One interpretation of equations (4.11)–(4.12) is that of a "swarming" model, where particles have internal dynamics μ_i, and ϕ_i is a term analogous to an interaction potential.

The *baseline* was then found by considering the average concentration at the cell's location were the cell not there. In Section 4.1 cells had geometries and so required changes to the domain.

For simplicity, in our synthetic system, we will consider cells occupying negligible area, i.e, they will behave as point sources/sinks of the SF — and therefore we do not need to incorporate boundary conditions. In this case, the *baseline* (b_i) can be calculated by removing the internal dynamics for cell i, i.e., by setting $\mu_i = 0$. We do not try to systematically reduce the model of Section 4.1 to a model with point sources (by supposing cells are well separated, for example). Rather we postulate a new simpler model in which the interaction between cells depends on their separation though the Green's function for equation (4.1). Specifically, we take ϕ_i to be

$$\phi_i = \beta\sum_{j\neq i} G_n(d_{ij}, \alpha)\,[y_j(t) - y_i(t)]\ , \tag{4.13}$$

where G_n satisfies

$$\nabla^2 G_n - \alpha^2 G_n = -\delta(\boldsymbol{x}) \text{ in } \mathbb{R}^n\,, \tag{4.14}$$

and d_{ij} represents the distance between cells i and j. The form of G_n depends on the dimension, and is given by

$$G_n(r,\alpha) = \begin{cases} K_0(\alpha r)/2\pi & \text{if} \quad n = 2\,, \\ e^{-\alpha r}/4\pi r & \text{if} \quad n = 3\,, \end{cases} \tag{4.15}$$

where K_0 is the modified Bessel function of the second kind. The *baseline* is then given by

$$b_i = \sum_{j\neq i} c_j\, G_n(d_{ij}, \alpha) \Big/ \sum_{j\neq i} G_n(d_{ij}, \alpha)\,. \tag{4.16}$$

Notice that as cells are points, there is no γ parameter (though in some sense it has been replaced by β).

We specify that there are three cell phenotypes $\tau \in \mathcal{T} = \{1, 2, 3\}$. We take $N = 3000$. 1500 cells are placed uniformly at random in the unit circle; 1500 cells are placed uniformly at random in the annulus between $r = 1$ and $r = 2$ (see Figure 4.6). Using k-means clustering, cells are assigned into 15 groups. Groups are then assigned a cell type label randomly so that there are 5 groups of each cell type. The internal dynamics of each cell type are chosen to be given by

$$\mu_i(y_i) = \begin{cases} \epsilon_i/4 - y_i & \text{if} \quad \tau_i = 1\,, \\ 0 & \text{if} \quad \tau_i = 2\,, \\ 1 + \epsilon_i/4 - y_i & \text{if} \quad \tau_i = 3\,, \end{cases} \tag{4.17}$$

and we use the 3-dimensional Green's function as the interaction term. Here ϵ_i is a random number drawn from $\epsilon_i \sim \mathcal{N}(0, 1)$ and is the means by which we model heterogeneity within a fixed cell phenotype. We choose $\beta = 4\pi/N$ and $\alpha = 10$. We can interpret the cell phenotypes as: cell phenotype $\tau = 1$ is a cell that averages the signal received by neighbours to settle at a steady-state close to some intrinsic value $\epsilon_i/4$; cell phenotype $\tau = 2$ is a passive cell that mimics nearby cells; and cell phenotype $\tau = 3$ is a cell that averages the signal received by neighbours to settle at a steady-state close to some intrinsic value $1 + \epsilon_i/4$. From random initial conditions in the unit interval ($y_i(t = 0) \in [0, 1]$), the system will reach a steady-state. The functional forms chosen are such that there is considerable overlap in the distribution of steady-states for each cell phenotype, so that it is not immediately clear which phenotype a cell belongs to given the steady-state value c_i.

In Figures 4.6(a, b), we see a spatial plot of the cell centres and a histogram of the *observed* intensities ($\vec{c}$); Figure 4.6(c, d) reveals the discrete cell phenotypes that are not immediately apparent when viewing Figures 4.6(a, b). To calculate the *baseline* ($\vec{b}$), we assume the functional form of the interactions are as in equation (4.13), but without specifying the value of α, which is determined via a best fit as in Section 4.1.2. In Figure 4.6(e, f), we show a spatial plot and histogram of the *baseline* cell intensities; and in Figure 4.6(g, h) we show the *cell impact* cell intensities. From Figure 4.6(c) to Figure 4.6(f), we see the emergence of a trimodal distribution indicating the three cell phenotypes. The phenotype $\tau = 2$ is easily identified in Figure 4.6(h) as the population having zero *cell impact*: this is to be expected since these cells essentially copy what their neighbours are doing.

Over 1000 simulations, we find that α_* has a mean value of 11.49 [95% CI: (8.65, 14.46)], and $R^2_{\max}$ has a mean value of 79.6% [95% CI: (76.9%, 82.3%)]. Carrying out k-means clustering on $\vec{c}$, $\vec{b}$ and $\vec{f}$ using *a priori* knowledge that there are 3 phenotypes present, one finds that on average one identifies the 3 groups with 70.2% [using $\vec{c}$, 95% CI: (49.9%, 82.5%)], 74.3% [using $\vec{b}$, 95% CI: (57.4%, 87.3%)], and 15.7% [using $\vec{f}$, 95% CI: (11.0%, 20.1%)] accuracy respectively. Therefore, one can obtain slightly higher accuracy by looking at the *baseline* intensities rather than the stain intensities. Moreover, if we identify the passive $\tau = 2$ cells using $f_i \approx 0$, see Figure 4.6(h), then the remaining cells can be clustered into 2 groups with approximately 100% accuracy.

Carrying out further simulations using different strengths of interactions, we find that as we increase β, the value of $R^2_{\max}$ increases as well as the value of α_*. This first

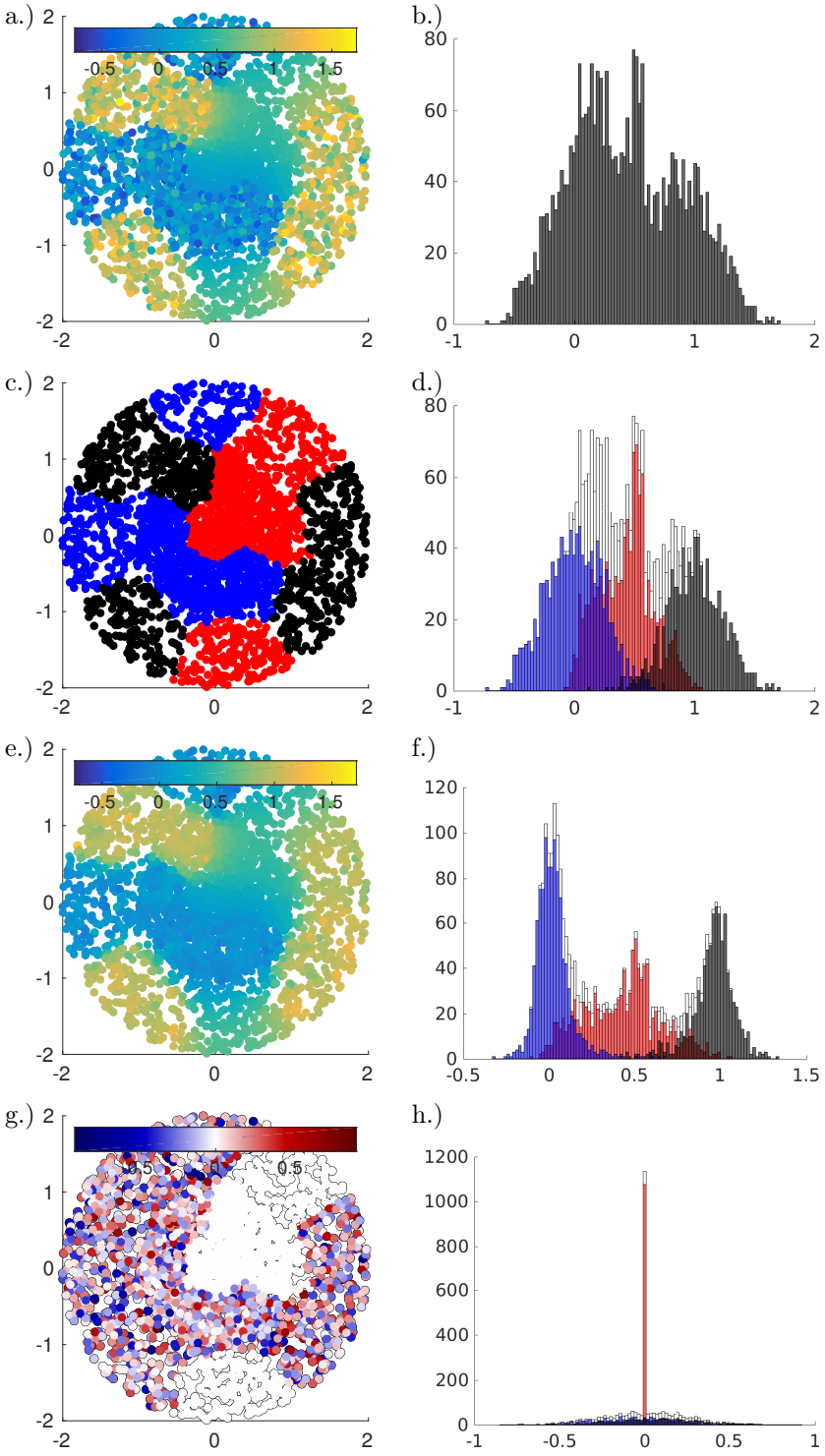

Figure 4.6: Plots relating to toy model. (a, b.) Plot of *observed* cell intensities, and corresponding histogram of intensities. (c, d.) Plot of simulated cell locations, now marked red or blue according to cell phenotype, and histogram now broken up by cell phenotype. (e, f.) Plot and histogram of *baseline* cell intensities. (g, h.) Plot and histogram of *cell impact* intensities. For the simulation shown, $\alpha_* = 10.91$, $R^2_{\text{max}} = 79\%$. Using k-means clustering on the 3 data sets ($\vec{c}$, $\vec{b}$, $\vec{f}$), cell phenotypes are correctly identified with: 79% ($\vec{c}$), 84% ($\vec{b}$), and 13% ($\vec{f}$) accuracy.

result should be expected as $R^2_{\max}$ is the maximum proportion of variance accounted for by paracrine signalling. The second result is an artefact of the toy system, the *baseline* is a weighted average given by equation (4.16), α_* will then increase as the fitting procedure will prioritise local interactions as the interaction strength increases. It should be said however that α_* is always within the correct order of magnitude of α, even as β changes drastically. When considering the 2-dimensional Green's function, the same trends persist.

4.3.1 Final Remarks: Method Applicability

When applied to our synthetic data, the method successfully deconvolutes the *observed* intensities data set into the *baseline* and *cell impact* intensities. This allows for easy visual interpretation and further analysis.

In our analyses of clinical samples, we used stains for proteins where we are unsure of the exact sources behind variation in stain intensity, be that genetic, microenvironmental, or stochastic. *HER2* amplification is widely believed to be a genetic event and should be heritable. Expression levels of *HER2* protein are expected to reflect the gene amplification status. On the other hand, some experimental evidence shows *HER2* expression might reflect not only genetic material, but also microenvironmental stimuli, such as Notch and NF-κB (RANK) signalling (with the effect of increased *HER2* transcription and regulation of the expansion of cancer stem cells) [73, 82, 96, 168]. The interpretation of the $R^2_{\max}$ values should be as *what is the maximum percent of the signal variance explainable via our model of cellular communication for paracrine signalling.* Therefore, our method can potentially reveal paracrine interaction even in scenarios where variability of the analysed trait is primarily believed to reflect genetic differences.

When considering the data set used in Sections 4.2, for our method to "pick out" important features of the data, we recommend that $R^2_{\max} \gtrsim 40\%$ at a minimum.

Chapter 5

Discussion and Conclusion

5.1 Evolving Spatial Networks

In Chapter 2, we introduced a model for evolving spatial networks, and we used a mean-field approximation to reduce the dimension of its governing hierarchal Fokker–Planck equations. Specifically, by defining a local state degree distribution, we derived IPDEs (2.16) and (2.26) to describe an evolving spatial network that includes evolution of the position of nodes (or some more general state vector), edge creation, edge deletion, and new node creation that occur at prescribed rates. Our approach generalises commonly-studied master-equation approaches by including a state space so that we can examine spatial networks.

For all our examples in Chapter 2, the motion in state space was independent of network structure. Of course, it is also possible to imagine scenarios in which the motion depends on the network. Our mean-field approach can be readily extended to situations in which the motion of a node depends on its degree (and even the degrees of its neighbours). For example, in the case of pairwise interactions it is easy to extend the model to the case in which the interaction depends on the degrees of the two nodes as well as their position. However, network information that is not expressible in terms of the degrees of nodes, such as the local clustering coefficient, would require extra closure assumptions to incorporate. In Chapter 3, osteoblasts of degree $k = 0$ were able to diffuse — we did not carry out a derivation of this diffusion term as it was a trivial extension of the derivation in Chapter 2.

5.1.1 Mean-Field Approach Extensions

In our model of network evolution nodes are created or removed according to Poisson processes, so that the model may generate multiedges. Our approach may be extended to simple graphs, in which multiedges are not allowed, with an additional closure assumption. In the edge creation term the creation of an edge should be abandoned if an edge already exists between a pair of nodes. This results in $\mathcal{C}(\boldsymbol{s}_i, k_i, \boldsymbol{s}_j, k_j)$ being multiplied by the probability that there is no existing edge between nodes i and j, which can be approximated by $1 - k_i k_j / 2m$, where k_i and k_j are the node degrees and m is the total number of edges, as in Section 2.5.

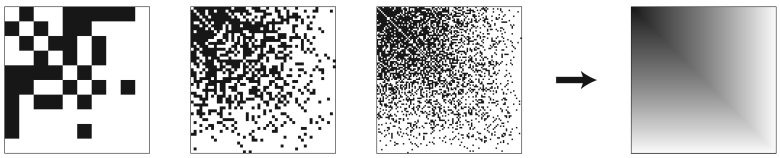

Figure 5.1: Graphic illustrating the process of a series of adjacencies (generated by realisations of random graphs) converging a Graphon limit as $n \to \infty$, which in this case is $G(x, y) = 1 - \max(x, y)$. (Figure kindly taken with permission from D. Glasscock [52].)

Another extension of interest are non-local limits of our network formation model, specifically Graphon limits [52], see Figure 5.1. A Graphon is a function from the unit square to the unit interval, $G : [0, 1]^2 \to [0, 1]$, specifying the probability of an edge after two nodes are given values in the range $[0, 1]$ drawn uniformly at random from the unit square. Deriving a differential equation for an evolving network with a Graphon as a solution is attractive because Graphons contain more information about the underlying network than the degree distribution. A literature search suggests that Graphon differential equations for evolving networks have not been derived before.

5.2 Osteocyte Network Formation

In Chapter 3, we have presented a model for the formation of an osteocyte network and identified parameters for healthy bone formation. By perturbing parameters, one can investigate irregular bone formation and the resulting osteocyte morphology changes. One can also then predict the driving differentiation markers that osteoblasts exhibit that would lead to these morphological changes. In the context of zoledronate therapy for breast cancer, we have used our model to propose reasons behind the brittle treated bone. For future experiments, we have suggested how measurable quantities link to underlying mechanisms.

From a modelling perspective, were one to chase biological reality, one could suggest many improvements to the model to improve our idealisation of the osteocyte network. Additionally, one might also want to consider the inclusion of chemical species representing proteins of interest, and the inclusion of osteoclasts to incorporate bone resorption. However, our model acts as a first step towards mathematically modelling osteocyte network formation, and avoids making overly specific assumptions on underlying mechanisms.

We now comment on how various aspects of our model compare to biological reality.

5.2.1 Triggering Osteoblast Differentiation

During a bone remodelling event, the total number of osteoblasts generated is far larger than the total number of new osteocytes generated [117]. Pazzaglia *et. al.* [119] have estimated that only 1 in 67 osteoblasts become embedded in bone matrix as osteocytes, whereas in our model, all osteoblasts will eventually differentiate; the mechanisms behind which are still poorly understood. They may involve physical

processes such as burial by neighbouring osteoblasts, or self-burial [44]. It has also been suggested that subpopulations of osteoblasts are predestinated to become osteocytes [100], and that this selection may be determined by the number of connections with osteocytes [76].

One aspect ignored in our model is mechanotransduction. It is known that mechanical loads and fluid flow sheer stress can lead to greater dendrite growth [24, 167]. After now posing our model, a pertinent question then remains as to the relative effect sizes between mechanical stimuli and microenvironmental signalling. In our work, we focused on breast cancer that metastasises to bone. One advantage to investigating breast cancer is that it is osteolytic, which means that there is a net bone reduction, so it is unlikely there is a substantial increase in pressure on bone. Other cancers may be osteoblastic, which means there would be net increase in bone mass, e.g., metastatic prostate cancer. For osteoblastic cancers, it may be hard to decouple mechanical and microenvironmental effects experimentally.

5.2.2 Osteocyte Degree Distribution

In the steady-state travelling wave regime, one can show that the degree distribution of the osteocyte network is geometrically distributed when using either the null model (see Section 3.4.1.1), or the switch-like proposed mechanism (see Section 3.4.1.3). This effect comes from the difference equation structure in equations (3.11)–(3.12) in Section 3.2.1.

In Ref. [78] a three-dimensional osteocyte network was studied, the topology of this network includes dendrites that do not connect to a second osteocyte, and edges that link between multiple osteocytes. Additionally, the nodes of their network included both osteocytes and the branching points of dendrites. Thus the communication network we studied, and the exact biological network they studied are different. However, the degree distribution of their three-dimensional scanned network was shown to be geometrically[1] distributed. It remains to be elucidated as to whether there is a reasonable explanation for this match in degree distributions, or as to whether this is coincidence.

5.2.3 Orientation of Dendrites

It is clear from Figure 3.7 that we observe orientation of edges from older osteocytes towards the younger osteocytes and the osteoblast layer. An interesting question is as to whether one can configure our model to lose this orientation.

This is also evidence of lateral connections between osteocytes [115], and we do notice some of this within Figure 3.7. Having said this, the majority of the network structure is perpendicular to the bone surface.

A possible future direction in our work may be to modify our model to explore the functional difference between lateral connections, and connections perpendicular to

[1]They actually stated that the degree distribution was exponentially distributed, but this would only be correct for continuous distributions. A geometric distribution is the discrete equivalent.

the bone surface. As osteocytes have coordinated burial, one may be able to explore whether coordinated burial can occur as a function of lateral connections, burying a group of osteoblasts simultaneously.

5.2.4 Network Description Incorrect

Our network description refers to which osteoblasts and osteocytes are communicating with each other — not the full biological reality of the dendritic network. Were one to consider the full morphology of the dendritic network, one would have to also consider edges that occasionally do not go anywhere, and edges that connect multiple nodes (hypergraphs). This would account for the branching dendrites that one sees experimentally. We also have redundancy in our communication network in the form of multiedges (multiple edges between two nodes). However in the limit of large networks, the probability of a multiedge occurring approaches zero. Additionally, even in the case of finite networks, this is very unlikely to occur as $\langle \tilde{k} \rangle_{\mathrm{Ob}}, \langle \tilde{k} \rangle_{\mathrm{Ocy}} = \mathcal{O}(1)$.

To summarise, points of dendrite branching may act as nodes within osteocyte networks and we do not account for this. The network modelled is the network of cell–cell connections, not the dendritic nor the canalicular network, and so represent the ability for communication not morphological reality. Other approaches to modelling spatial networks may be possible, although our approach allows for visualisation of the network, and is amenable to parameterisation via mathematical analysis.

5.3 Histology Analysis

In Chapter 4, we have presented a method to identify and extract diffusible microenvironment signalling from histology slides. We are also able to quantify what percentage of the data is explainable by diffusion mediated signalling. We applied our method to breast cancer histology slides and found that *HER2* amplified cells with low *HER2* stain intensity have a higher *cell impact* than the population of all low *HER2* stain intensity cells. Finally the method was evaluated on synthetic data generated by a simpler model for cell behaviour.

Due to this work being only a preliminary study, the presented analysis should be viewed as a promising first step and demonstration of the method, rather than bona fide proof of principle. We envision that the method presented here will be directly applicable to defined scenarios of biological and clinical importance. For example, paracrine signalling is responsible for microenvironment-directed therapy resistance against most of the targeted anti-cancer therapies used in clinics [160]. Yet, the signalling fields, as well as the impact of individual cells on them, have not been studied due to the lack of appropriate tools.

A clear next step to promote use and acceptance of our method would be to see how our method performs against different types of cancer stained under the same protocol. Particularly, it may be of particular interest to investigate cancers that are known to be genetically homogeneous, and so the majority of the variance in observation may come from diffusion. In contrast, one could investigate genetically

heterogeneous cancers and therefore proportionally less variance may be accountable by diffusion. Additionally, it would be particularly pertinent to design experiments where stains relating to metabolic activity were selected. Cell types are usually identifiable by eye, and our approach may even aid hypothesis of cell function.

Future experiments have been proposed to apply the method to interrogate the spatial distribution of *c-MET* phosphorylation in non-small cell lung cancers[2]. The *c-MET* protein is implied in resistance to *ALK* tyrosine kinase receptor [160, 166]. Phosphorylation of *c-MET* should be reflective of microenvironmental gradients of its ligand *HGF*, which is primarily produced by cancer-associated fibroblasts.

5.3.1 Data Limitations

Clearly our method as it stands suffers many drawbacks. Regarding use of data, we are stuck working in two dimensions. Working in three dimensions using complete reconstructions of cell geometry would be possible; however, this would be expensive and not repeatable in a clinical setting.

There will also be edge effect artefacts that we have not accounted for in the model. By this, we mean there will be cells that impact the SF, but were excluded by the biopsy extraction and preparation process. One option is to decrease sample sizes by ignoring a layer of cells at the edge of the histology slice.

5.3.2 Parameter Selection

It is likely that other methods for parameter selection are also worthy of exploration. For example, one could also make the opposite assumption: that the contribution of genetic heterogeneity is large, and the microenvironment minimally contributes to the *observed* data set $\vec{c}$ — however this does not work practically as then one could then either set $\alpha \to \infty$, or $\gamma = 0$ and then $b_i = 0$ and $\|\vec{c} - \vec{b}\|$ is maximised. Constraints have to be introduced in an intelligent manner.

Our model could also be expanded to include different classes of objects, for instance, it would not be difficult to include blood vessel structures. Additionally, were it the case that a cell was stained multiple times and one had an *a priori* knowledge for how a cell was supposed to function, relevant constraints could be included in the parameter selection method. In this work, we did not carry out an exhaustive search on parameter selection techniques.

5.3.3 Applications within Interacting Particle Systems

The approach described in Section 4.3 essentially amounted to setting up a null model for interacting particle systems allowing to ask: *assuming business as usual, how close could the null model get to reality?* This initial study suggests a methodology that

[2]The *MET* gene encodes the *c-MET* receptor protein that processes activity of the enzyme tyrosine kinase.

could be applied to more general problems. For example with regards to interacting cellular systems, mechanotransduction is another important method of cellular communication [70], to which our simulated ablation approach could be applied.

The approach may also be applicable to other interacting particle systems where the agents are not close to steady-state. For instance, we are now starting to reconcile swarming models with real data [121]. However, some swarms consist of agents carrying out different behavioural roles, e.g., leader and follower behaviour seen in pigeons [123]. If one could adapt the method appropriately, it may be possible to analyse trajectories to discern between different animal behaviours.

Appendix A

Image Processing Technique for Osteocyte Density Estimation

Using the inbuilt functions of the MATLAB image processing toolbox, our technique for calculating approximate osteocyte densities consists of three stages:

1. Colour-based segmentation to isolate the mineralised section of the bone.
2. Entropy-based segmentation to isolate and locate osteocytes centres.
3. Estimation of osteocyte density as

$$\text{Implied osteocyte density} = \frac{\#\text{osteocytes}}{\text{mineralised area}} \tag{A.1}$$

Colour-based segmentation is carried out by treating the RGB signal as a vector and clustering these vectors using k-means clustering, the value of k chosen depending on an *ad-hoc* basis depending on the specific image. Entropy-based segmentation and thresholding was used to detect approximate locations of osteocytes. Manual validation was also carried out to confirm/correct the locations of the osteocytes detected. In Figure A.1, we see the output of the algorithm, the stroma appears red, the mineralised region of the bone appears blue. The region between measured is outlined in green and the osteocyte's centre is marked with a red circle.

Our criterion for what was marked and counted as an osteocyte was as follows:

i.) The cell boundary of the osteocyte must be visible.

ii.) There must be de-calcified osteoid around the osteocyte.

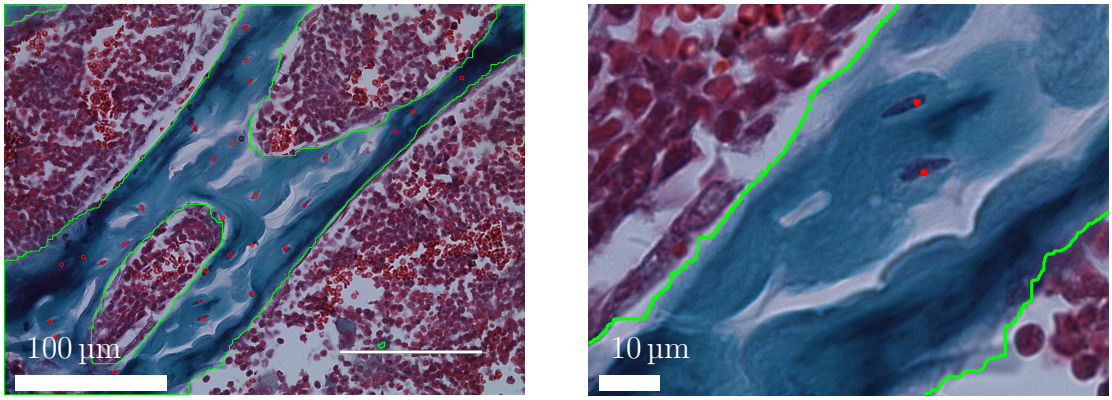

Figure A.1: Output of image processing technique for osteocyte density calculation: (left) full size image, (right) close-up image. Region measured is outlined in green and osteocyte centres are marked in red.

Appendix B

Method of lines for IPDE in Section 2.6.2

We briefly describe the numerical method used to solve equation (2.31). A finite-volume method (FVM) involves averaging equation (2.31) over a test volume. We derive a numerical scheme for the quantities

$$U_{k,j}(t) := \frac{1}{\Delta x}\int_{(j-1)\Delta x}^{j\Delta x} u_k(t,x)\mathrm{d}x\,, \tag{B.1}$$

for $j = 1,\ldots,J$ and $\Delta x = 1/J$ and large $J \in \mathbb{N}_0$. For the degree k flux defined as

$$F_k(t,x) = \mu u_k(t,x) - \frac{\sigma^2}{2}\frac{\partial u_k}{\partial x}(t,x)\,, \tag{B.2}$$

using the Fundamental Theorem of Calculus (or Divergence theorem in higher dimensions), we need to approximate the flux at the edges of the test volume

$$\frac{1}{\Delta x}\int_{(j-1)\Delta x}^{j\Delta x}\frac{\partial}{\partial x}F_k(t,x)\mathrm{d}x = \frac{1}{\Delta x}\left[F_k(t,j\Delta x) - F_k(t,(j-1)\Delta x)\right]\,. \tag{B.3}$$

Using central differences, one can write

$$F_k(t,j\Delta x) = \begin{cases} \frac{\mu}{2}\left(U_{k,j}+U_{k,j+1}\right) - \frac{\sigma^2}{2\Delta x}\left(U_{k,j+1}-U_{k,j}\right) & \text{if} \quad j \neq 1, J\,, \\ 0 & \text{if} \quad j = 1, J\,, \end{cases} \tag{B.4}$$

and the no flux boundary conditions are immediately incorporated at the end points. The discretisation of the drift and diffusion differential operators is second order, in that

$$|U_{k,j}(t) - u_k(t,x)| = \mathcal{O}(\Delta x^3)\,. \tag{B.5}$$

The summation and integration terms can then easily be approximated using the trapezium rule; for general $f = f(k,x)$, we write

$$\sum_{k=0}^{\infty}\int_0^1 f(k,x)u_k(t,x)\mathrm{d}x \approx \frac{1}{2}\sum_{k=0}^{\infty}\sum_{j=1}^{J}\left[f(k,(j-1)\Delta x) + f(k,j\Delta x)\right]U_{k,j}(t)\,. \tag{B.6}$$

Putting all these terms together, one has a system of ODEs (this discretisation of space is known as the *method of lines*). One then solves the resulting equations with a Runge–Kutta scheme (or other method for initial value problem ODEs).

Appendix C

Monte Carlo Algorithm for Stochastic Simulation of Bone Formation

We give pseudocode for a fixed time step Monte Carlo algorithm for our osteocyte network formation model described in Section 3.1 using functions and parameters as detailed in Table 3.2. The Monte Carlo algorithm is broken town into two sub-algorithms. Algorithm 2 is the master algorithm that calls on Algorithms 3 and 4.

Algorithm 3 details how the network structure changes with the following Poisson processes: edge creation events from osteocyte to osteoblast; osteoblast to osteocyte differentiation; and osteoblast proliferation. Algorithm 3 follows from the Algorithm 1 given in Chapter 2. When the number of osteoblasts is fixed [see equation (3.34)], one can save on computation time by enforcing that osteoblast differentiation and proliferation occur simultaneously, i.e., a proliferation event is triggered by a differentiation event.

Algorithm 4 details the changing domain $\Omega(t)$ and boundary $B(t)$ (we specify osteoblast migration as part of this). For the changing domain, one has a few options regarding how one deals with the boundary (e.g., the level set method), but due to the fact that we have osteoblasts that occupy positions on the boundary, we use a particle method (discretising the boundary with an ordered set of particles).

As osteoblasts can diffuse on the boundary $B(t)$, osteoblast diffusion is incorporated into this Algorithm 4 via a position jump process (a type of random walk) where osteoblasts can jump either left or right along the discretised boundary as a Poisson process that approximates diffusion (Brownian motion) as the spacing between the boundary discretisation reduces to zero. Therefore, osteoblasts move perpendicular to $B(t)$, and secrete bone normal to $\Omega(t)$.

For all simulations in Chapter 3, in Algorithms 2, 3 and 4, we use a global time step of $\Delta t = 0.25\,\text{days}$ and a diffusion time step of $\delta t = 0.0125\,\text{days}$. Osteoblasts are placed uniformly at random along the boundary B. The initial spacing between discretisation points along boundary B is set as $0.01\,\text{mm}$ with tolerances in Algorithm 4 chosen as $\text{TOL}_1 = 0.006\,\text{mm}$ and $\text{TOL}_2 = 0.0015\,\text{mm}$. Therefore, lots of new discretisation points will be added initially as the boundary deforms.

We now give extra details for Algorithm 4 on the particle method for the changing

boundary and the selection of the jumping rate for the osteoblasts.

Algorithm 2: Master algorithm for fixed time step progression of $\Delta t > 0$ that refers to Algorithms 3 and 4.

Data: Choose an end time $T_{\text{end}} = M\Delta t$ for large $M \in \mathbb{N}$ and small $\Delta t > 0$. For Algorithm 4, one needs to also specify osteoblast diffusion time step $\delta t > 0$ and two tolerances $\text{TOL}_1 > \text{TOL}_2$.

Set the number of particles $N \leftarrow N_0$.

Initialise the starting state as $\boldsymbol{s}_i \leftarrow \boldsymbol{s}_0^{(i)} = (\boldsymbol{x}_0^{(i)}, \rho_0^{(i)})$ for $i = 1, \ldots, N$ and $\rho_0 \in \{\text{Ob}, \text{Ocy}\}$, and specify starting degree $k_i \leftarrow k_0^{(i)}$.

Specify region $\Omega \leftarrow \Omega_0$ and boundary $B \leftarrow B_0$. (Note that a method for the discretisation of the boundary will be needed.)

Set time counter $m \leftarrow 0$.

while $m \leq M$ **do**

- *% Network structure update.*
- Run Algorithm 3.
- *% Domain size update.*
- Run Algorithm 4.
- *% Time update.*
- Update time: $m \leftarrow m + 1$.

C.1 Extra Details for Algorithm 4

Algorithm 4 deals with the changing boundary by allowing for the addition and removal of extra discretisation points. When pairs of discretisation points are too close, one of the points may be removed to avoid having to reduce the time-step Δt. When pairs of discretisation points move to far apart, a new discretisation point is added with coordinates equal to the mean of the pair of discretisation points in question.

There is the potential for topology changes where osteoblasts would be buried without differentiation. However, we do not account for topology changes as circular regions with an osteocyte within them would shrink to a point; we save on computation time by shrinking closed to loops to points immediately (see Figure C.1).

Algorithm 4 approximates osteoblast diffusion via a jumping process along the boundary discretisation. The effective jump rates are found from analysing the Taylor expansion for the Poisson process where one either jumps "up" a distance of ℓ_u at rate j_u or "down" a distance of ℓ_d at rate j_d along an arc length coordinate s. As an approximation, we assume that the migration speed of osteoblasts occurs at an order of magnitude faster than the rate of osteoid deposition; therefore we can assume the interface is temporarily static. Consider a small time step of size $\delta t > 0$, and denote

Algorithm 3: Algorithm for network structure changes. By `randperm`(X), we mean a permutation of the discrete set X selected uniformly at random.

% Edge creation update.
for $i \leftarrow$ `randperm`$(\{1, 2, \ldots, N\})$ *and* $\varrho_i = Ocy$ **do**
  for $j \leftarrow$ `randperm`$(\{i+1, \ldots, N\})$ *and* $\varrho_j = Ob$ **do**
    Draw a uniform random number r_1 from distribution $R \sim \mathcal{U}(0, 1)$.
    if $r_1 \leq \mathcal{C}(\boldsymbol{x}_i, \boldsymbol{x}_j)\Delta t$ **then**
      Create an edge between osteocyte i and osteoblast j.

% Differentiation update.
for $i \leftarrow$ `randperm`$(\{1, 2, \ldots, N\})$ *and* $\varrho_i = Ob$ **do**
  Draw a uniform random number r_2 from distribution $R \sim \mathcal{U}(0, 1)$.
  if $r_2 \leq D_k \Delta t$ **then**
    Osteoblast i differentiates into an osteocyte.

% Proliferation update.
for $i \leftarrow$ `randperm`$(\{1, 2, \ldots, N\})$, $\varrho_i = Ob$ *and* $k_i = 0$ **do**
  Draw a uniform random number r_3 from distribution $R \sim \mathcal{U}(0, 1)$.
  if $r_3 \leq \mu(m\Delta t)\Delta t$ **then**
    Osteoblast i produces a daughter osteoblast. The daughter osteoblast will have index $N + 1$.
    Initialise position $\boldsymbol{x}_{N+1} \leftarrow \boldsymbol{x}_i$.
    Initialise degree $k_{N+1} \leftarrow 0$.
    Update number of particles: $N \leftarrow N + 1$.

the density of osteoblasts on B by $\rho(t, s)$, then

$$\begin{aligned}\rho(t + \delta t, s) = \rho(t, s) + \delta t(j_d \rho(t, s + \ell_d) + j_u \rho(t, s - \ell_u)) \\ - \delta t(j_d + j_u)\rho(t, s) + \mathcal{O}(\delta t^2)\,.\end{aligned} \tag{C.1}$$

Taylor expanding around the value s, and taking the limit as $\delta t \to 0$, we obtain the drift-diffusion equation

$$\frac{\partial \rho}{\partial t} = (j_d \ell_d - j_u \ell_u)\frac{\partial \rho}{\partial s} + \frac{j_d \ell_d^2 + j_u \ell_u^2}{2}\frac{\partial^2 \rho}{\partial s^2} + \mathcal{O}(\ell_d^3, \ell_u^3)\,. \tag{C.2}$$

To prevent artificial drift of osteoblasts along the bone surface, one must choose $j_d \ell_d = j_u \ell_u$ and we specify that the diffusion constant is $\kappa_{\text{diff}} = j_d \ell_d^2 + j_u \ell_u^2/2$. Therefore we select the jumping rates j_u and j_d as

$$j_u = \frac{2\kappa_{\text{diff}}}{\ell_u(\ell_d + \ell_u)}\,, \text{ and } j_d = \frac{2\kappa_{\text{diff}}}{\ell_d(\ell_d + \ell_u)}\,. \tag{C.3}$$

Note that osteoblasts jump along the boundary $B(t)$ at a rate faster than all the other processes, so we specify a smaller time step $\delta t > 0$ for the osteoblast position

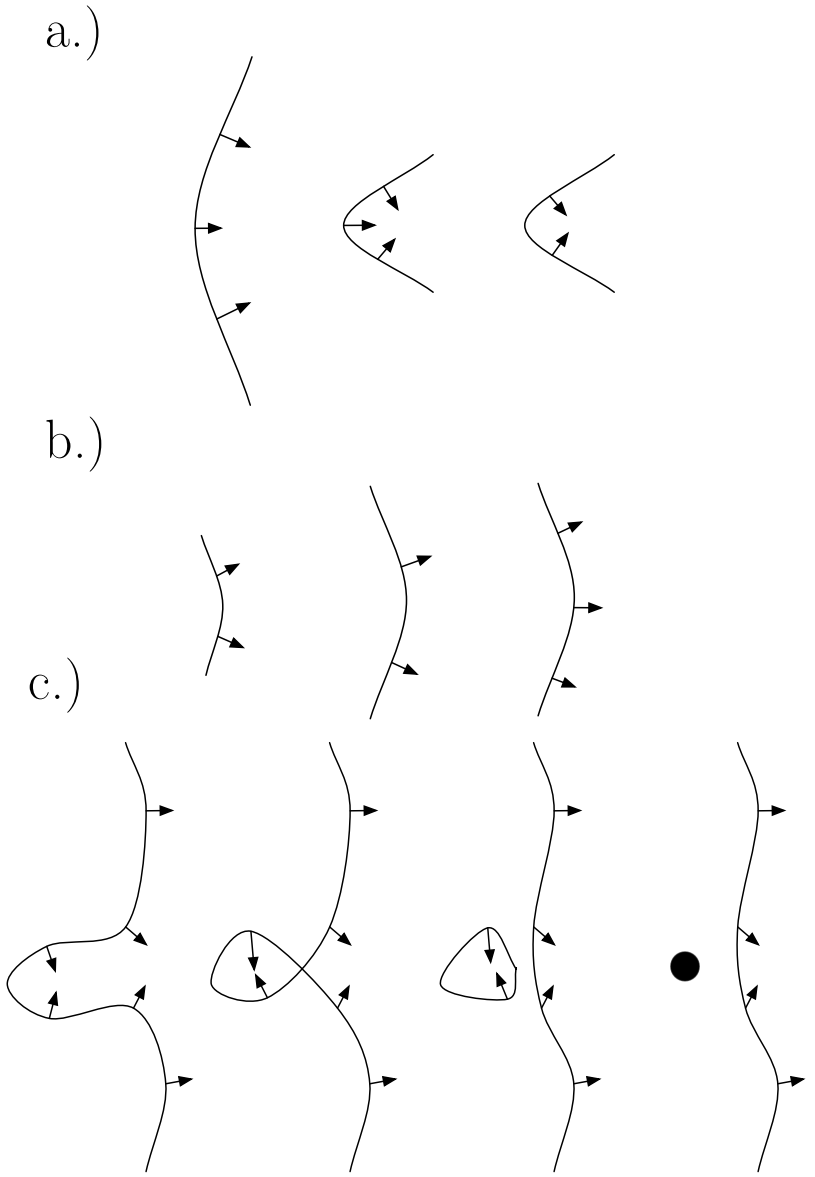

Figure C.1: Diagrams showing boundary discretisation refinements: (a) shows a discretisation point being removed as the surrounding points move closer together; (b) shows a discretisation point being added as the surrounding points move further apart; and (c) shows how topology changes may occur, in the far right graphic, a hole is immediately collapsed (which saves on computation time).

jump process. The value of $\delta t > 0$ is such that $\Delta t/\delta t$ is an integer, i.e., there are $\Delta t/\delta t$ iterations of the osteoblast position jump process for a single iteration of all other processes.

Algorithm 4: Algorithm for changing the size of the domain $\Omega(t)$ and boundary $B(t)$ for small time step $\Delta t > 0$.

Data: Specify small time step $\Delta t > 0$, osteoblast diffusion time step $\delta t > 0$ and two tolerances $\mathrm{TOL}_1 > \mathrm{TOL}_2$.

For a boundary discretised by N_B points labelled $\{\boldsymbol{y}_i\}_{i=1}^{N_B}$, the locations of the osteoblasts are constrained to the boundary discretisation $\{\boldsymbol{x}_i\}_{\rho_i=\mathrm{Ob}} \subset \{\boldsymbol{y}_i\}_{i=1}^{N_B}$.

% Osteoblast migration update.

for $k \leftarrow \{1, \ldots, \Delta t/\delta t\}$ **do**

  for $i \leftarrow$ `randperm`$(\{1, 2, \ldots, N\})$, $\varrho_i = Ob$ *and* $k_i = 0$ **do**

    % Allow osteoblast i to diffuse on the manifold B.

    Calculate the rate of jumping up $j_u = 2\kappa_{\mathrm{diff}}/\ell_u(\ell_u + \ell_d)$ and the rate of jumping down as for $j_d = 2\kappa_{\mathrm{diff}}/\ell_d(\ell_u + \ell_d)$ for $\ell_u = ||\boldsymbol{y}_i - \boldsymbol{y}_{i+1}||$ and $\ell_d = ||\boldsymbol{y}_{i-1} - \boldsymbol{y}_i||$.

    Draw a uniform random number r_u from distribution $R \sim \mathcal{U}(0, 1)$.

    if $r_u \leq j_u \delta t$ **then**

      % Osteoblast i moves up.

      $\boldsymbol{x}_i \leftarrow \boldsymbol{y}_{i-1}$

    Draw a uniform random number r_d from distribution $R \sim \mathcal{U}(0, 1)$.

    if $r_d \leq j_d \delta t$ **then**

      % Osteoblast i moves down.

      $\boldsymbol{x}_i \leftarrow \boldsymbol{y}_{i+1}$

% Boundary position update; note that the distance between used in $S(\boldsymbol{y}_i, \boldsymbol{x}_j)$ is the curve distance.

for $i \leftarrow \{1, 2, \ldots, N_B\}$ **do**

  $\boldsymbol{y}_i \leftarrow \boldsymbol{y}_i + \Delta t\, \boldsymbol{n}(\boldsymbol{y}_i) \sum_{\rho_j = \mathrm{Ob}} S(\boldsymbol{y}_i, \boldsymbol{x}_j)$.

% Boundary node deletion (See Fig. C.1a).

for $i \leftarrow$ `randperm`$(\{1, 2, \ldots, N_B - 1\})$ **do**

  if $||\boldsymbol{y}_i - \boldsymbol{y}_{i+1}|| < TOL_2$ **then**

    Delete discretisation point $\boldsymbol{y}_i$ provided there is no osteoblast present at this location.

% Boundary node addition (See Fig. C.1b).

for $i \leftarrow$ `randperm`$(\{1, 2, \ldots, N_B - 1\})$ **do**

  if $||\boldsymbol{y}_i - \boldsymbol{y}_{i+1}|| > TOL_1$ **then**

    Add discretisation point between points $\boldsymbol{y}_i, \boldsymbol{y}_{i+1}$, $\boldsymbol{y}^* = (\boldsymbol{y}_i + \boldsymbol{y}_{i+1})/2$.

% Boundary topology update (See Fig. C.1c).

for $i \leftarrow$ `randperm`$(\{1, 2, \ldots, N_B - 1\})$ **do**

  if $y_{i+1,2} < y_{i,2}$ **then**

    Change topology by allowing for a closed loop in addition to exterior boundary.

    Optional: Save on computation by instantly shrinking loop to single point.

Appendix D

Discussion on D_k

D.1 Proposed Mechanism: Cumulative Activation

One mechanism we considered was a cumulative activation effect, essentially each osteoblast has an intrinsic rate of differentiation (λ_1) plus an extrinsic contribution ($f = \gamma_1 k$). This extrinsic contribution corresponds to increasing the rate of osteoblast to osteocyte differentiation proportional to the number osteocytes that each osteoblast is in contact with. We write

$$D_k^{(1)} = \lambda_1 + \gamma_1 k \,. \tag{D.1}$$

One can calculate the mean osteoblast degree with the following analysis. Writing the first moment of $\tilde{v}_k$ as $\widetilde{\mathcal{M}}_1 = \sum_{k=0}^{\infty} k\tilde{v}_k$, then the equation for $k = 0$ is

$$\lambda_1 \tilde{p} + \gamma_1 \widetilde{\mathcal{M}}_1 = (\tilde{F} + \lambda_1)\tilde{v}_0 \,. \tag{D.2}$$

We can recursively find all $\tilde{v}_k$, and we determine that

$$\tilde{v}_k = \tilde{v}_{k-1} \frac{\tilde{F}}{\tilde{F} + \lambda_1 + \gamma_1 k} \,. \tag{D.3}$$

though the use of lower incomplete gamma functions defined as $\hat{\gamma}(s, x) = \int_0^x t^{s-1} e^{-t} \mathrm{d}t$, one can show that

$$\frac{\hat{\gamma}(s, x) e^x}{x^{s-1}} = \sum_{k=0}^{\infty} \frac{x^k}{(s+1)\dots(s+k)} \,, \tag{D.4}$$

and therefore

$$\langle k \rangle_{\mathrm{Ob}} = G\left(\frac{\tilde{F} + \lambda_1}{\gamma_1}, \frac{\tilde{F}}{\gamma_1} \right) - \frac{\lambda_1}{\gamma_1} \,, \tag{D.5}$$

for $G(s, x) = x^s e^{-x} / \hat{\gamma}(s, x)$ and

$$\tilde{q} = \frac{\lambda_1 + \gamma_1 \langle k \rangle_{\mathrm{Ob}}}{\eta \iota \sqrt{2\pi} L_z} \,. \tag{D.6}$$

We fit parameters as stated in Section 3.4.1.2. Specifying that the network has an excitatory effect on osteoblast differentiation, we set $\lambda_1 = \hat{D}/2$ and therefore

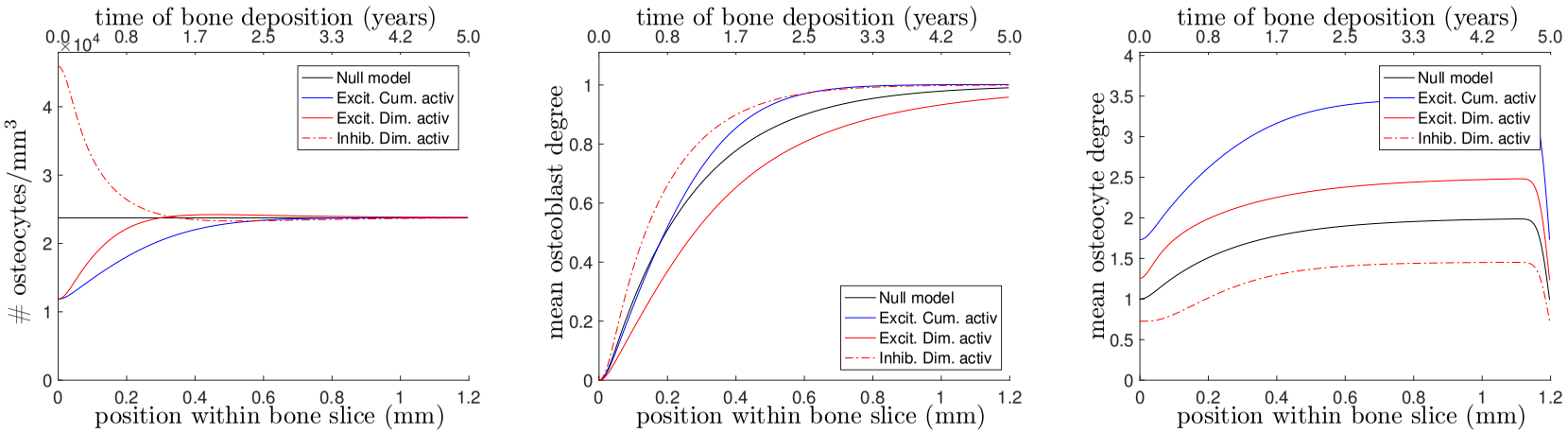

Figure D.1: (Left) Osteocyte density profile $[q(t, x = \tilde{\nu}t)]$, (middle) mean osteoblast degree over time $[\langle k(t = \tilde{\nu}t)\rangle_{\mathrm{Ob}}]$, and (right) mean osteocyte degree over time $[\langle k(t = \tilde{\nu}t)\rangle_{\mathrm{Ocy}}]$ when solving equations (3.7)–(3.8). The black line shows the null model, the blue line shows the excitatory cumulative activation model, and the red lines show the diminishing activation model, excitatory effects using the solid line and inhibitory effects using the dot-dashed line.

Table D.1: Choice in rate of osteoblast differentiation.

Symbol and form	Interpretation
$D_k^{(\text{null})} = \hat{D}$	No network effects.
This corresponds to the null hypothesis: the network does not impact the rate of osteoblast differentiation.	
$D_k^{(\text{swt})} = \left\{ \begin{array}{cc} \lambda & \text{if } k = 0 \\ \lambda + \gamma & \text{if } k \geq 1 \end{array} \right\}$	Switch-like influence.
The network does impact osteoblast differentiation rates but there are no cumulative effects, i.e., communicating with more osteocyte does not mean osteoblasts differentiate any faster/slower.	
$D_k^{(1)} = \lambda_1 + \gamma_1 k$	Cumulative activation.
The osteoblast will differentiate at a rate that increases proportional to how many osteocytes it is in communication with.	
$D_k^{(2)} = \left\{ \begin{array}{cc} \lambda_2 & \text{if } k = 0 \\ \lambda_2 + \gamma_2/k & \text{if } k \geq 1 \end{array} \right\}$	Cumulative inhibition.
The osteoblast will differentiate at a rate that increases inversely proportional to how many osteocytes it is in communication with.	

$\alpha_1 = 2.41 \times 10^{-3}\,\text{day}^{-1}$ and $\gamma_1 = 1.30 \times 10^{-3}\,\text{day}^{-1}$. Figure D.1 shows that when considering the cumulative activation model when compared to the null model, it takes approximately 3 years to obtain the desired osteocyte density of $\tilde{q} = 2.375 \times 10^4\,\text{mm}^{-3}$. This timescale is clearly too long to be considered biologically realistic. Additionally, were one to make $\gamma_1 < 0$, the rate $D_k^{(1)}$ can be negative which means that when using this model, inhibitory network effects are impossible. When considering the cumulative activation model, at the time of osteoblast differentiation a large quantity of a differentiation-promoting protein must be present in the osteoblasts. This protein would have therefore previously diffused along the dendrite structures. From a biological perspective, it seems more likely that only a small amount of protein should be required to travel though the dendrite structure to induce differentiation.

D.2 Proposed Mechanism: Diminishing Activation

Another mechanism considered is a cumulative inhibition effect. Each osteoblast has an intrinsic rate of differentiation (λ_2) plus an extrinsic contribution ($f = \gamma_2/k$). This extrinsic contribution corresponds to decreasing the rate of osteoblast to osteocyte differentiation inversely proportional to the number osteocytes that each osteoblast is contact with. We write

$$D_k^{(2)} = \left\{ \begin{array}{cc} \lambda_2 & \text{if } k = 0 \\ \lambda_2 + \frac{\gamma_2}{k} & \text{if } k \geq 1 \end{array} \right\}. \tag{D.7}$$

To calculate the mean osteoblast degree, one can make use of the series

$$H_f(x,y) = \sum_{k=0}^{\infty} f(k)[y+k+1]B(y+1,k+1)x^k\,, \tag{D.8}$$

for $f : \mathbb{N}_0 \to \mathbb{R}$ and $B(a,b) = \int_0^1 t^{a-1}(1-t)^{b-1}\mathrm{d}t$ is the beta function to calculate

$$\langle k\rangle_{\mathrm{Ob}} = \frac{H_k(\frac{\tilde{F}}{\tilde{F}+\lambda}, \frac{\gamma}{\tilde{F}+\lambda})}{H_1(\frac{\tilde{F}}{\tilde{F}+\lambda}, \frac{\gamma}{\tilde{F}+\lambda})}\,. \tag{D.9}$$

and

$$\tilde{q} = \frac{\tilde{F}+\lambda}{\eta\iota\sqrt{2\pi}L_z}\left[H_1\left(\frac{\tilde{F}}{\tilde{F}+\lambda}, \frac{\gamma}{\tilde{F}+\lambda}\right)\right]^{-1}\,. \tag{D.10}$$

Using equation (3.40), algebraic equations (D.9)–(D.10) are closed.

We fit parameters as stated in Section 3.4.1.2. Specifying that the network has an excitatory effect on osteoblast differentiation, we set $\lambda_2 = \hat{D}/2$ and therefore $\alpha_2 = 1.75 \times 10^{-3}\,\mathrm{day}^{-1}$ and $\gamma_2 = 4.56 \times 10^{-3}\,\mathrm{day}^{-1}$. Our diminishing activation model also has the possibility to allow for inhibition when $\lambda_2 > \hat{D}$; however the rate $D_k^{(2)}$ can be negative. For the greatest allowable amount of inhibition, one can set $\gamma_2 = -\lambda_2$. To maintain the desired travelling wave profile, the maximum value of λ_2 is given as $\lambda_2 = 190\% \times \hat{D}$ and in which case $\alpha_2 = 1.01 \times 10^{-3}\,\mathrm{day}^{-1}$.

Both the excitatory and (maximum) inhibitory effects are shown in Figure D.1. When compared to the null model, both models take approximately 2 years to get to the desired osteocyte density. This timescale is too long to be considered biologically realistic.

One emergent property we notice from this choice in differentiation mechanism is that when D_k is non-monotonic (i.e., has a maximum/minimum around $k = 1$), it appears that there is an over-shoot then adjustment period when viewing the density profile $q(t,x)$, e.g., the density starts below $\tilde{q}$, then over-reaches above $\tilde{q}$ before converging to $\tilde{q}$. In Figure D.1, this effect is very minimal, but different parameter choices can exacerbate this effect. When viewing 3-dimensional scans, one does observe similar behaviour around cement lines [39, 128]. The question now is how to choose and calibrate a function f; due to a lack of data and the fact that our model will never replicate reality perfectly, we only consider a switch-like mechanism in Chapter 3.

Appendix E

Finite Element Method for Simulated Ablation

In this appendix, we give both an existence and uniqueness proof for the solution to the elliptic PDE in Chapter 4, and also a method for FEM implementation.

E.1 Existence and Uniqueness

The original problem is stated as equations (4.3)–(4.4) for each $i \in \mathcal{N}$. Without any loss of generality, we can solve equations (4.1)–(4.2). Written out again, this is

$$\begin{aligned} \nabla^2 u - \alpha^2 u &= 0 \text{ in } \Omega\,, \\ \boldsymbol{n}_i \cdot \nabla u &= \gamma(c_i - u) \text{ on } \partial\mathscr{D}_i\,. \end{aligned} \tag{E.1}$$

We specify that $\partial\mathscr{D}_i$ is $\mathcal{C}^1$ regular, and we prove the existence and uniqueness of u in $H^1(\Omega)$ — although the solution is likely smoother.

The question whether we have to impose a limit condition of the form $\lim_{\|\boldsymbol{x}\|\to\infty} u(\boldsymbol{x}) = 0$ is *a priori* unclear. Intuitively, if we impose such a condition, it has to be zero, since the dissipation term would mean a null concentration at an infinite distance from the source (provided by the boundary condition). In fact, we will not have to impose this, as the unique solution of (E.1) is zero at infinity, due to the dissipation.

Let us recall that the Sobolev space $W_m^p(\Omega)$ is the space of functions defined as follows

$$W_m^p(\Omega) = \{u \in L^p(\Omega) \,|\, D^\beta u \in L^p(\Omega)\,, \forall \beta \leq m\}\,. \tag{E.2}$$

Here we will be particularly focused on the Hilbert space $H^1(\Omega) = W_1^2(\Omega)$ endowed with the H^1 norm defined by

$$\|v\|_{H^1(\Omega)} = \|v\|_{L^2(\Omega)} + \|\nabla v\|_{L^2(\Omega)}\,,\ \forall v \in H^1(\Omega)\,. \tag{E.3}$$

Proposition E.1.1. *The problem* (E.1) *has a unique solution in* $H^1(\Omega)$*.*

Proof. The weak formulation of the problem (E.1) is given by

$$a(u, v) = l(v)\,, \quad \forall v \in H^1(\Omega)\,, \tag{E.4}$$

for

$$a(u,v) = \int_\Omega \nabla u(\boldsymbol{x})\cdot\nabla v(\boldsymbol{x})\mathrm{d}\boldsymbol{x} + \alpha^2 \int_\Omega u(\boldsymbol{x})v(\boldsymbol{x})\mathrm{d}\boldsymbol{x} + \gamma \int_{\partial\Omega} u(\boldsymbol{x})v(\boldsymbol{x})\mathrm{d}S\,,\ \forall u,v \in H^1(\Omega)\,, \tag{E.5}$$

and

$$l(v) = \gamma \int_{\partial\Omega} \psi(\boldsymbol{x})v(\boldsymbol{x})\mathrm{d}S\,, \quad \forall v \in H^1(\Omega)\,, \tag{E.6}$$

where $\partial\Omega = \bigcup_i \partial\mathscr{D}_i$ and ψ is a function satisfying

$$\psi(\boldsymbol{x}) = c_i \text{ when } \boldsymbol{x} \in \mathscr{D}_i\,. \tag{E.7}$$

We now aim to prove continuity and coercivity of $a(u,v)$ on $H^1(\Omega)$, as well as the continuity of $l(v)$ on $H^1(\Omega)$ to satisfy the Lax–Milgram Theorem (Theorem 5.8 on page 83 in [50]). Specifically, we wish to show that

$$\begin{aligned} \text{Continuity of } a(u,v) &\Longleftrightarrow \exists A>0 \text{ s.t. } |a(u,v)| \le A\|u\|\|v\|\,, \\ \text{Coercivity of } a(u,v) &\Longleftrightarrow \exists B>0 \text{ s.t. } |a(u,u)| \ge B\|u\|\,, \\ \text{Continuity of } l(v) &\Longleftrightarrow \exists C>0 \text{ s.t. } |l(v)| \le C\|v\|\,. \end{aligned} \tag{E.8}$$

Continuity of $a(u,v)$

For $u,v \in H^1(\Omega)$, by nature of the modulus function, one can immediately write the following inequality

$$|a(u,v)| \le \left|\int_\Omega \nabla u(\boldsymbol{x})\cdot\nabla v(\boldsymbol{x})\mathrm{d}\boldsymbol{x}\right| + \alpha^2\left|\int_\Omega u(\boldsymbol{x})v(\boldsymbol{x})\mathrm{d}\boldsymbol{x}\right| + \gamma\left|\int_{\partial\Omega} u(\boldsymbol{x})v(\boldsymbol{x})\mathrm{d}S\right|. \tag{E.9}$$

The Cauchy-Schwartz inequality allows us then to write

$$|a(u,v)| \le \|\nabla u\|_{L^2(\Omega)}\|\nabla v\|_{L^2(\Omega)} + \alpha^2\|u\|_{L^2(\Omega)}\|v\|_{L^2(\Omega)} + \gamma\|u_{|\partial\Omega}\|_{L^2(\partial\Omega)}\|v_{|\partial\Omega}\|_{L^2(\partial\Omega)}. \tag{E.10}$$

According to the Trace Theorem [38], since $u,v \in H^1(\Omega)$ and because Ω is $\mathcal{C}^1$ and $\partial\Omega$ is bounded, then $u_{|\partial\Omega}, v_{|\partial\Omega} \in H^{\frac{1}{2}}(\partial\Omega)$ and the Trace operator is continuous from $H^1(\Omega)$ to $H^{\frac{1}{2}}(\partial\Omega)$. So, there exists a positive constant C such that

$$\|u_{|\partial\Omega}\|_{H^{\frac{1}{2}}(\partial\Omega)}\|v_{|\partial\Omega}\|_{H^{\frac{1}{2}}(\partial\Omega)} \le C^2\|u\|_{H^1(\Omega)}\|v\|_{H^1(\Omega)}. \tag{E.11}$$

According to the Sobolev Embedding Theorem [169], for an open set $U \subset \mathbb{R}^N$, $W^{m,p}(U) \subset L^q(U), \forall q \in (1,\infty)$ if $mp = N$. This is the case for us when $U = \partial\Omega$, $m = \frac{1}{2}$, $p = 2$ and $N = 1$. Moreover, this injection is continuous and then, for all $q \in (1,\infty)$, there is a positive constant D_q such that

$$\|u_{|\partial\Omega}\|_{L^q(\partial\Omega)}\|v_{|\partial\Omega}\|_{L^q(\partial\Omega)} \le D_q^2\|u_{|\partial\Omega}\|_{H^{\frac{1}{2}}(\partial\Omega)}\|v_{|\partial\Omega}\|_{H^{\frac{1}{2}}(\partial\Omega)}. \tag{E.12}$$

Therefore, using (E.11) and (E.12), we can write

$$\|u_{|\partial\Omega}\|_{L^q(\partial\Omega)}\|v_{|\partial\Omega}\|_{L^q(\partial\Omega)} \le C^2D_2^2\|u\|_{H^1(\Omega)}\|v\|_{H^1(\Omega)}. \tag{E.13}$$

From this inequality, we can write (E.10) as follows

$$|a(u,v)| \leq \|\nabla u\|_{L^2(\Omega)}\|\nabla v\|_{L^2(\Omega)} + \alpha^2\|u\|_{L^2(\Omega)}\|v\|_{L^2(\Omega)} + \gamma C^2 D_2^2\|u\|_{H^1(\Omega)}\|v\|_{H^1(\Omega)}\,. \tag{E.14}$$

Because $\|\nabla u\|_{L^2(\Omega)}\|\nabla v\|_{L^2(\Omega)} \leq \|u\|_{H^1(\Omega)}\|v\|_{H^1(\Omega)}$ and $\|u\|_{L^2(\Omega)}\| v\|_{L^2(\Omega)} \leq \|u\|_{H^1(\Omega)}\|v\|_{H^1(\Omega)}$, then the following inequality can be deduced from (E.14):

$$|a(u,v)| \leq (1 + \alpha^2 + \gamma C^2 D_2^2)\|u\|_{H^1(\Omega)}\|v\|_{H^1(\Omega)}\,, \tag{E.15}$$

allowing us to conclude that the bilinear form $a(u,v)$ is continuous on $H^1(\Omega)$.

Coercivity of $a(u,v)$

Let us prove now the coercivity of a. Let $u \in H^1(\Omega)$. We can write

$$|a(u,u)| = \|\nabla u\|^2_{L^2(\Omega)} + \alpha^2\|u\|^2_{L^2(\Omega)} + \gamma\int_{\partial\Omega}[u(\boldsymbol{x})]^2\mathrm{d}S\,. \tag{E.16}$$

Since the term $\gamma\int_{\partial\Omega}u^2\mathrm{d}S$ is positive, then

$$|a(u,u)| \geq \|\nabla u\|^2_{L^2(\Omega)} + \alpha^2\|u\|^2_{L^2(\Omega)}\,, \tag{E.17}$$

and therefore

$$|a(u,u)| \geq \min(1,\alpha^2)\|u\|^2_{H^1(\Omega)}\,, \tag{E.18}$$

which proves the coercivity of $a(u,v)$.

Continuity of $l(v)$

Let $v \in H^1(\Omega)$, we can immediately write the following inequality

$$|l(v)| \leq \gamma\int_{\partial\Omega}|\psi(\boldsymbol{x})v(\boldsymbol{x})|\mathrm{d}S\,. \tag{E.19}$$

Because the function ψ is bounded on Ω, we can write

$$|l(v)| \leq \gamma\|\psi\|_{L^\infty}\int_{\partial\Omega}|v(\boldsymbol{x})|\mathrm{d}S\,, \tag{E.20}$$

which can be written

$$|l(v)| \leq \|\psi\|_{L^\infty}\|v\|_{L^1(\partial\Omega)}\,. \tag{E.21}$$

Using again the Trace Theorem [38], since $v \in H^1(\Omega)$, we know that there exists a positive constant C such that

$$\|v_{|\partial\Omega}\|_{H^{\frac{1}{2}}(\partial\Omega)} \leq C\|v\|_{H^1(\Omega)}\,. \tag{E.22}$$

According once more to the Sobolev Embedding Theorem [169], there is a positive constant D_q such that

$$\|v_{|\partial\Omega}\|_{L^q(\partial\Omega)} \leq D_q\|v_{|\partial\Omega}\|_{H^{\frac{1}{2}}(\partial\Omega)}\,. \tag{E.23}$$

Therefore, using (E.22) and (E.23), we can write

$$\|v_{|\partial\Omega}\|_{L^1(\partial\Omega)} \leq CD_1\|v\|_{H^1(\Omega)}\,. \tag{E.24}$$

Then we can write (E.21) as follows

$$|l(v)| \leq \gamma C D_1 \|\psi\|_{L^\infty} \|v\|_{H^1(\Omega)} \,, \tag{E.25}$$

which proves the continuity of l on $H^1(\Omega)$. Then the Lax–Milgram Theorem [50] ensures that the problem (E.4) has a unique solution u on $H^1(\Omega)$. □

Remark E.1.1. *The previous proof does not work for the particular case $\gamma \to \infty$, which corresponds to a Dirichlet condition imposed on the surface of each cell. The proof of existence and uniqueness in this particular case would need to proceed differently. This case can be treated in defining the closed and convex set $K = \{v \in H^1(\Omega) \,|\, v - \psi \in H_0^1(\Omega)\}$ and applying Stampacchia's Theorem [50].*

E.2 Numerical Approach

Due to the geometrical effects involved in this problem, we use a Finite Element Method (FEM) approach. For a practical guide to implementation, see Ref. [1], and a theoretical guide to elliptic PDEs, see Ref. [50]. In weak form, our problem is for cell i removed on domain $\Omega_i = \Omega \cup \mathscr{D}_i = \mathbb{R}^2 \setminus \bigcup_{j \neq i} \mathscr{D}_j$. For $u_i, v \in H^1(\Omega_i)$, we have the weak form problem

$$\int_{\Omega_i} \nabla v(\boldsymbol{x}) \cdot \nabla u_i(\boldsymbol{x}) \mathrm{d}\boldsymbol{x} + \alpha^2 \int_{\Omega_i} v(\boldsymbol{x}) u_i(\boldsymbol{x}) \mathrm{d}\boldsymbol{x} + \gamma \int_{\partial\Omega_i} v(\boldsymbol{x}) u_i(\boldsymbol{x}) \mathrm{d}S = \gamma \int_{\partial\Omega_i} v(\boldsymbol{x}) \psi_i(\boldsymbol{x}) \mathrm{d}S \,, \tag{E.26}$$

where $\psi_i = \psi_i(\boldsymbol{x})$ is any function that satisfies

$$\psi_i(\boldsymbol{x}) = c_j \text{ when } \boldsymbol{x} \in \bar{\mathscr{D}}_j \,, \tag{E.27}$$

for $j = 1, \ldots, i-1, i+1, \ldots, N$. We use a standard continuous Galerkin method with piecewise linear basis functions $\{\eta_k(\boldsymbol{x})\}_{k=1}^K$ on the triangulation of Ω_i, $\mathcal{T} = \mathcal{T}(\Omega_i)$. For a triangle T with vertices (t_1, t_2, t_3), and the k^{th} basis function being located at vertex t_1, η_k is given as

$$\eta_k(x, y) = \frac{1}{2|T|} \det \begin{pmatrix} 1 & x & y \\ 1 & x_{t_2} & y_{t_2} \\ 1 & x_{t_3} & y_{t_3} \end{pmatrix} \,, \quad \forall (x, y) \in T \,, \tag{E.28}$$

for

$$|T| = \text{Area}(T) = \frac{1}{2} \det \begin{pmatrix} 1 & x_{t_1} & y_{t_1} \\ 1 & x_{t_2} & y_{t_2} \\ 1 & x_{t_3} & y_{t_3} \end{pmatrix} \,, \tag{E.29}$$

and $\eta_k(x, y) = 0$ for $(x, y) \notin T$. Therefore

$$\eta_k(x_l, y_l) = \delta_{kl} \,, \text{ for } k, l = 1, \ldots K \,. \tag{E.30}$$

Replacing v by the l^{th} basis function η_l and expanding u_i as the sum

$$u_i = \sum_k a_k \eta_k \,, \tag{E.31}$$

we obtain a linear system of equations

$$\left(L + \alpha^2 D + \gamma R\right) \boldsymbol{a} = \gamma \boldsymbol{r} \,, \tag{E.32}$$

and we solve for $\boldsymbol{a}$. Notice that changing constants (α, γ) do not require reassembly of matrices. The matrix entries are given as follows: the Laplacian matrix L is given by

$$L_{kl} = \int_{\Omega_i} \nabla \eta_k(\boldsymbol{x}) \cdot \nabla \eta_l(\boldsymbol{x}) \, \mathrm{d}\boldsymbol{x} \,; \tag{E.33}$$

the exponential decay matrix D is given by

$$D_{kl} = \int_{\Omega_i} \eta_k(\boldsymbol{x}) \, \eta_l(\boldsymbol{x}) \, \mathrm{d}\boldsymbol{x} \,; \tag{E.34}$$

and the Robin boundary condition comes in two parts, first the matrix R,

$$R_{kl} = \int_{\partial\Omega_i} \eta_k(\boldsymbol{x}) \, \eta_l(\boldsymbol{x}) \, \mathrm{d}S \,, \tag{E.35}$$

and then the vector $\boldsymbol{r}$ with entries

$$r_k = \int_{\partial\Omega_i} \eta_k(\boldsymbol{x}) \, \psi_i(\boldsymbol{x}) \, \mathrm{d}S \,. \tag{E.36}$$

Within this finite element framework, calculating the *baseline* is then

$$b_i = \sum_{T \in \mathcal{T}(\mathscr{D}_i)} \int_T a_k \eta_k(\boldsymbol{x}) \mathrm{d}\boldsymbol{x} \,, \tag{E.37}$$

$$= \sum_{T \in \mathcal{T}(\mathscr{D}_i)} \frac{|T|}{3} [a_{t_1} + a_{t_2} + a_{t_3}] \,. \tag{E.38}$$

Calculating these inner products between basis functions can be challenging. We now give a practical guide to implementation.

E.2.1 Practical Approach to FEM Implementation

To practically implement our FEM scheme, instead of putting in the entries to the matrices L, B, R and vector b individually, it is much simpler to do it each triangle or boundary edge at a time. We write L and B as a sum over the triangles T in the triangulation $\mathcal{T}(\Omega_i)$

$$L = \sum_{T \in \mathcal{T}(\Omega_i)} L^{(T)} \,, \tag{E.39}$$

$$D = \sum_{T \in \mathcal{T}(\Omega_i)} D^{(T)} \,. \tag{E.40}$$

The entries of $L^{(T)}$ are given as

$$L_{kl}^{(T)} = \left\{ \begin{array}{cc} \tilde{L}_{t_k,t_l}^{(T)} & \text{if vertices } (k,l) \text{ are part of triangle } T \\ 0 & \text{otherwise} \end{array} \right\}, \tag{E.41}$$

and analogously for $D^{(T)}$

$$D_{kl}^{(T)} = \left\{ \begin{array}{cc} \tilde{D}_{t_k,t_l}^{(T)} & \text{if vertices } (k,l) \text{ are part of triangle } T \\ 0 & \text{otherwise} \end{array} \right\}, \tag{E.42}$$

and therefore $\tilde{L}$ and $\tilde{D}$ are 3×3 matrices. These matrices have well known analytic formulations given as

$$\tilde{L} = \frac{|T|}{2} G\, G^{\dagger}\,, \tag{E.43}$$

for

$$G = \begin{pmatrix} 1 & 1 & 1 \\ x_{t_1} & x_{t_2} & x_{t_3} \\ y_{t_1} & y_{t_2} & y_{t_3} \end{pmatrix}^{-1} \begin{pmatrix} 0 & 0 \\ 1 & 0 \\ 0 & 1 \end{pmatrix}, \tag{E.44}$$

and

$$\tilde{D} = \frac{|T|}{12} \begin{pmatrix} 2 & 1 & 1 \\ 1 & 2 & 1 \\ 1 & 1 & 2 \end{pmatrix}. \tag{E.45}$$

For matrix R and vector $\boldsymbol{r}$, we sum over edges E that form the discretised boundary $\mathcal{E}(\partial\Omega_i)$

$$R = \sum_{E \in \mathcal{E}(\partial\Omega_i)} R^{(E)}\,, \tag{E.46}$$

$$\boldsymbol{b} = \sum_{E \in \mathcal{E}(\partial\Omega_i)} \boldsymbol{b}^{(E)}\,, \tag{E.47}$$

where

$$R_{kl}^{(E)} = \left\{ \begin{array}{cc} \tilde{R}_{e_k,e_l}^{(E)} & \text{if vertices } (k,l) \text{ are part of edge } E \\ 0 & \text{otherwise} \end{array} \right\}, \tag{E.48}$$

and therefore $\tilde{R}$ is a 2×2 matrix given as

$$\tilde{R} = \frac{|E|}{6} \begin{pmatrix} 2 & 1 \\ 1 & 2 \end{pmatrix}, \tag{E.49}$$

for $|E| = \text{Length}(E) = \|\boldsymbol{x}_{e_1} - \boldsymbol{x}_{e_2}\|$. Similarly for entries of vector $\boldsymbol{r}$

$$r_k = \left\{ \begin{array}{cc} \tilde{r}_{e_k}^{(E)} & \text{if vertex } k \text{ are part of edge } E \\ 0 & \text{otherwise} \end{array} \right\}, \tag{E.50}$$

and therefore

$$\tilde{r}_k = \frac{|E|}{2} \psi_i(\boldsymbol{x}_e)\,. \tag{E.51}$$

Bibliography

[1] J. Alberty, C. Carstensen, and S. A. Funken, *Remarks around 50 lines of Matlab: short finite element implementation*, Numerical Algorithms, 20 (1999), pp. 117–137.

[2] V. Almendro, Y.-K. Cheng, A. Randles, S. Itzkovitz, A. Marusyk, E. Ametller, X. Gonzalez-Farre, M. Muñoz, H. G. Russnes, Å. Helland, et al., *Inference of tumor evolution during chemotherapy by computational modeling and in situ analysis of genetic and phenotypic cellular diversity*, Cell Reports, 6 (2014), pp. 514–527.

[3] A. R. Anderson, K. A. Rejniak, P. Gerlee, and V. Quaranta, *Microenvironment driven invasion: a multiscale multimodel investigation*, Journal of Mathematical Biology, 58 (2009), pp. 579–624.

[4] A. R. Anderson, A. M. Weaver, P. T. Cummings, and V. Quaranta, *Tumor morphology and phenotypic evolution driven by selective pressure from the microenvironment*, Cell, 127 (2006), pp. 905 – 915.

[5] A. R. A. Anderson, M. Hassanein, K. M. Branch, J. Lu, N. A. Lobdell, J. Maier, D. Basanta, B. Weidow, A. Narasanna, C. L. Arteaga, A. B. Reynolds, V. Quaranta, L. Estrada, and A. M. Weaver, *Microenvironmental independence associated with tumor progression*, Cancer Research, 69 (2009), pp. 8797–8806.

[6] N. Andor, T. A. Graham, M. Jansen, L. C. Xia, C. A. Aktipis, C. Petritsch, H. P. Ji, and C. C. Maley, *Pan-cancer analysis of the extent and consequences of intratumor heterogeneity*, Nature Medicine, 22 (2016), pp. 105–113.

[7] A. Araujo, L. M. Cook, C. C. Lynch, and D. Basanta, *An integrated computational model of the bone microenvironment in bone-metastatic prostate cancer*, Cancer Research, 74 (2014), pp. 2391–2401.

[8] M. Archetti, *Evolutionary game theory of growth factor production: Implications for tumour heterogeneity and resistance to therapies*, British Journal of Cancer, 109 (2013), pp. 1056–1062.

[9] M. Aubry, *Metaphors in mathematics: Introduction and the case of algebraic geometry*. Unpublished, 2009.

[10] C. I. Bargmann and L. Avery, *Laser killing of cells in Caenorhabditis elegans*, Methods in Cell Biology, 48 (1995), pp. 225–250.

[11] M. Barthelemy, *Spatial networks*, Physics Reports, 499 (2011), pp. 1–101.

[12] M. Barthelemy and R. Louf, *Morphogenesis of Urban Networks*, Springer-Verlag, 2017.

[13] D. Basanta and A. R. Anderson, *Exploiting ecological principles to better understand cancer progression and treatment*, Interface Focus, 3 (2013), p. 20130020.

[14] M. Bisi and L. Desvillettes, *From reactive Boltzmann equations to reaction–diffusion systems*, Journal of Statistical Physics, 124 (2006), pp. 881–912.

[15] B. Blonder, C. Violle, L. P. Bentley, and B. J. Enquist, *Venation networks and the origin of the leaf economics spectrum*, Ecology Letters, 14 (2011), pp. 91–100.

[16] M. Boguñá and R. Pastor-Satorras, *Class of correlated random networks with hidden variables*, Physical Review E, 68 (2003), p. 036112.

[17] M. Boguñá, R. Pastor-Satorras, A. Díaz-Guilera, and A. Arenas, *Emergence of clustering, correlations, and communities in a social network model*. arXiv:cond-mat/0309263, 2003.

[18] M. d. Bono and A. Villu Maricq, *Neuronal substrates of complex behaviors in C. elegans*, Annual Review of Neuroscience, 28 (2005), pp. 451–501.

[19] M. Bruna and S. J. Chapman, *Excluded-volume effects in the diffusion of hard spheres*, Physical Review E, 85 (2012), p. 011103.

[20] P. R. Buenzli, *Osteocytes as a record of bone formation dynamics: A mathematical model of osteocyte generation in bone matrix*, Journal of Theoretical Biology, 364 (2015), pp. 418 – 427.

[21] P. R. Buenzli, P. Pivonka, and D. W. Smith, *Bone refilling in cortical basic multicellular units: Insights into tetracycline double labelling from a computational model*, Biomechanics and Modeling in Mechanobiology, 13 (2014), pp. 185–203.

[22] P. R. Buenzli and N. A. Sims, *Quantifying the osteocyte network in the human skeleton*, Bone, 75 (2015), pp. 144–150.

[23] J. M. Burgers, *The Boltzmann equation for flows with chemical reactions*, Planetary and Space Science, 3 (1961), pp. 4–11.

[24] S. Burra, D. P. Nicolella, W. L. Francis, C. J. Freitas, N. J. Mueschke, K. Poole, and J. X. Jiang, *Dendritic processes of osteocytes are mechanotransducers that induce the opening of hemichannels*, Proceedings of the National Academy of Sciences, 107 (2010), pp. 13648–13653.

[25] J. A. Carrillo, M. R. D'Orsogna, and V. Panfarov, *Double milling in self-propelled swarms from kinetic theory*, Kinetic and Related Models, 2 (2009), pp. 363–378.

[26] N. P. Carter, *Methods and strategies for analyzing copy number variation using DNA microarrays*, Nature Genetics, 39 (2007), pp. S16–S21.

[27] Y. Carter, J. L. Suchorab, C. D. L. Thomas, J. G. Clement, and D. M. L. Cooper, *Normal variation in cortical osteocyte lacunar parameters in healthy young males*, Journal of Anatomy, 225 (2014), pp. 328–336.

[28] CC BY-NC-ND 4.0. `https://creativecommons.org/licenses/by-nc-nd/4.0/`.

[29] C. Cercignani, *The Boltzmann Equation and Its Applications*, Springer-Verlag, 1988.

[30] C. Cercignani, R. Illner, and M. Pulvirenti, *The Mathematical Theory of Dilute Gases*, Springer, 1994.

[31] W. Chen, R. Erban, and S. J. Chapman, *From Brownian dynamics to Markov chain: An ion channel example*, SIAM Journal on Applied Mathematics, 74 (2014), pp. 208–235.

[32] J. L. Cherry and F. R. Adler, *How to make a biological switch*, Journal of Theoretical Biology, 203 (2000), pp. 117–133.

[33] E. C. Connolly, J. Freimuth, and R. J. Akhurst, *Complexities of TGF-β targeted cancer therapy*, International Journal of Biological Sciences, 8 (2012), pp. 964–978.

[34] S. Dallas, *Dynamics of bone extracellular matrix assembly and mineralization*, Journal of Musculoskeletal and Neuronal Interactions, 6 (2006), p. 370.

[35] S. L. Dallas and L. F. Bonewald, *Dynamics of the transition from osteoblast to osteocyte*, Annals of the New York Academy of Sciences, 1192 (2010), pp. 437–443.

[36] D. L. Davies and D. W. Bouldin, *A cluster separation measure*, IEEE Transactions on Pattern Analysis and Machine Intelligence, (1979), pp. 224–227.

[37] P. Degond, L. Pareschi, and G. Russo, *Modeling and Computational Methods for Kinetic Equations*, Birkhäuser, 2004.

[38] Z. Ding, *A proof of the trace theorem of Sobolev spaces on Lipschitz domains*, Proceedings of the American Mathematical Society, 124 (1996), pp. 591–600.

[39] P. Dong, S. Haupert, B. Hesse, M. Langer, P.-J. Gouttenoire, V. Bousson, and F. Peyrin, *3D osteocyte lacunar morphometric properties and distributions in human femoral cortical bone using synchrotron radiation micro-CT images*, Bone, 60 (2014), pp. 172–185.

[40] R. Durrett and S. Levin, *The importance of being discrete (and spatial)*, Theoretical Population Biology, 46 (1994), pp. 363 – 394.

[41] S. Eisenberger, K. Ackermann, G. Voggenreiter, H. Sültmann, C. Kasperk, and W. Pyerin, *Metastases and multiple myeloma generate distinct transcriptional footprints in osteocytes in vivo*, The Journal of Pathology, 214 (2008), pp. 617–626.

[42] P. Erdős and A. Rényi, *On the evolution of random graphs*, Publications of the Mathematical Institute of the Hungarian Academy of Sciences, Series A, 5 (1960), pp. 17–61.

[43] B. Fornberg and N. Flyer, *A primer on radial basis functions with applications to the geosciences*, vol. 87, SIAM, 2015.

[44] T. A. Franz-Odendaal, B. K. Hall, and P. E. Witten, *Buried alive: How osteoblasts become osteocytes*, Developmental Dynamics, 235 (2006), pp. 176–190.

[45] I. Gallagher, L. Saint-Raymond, and B. Texier, *From Newton to Boltzmann: Hard spheres and short-range potentials*, American Mathematical Society, 2014.

[46] R. Gallotti and M. Barthelemy, *Anatomy and efficiency of urban multimodal mobility*, Scientific Reports, 4 (2014), p. 6911.

[47] M. Gerlinger, A. J. Rowan, S. Horswell, J. Larkin, D. Endesfelder, E. Gronroos, P. Martinez, N. Matthews, A. Stewart, P. Tarpey, et al., *Intratumor heterogeneity and branched evolution revealed by multiregion sequencing*, New England Journal of Medicine, 366 (2012), pp. 883–892.

[48] M. B. Gerstein, C. Bruce, J. S. Rozowsky, D. Zheng, J. Du, J. O. Korbel, O. Emanuelsson, Z. D. Zhang, S. Weissman, and M. Snyder, *What is a gene, Post-ENCODE? History and updated definition*, Genome Research, 17 (2007), pp. 669–681.

[49] F. Ghaznavi, A. Evans, A. Madabhushi, and M. Feldman, *Digital imaging in pathology: whole-slide imaging and beyond*, Annual Review of Pathology: Mechanisms of Disease, 8 (2013), pp. 331–359.

[50] D. Gilbarg and N. S. Trudinger, *Elliptic partial differential equations of second order*, Springer, 2015.

[51] D. T. Gillespie, *Exact stochastic simulation of coupled chemical reactions*, The Journal of Physical Chemistry, 81 (1977), pp. 2340–2361.

[52] D. Glasscock, *What is ... a Graphon?*, Notices of the AMS, 62 (2015).

[53] A. R. Gohel, A. R. Hand, and G. A. Gronowicz, *Immunogold localization of beta 1-integrin in bone: effect of glucocorticoids and insulin-like growth factor I on integrins and osteocyte formation*, Journal of Histochemistry & Cytochemistry, 43 (1995), pp. 1085–1096.

[54] J. M. Graham, B. P. Ayati, S. A. Holstein, and J. A. Martin, *The role of osteocytes in targeted bone remodeling: A mathematical model*, PLoS ONE, 8 (2013), p. e63884.

[55] M. Greaves and C. C. Maley, *Clonal evolution in cancer*, Nature, 481 (2012), pp. 306–313.

[56] T. Gross and B. Blasius, *Adaptive coevolutionary networks: A review*, Journal of the Royal Society Interface, 5 (2008), pp. 259–271.

[57] E. Hairer, C. Lubich, and G. Wanner, *Geometric numerical integration illustrated by the störmer–verlet method*, Acta numerica, 12 (2003), pp. 399–450.

[58] K. Hannah, C. Thomas, J. Clement, F. D. Carlo, and A. Peele, *Bimodal distribution of osteocyte lacunar size in the human femoral cortex as revealed by micro-CT*, Bone, 47 (2010), pp. 866 – 871.

[59] S. Harris, *An introduction to the theory of the Boltzmann equation*, Holt, Reinhart and Winston, Inc, 1971.

[60] I. R. Hart, *'Seed and soil' revisited: mechanisms of site-specific metastasis*, Cancer and Metastasis Reviews, 1 (1982), pp. 5–16.

[61] J. Haskovec, P. Markowich, and B. Perthame, *Mathematical analysis of a PDE system for biological network formation*, Communications in Partial Differential Equations, 40 (2015), pp. 918–956.

[62] J. M. Heather and B. Chain, *The sequence of sequencers: The history of sequencing DNA*, Genomics, 107 (2016), pp. 1–8.

[63] L. L. M. Heaton, E. López, P. K. Maini, M. D. Fricker, and N. S. Jones, *Growth-induced mass flows in fungal networks*, Proceedings of the Royal Society B: Biological Sciences, 277 (2010), pp. 3265–3270.

[64] A. Heindl, S. Nawaz, and Y. Yuan, *Mapping spatial heterogeneity in the tumor microenvironment: a new era for digital pathology*, Laboratory Investigation, 95 (2015), pp. 377–384.

[65] D. J. Higham, *An algorithmic introduction to numerical simulation of stochastic differential equations*, SIAM Review, 43 (2001), pp. 525–546.

[66] T. Hillen, *On the L^2-moment closure of transport equations: The general case*, Discrete and Continuous Dynamical Systems-Series B, 5 (2003), pp. 299–318.

[67] ——, *On the L^2-moment closure of transport equations: The Cattaneo approximation*, Discrete and Continuous Dynamical Systems-Series B, 4 (2004), pp. 961–982.

[68] D. Hu and D. Cai, *Adaptation and optimization of biological transport networks*, Physical Review Letters, 111 (2013), p. 138701.

[69] L. Hu, K. Ru, L. Zhang, Y. Huang, X. Zhu, H. Liu, A. Zetterberg, T. Cheng, and W. Miao, *Fluorescence in situ hybridization (FISH): an increasingly demanded tool for biomarker research and personalized medicine*, Biomarker Research, 2 (2014), p. 3.

[70] J. D. Humphrey, E. R. Dufresne, and M. A. Schwartz, *Mechanotransduction and extracellular matrix homeostasis*, Nature Reviews Molecular Cell Biology, 15 (2014), pp. 802–812.

[71] R. Illner and M. Pulvirenti, *A derivation of the BBGKY-hierarchy for hard-sphere particle systems*, Transport Theory and Statistical Physics, 16 (1987), pp. 997–1012.

[72] Y. Ishihara, Y. Sugawara, H. Kamioka, N. Kawanabe, H. Kurosaka, K. Naruse, and T. Yamashiro, *In situ imaging of the autonomous intracellular $Ca2^+$ oscillations of osteoblasts and osteocytes in bone*, Bone, 50 (2012), pp. 842 – 852.

[73] S. Ithimakin, K. C. Day, F. Malik, Q. Zen, S. J. Dawsey, T. F. Bersano-Begey, A. A. Quraishi, K. W. Ignatoski, S. Daignault, A. Davis, et al., *HER2 drives luminal breast cancer stem cells in the absence of HER2 amplification: implications for efficacy of adjuvant trastuzumab*, Cancer Research, 73 (2013), pp. 1635–1646.

[74] R. K. Jain, *Determinants of tumor blood flow: A review*, Cancer research, 48 (1988), pp. 2641–2658.

[75] R. L. Jilka, B. Noble, and R. S. Weinstein, *Osteocyte apoptosis*, Bone, 54 (2013), pp. 264–271. The Osteocyte.

[76] H. Kamioka, T. Honjo, and T. Takano-Yamamoto, *A three-dimensional distribution of osteocyte processes revealed by the combination of confocal laser scanning microscopy and differential interference contrast microscopy*, Bone, 28 (2001), pp. 145–149.

[77] O. D. Kennedy, D. M. Laudier, R. J. Majeska, H. B. Sun, and M. B. Schaffler, *Osteocyte apoptosis is required for production of osteoclastogenic signals following bone fatigue* in vivo, Bone, 64 (2014), pp. 132 – 137.

[78] M. Kerschnitzki, P. Kollmannsberger, M. Burghammer, G. N. Duda, R. Weinkamer, W. Wagermaier, and P. Fratzl, *Architecture of the osteocyte network correlates with bone material quality*, Journal of Bone and Mineral Research, 28 (2013), pp. 1837–1845.

[79] M. Kivelä, A. Arenas, M. Barthelemy, J. P. Gleeson, Y. Moreno, and M. A. Porter, *Multilayer networks*, Journal of Complex Networks, 2 (2014), pp. 203–271.

[80] S. Klus, P. Koltai, and C. Schütte, *On the numerical approximation of the Perron–Frobenius and Koopman operator*, Journal of Computational Dynamics, (2015).

[81] M. Knothe Tate, R. Steck, M. Forwood, and P. Niederer, In vivo *demonstration of load-induced fluid flow in the rat tibia and its potential implications for processes associated with functional adaptation*, Journal of Experimental Biology, 203 (2000), pp. 2737–2745.

[82] H. Korkaya and M. S. Wicha, *HER-2, notch, and breast cancer stem cells: targeting an axis of evil*, Clinical Cancer Research, 15 (2009), pp. 1845–1847.

[83] P. L. Krapivsky and S. Redner, *Organization of growing random networks*, Physical Review E, 63 (2001), p. 066123.

[84] P. L. Krapivsky, S. Redner, and E. Ben-Naim, *A Kinetic View of Statistical Physics*, Cambridge University Press, 2010.

[85] P. L. Krapivsky, G. J. Rodgers, and S. Redner, *Degree distributions of growing networks*, Physical Review Letters, 86 (2001), p. 5401.

[86] D. Krioukov and M. Ostilli, *Duality between equilibrium and growing networks*, Physical Review E, 88 (2013), p. 022808.

[87] S. Y. Kristinsson, A. R. Minter, N. Korde, E. Tan, and O. Landgren, *Bone disease in multiple myeloma and precursor disease: novel diagnostic approaches and implications on clinical management*, Expert Review of Molecular Diagnostics, 11 (2011), pp. 593–603.

[88] B. L. Krock, N. Skuli, and M. C. Simon, *Hypoxia-induced angiogenesis: good and evil*, Genes & Cancer, 2 (2011), pp. 1117–1133.

[89] C. Kuehn, *Moment closure a brief review*, in Control of Self-Organizing Nonlinear Systems, Springer, 2016, pp. 253–271.

[90] S. H. Lee, M. D. Fricker, and M. A. Porter, *Mesoscale analyses of fungal networks*. advanced access; available at doi:10.1093/comnet/cnv034, 2016.

[91] Y.-C. Lee, C.-J. Cheng, M. A. Bilen, J.-F. Lu, R. L. Satcher, L.-Y. Yu-Lee, G. E. Gallick, S. N. Maity, and S.-H. Lin, *BMP4 promotes prostate tumor growth in bone through osteogenesis*, Cancer Research, 71 (2011), pp. 5194–5203.

[92] C. Lerebours and P. Buenzli, *Towards a cell-based mechanostat theory of bone: the need to account for osteocyte desensitisation and osteocyte replacement*, Journal of Biomechanics, 49 (2016), pp. 2600–2606.

[93] C. J. Logothetis and S.-H. Lin, *Osteoblasts in prostate cancer metastasis to bone*, Nature Reviews Cancer, 5 (2005), pp. 21–28.

[94] R. Louf and M. Barthelemy, *How congestion shapes cities: From mobility patterns to scaling*, Scientific Reports, 4 (2014), p. 5561.

[95] S. J. Lunt, N. Chaudary, and R. P. Hill, *The tumor microenvironment and metastatic disease*, Clinical & Experimental Metastasis, 26 (2009), pp. 19–34.

[96] A. Magnifico, L. Albano, S. Campaner, D. Delia, F. Castiglioni, P. Gasparini, G. Sozzi, E. Fontanella, S. Menard, and E. Tagliabue, *Tumor-initiating cells of HER2-positive carcinoma cell lines express the highest oncoprotein levels and are sensitive to trastuzumab*, Clinical Cancer Research, 15 (2009), pp. 2010–2021.

[97] C. C. Maley, P. C. Galipeau, J. C. Finley, V. J. Wongsurawat, X. Li, C. A. Sanchez, T. G. Paulson, P. L. Blount, R.-A. Risques, P. S. Rabinovitch, et al., *Genetic clonal diversity predicts progression to esophageal adenocarcinoma*, Nature Genetics, 38 (2006), pp. 468–473.

[98] V. Marceau, P.-A. Noël, L. Hébert-Dufresne, A. Allard, and L. J. Dubé, *Adaptive networks: Coevolution of disease and topology*, Physical Review E, 82 (2010), p. 036116.

[99] G. Marotti, *The osteocyte as a wiring transmission system*, Journal of Musculoskeletal and Neuronal Interactions, (2000), pp. 133–136.

[100] G. Marotti, M. Ferretti, M. Muglia, C. Palumbo, and S. Palazzini, *A quantitative evaluation of osteoblast-osteocyte relationships on growing endosteal surface of rabbit tibiae*, Bone, 13 (1992), pp. 363–368.

[101] G. Marotti, M. Ferretti, F. Remaggi, and C. Palumbo, *Quantitative evaluation on osteocyte canalicular density in human secondary osteons*, Bone, 16 (1995), pp. 125–128.

[102] P. Martinez, M. R. Timmer, C. T. Lau, S. Calpe, M. del Carmen Sancho-Serra, D. Straub, A.-M. Baker, S. L. Meijer, F. J. Ten Kate, R. C. Mallant-Hent, et al., *Dynamic clonal equilibrium and predetermined cancer risk in Barrett's oesophagus*, Nature Communications, 7 (2016), p. 12158.

[103] A. Marusyk, V. Almendro, and K. Polyak, *Intra-tumour heterogeneity: a looking glass for cancer?*, Nature Reviews Cancer, 12 (2012), pp. 323–334.

[104] R. Metzler and J. Klafter, *The random walk's guide to anomalous diffusion: A fractional dynamics approach*, Physical Reports, 339 (2000), pp. 1–77.

[105] M. M. Moasser, *The oncogene HER2: its signaling and transforming functions and its role in human cancer pathogenesis*, Oncogene, 26 (2007), pp. 6469–6487.

[106] C. Moore, G. Ghoshal, and M. E. J. Newman, *Exact solutions for models of evolving networks with addition and deletion of nodes*, Physical Review E, 74 (2006), p. 036121.

[107] A. Moroz, M. C. Crane, G. Smith, and D. I. Wimpenny, *Phenomenological model of bone remodeling cycle containing osteocyte regulation loop*, Biosystems, 84 (2006), pp. 183–190.

[108] R. Natrajan, H. Sailem, F. K. Mardakheh, M. A. Garcia, C. J. Tape, M. Dowsett, C. Bakal, and Y. Yuan, *Microenvironmental heterogeneity parallels breast cancer progression: A histology–genomic integration analysis*, PLoS Medicine, 13 (2016), p. E1001961.

[109] M. E. J. Newman, *Networks: An Introduction*, Oxford University Press, 2010.

[110] P. C. Nowell, *The clonal evolution of tumor cell populations*, Science, 194 (1976), pp. 23–28.

[111] R. O'Dea, H. Byrne, and S. Waters, *Continuum modelling of in vitro tissue engineering: A review*, in Computational Modeling in Tissue Engineering, L. Geris, ed., Studies in Mechanobiology, Tissue Engineering and Biomaterials, Springer-Verlag, 2013, pp. 229–266.

[112] H. Ohtsuki, C. Hauert, E. Lieberman, and M. A. Nowak, *A simple rule for the evolution of cooperation on graphs and social networks*, Nature, 441 (2006), pp. 502–505.

[113] B. Øksendal, *Stochastic Differential Equations: An Introduction with Applications (Universitext)*, Springer, 6th ed., Jan. 2014.

[114] H. Othmer, S. R. Dunbar, and W. Alt, *Models of dispersal in biological systems*, Journal of Mathematical Biology, 26 (1988), pp. 263–298.

[115] C. Palumbo, M. Ferretti, and G. Marotti, *Osteocyte dendrogenesis in static and dynamic bone formation: an ultrastructural study*, The Anatomical Record Part A: Discoveries in Molecular, Cellular, and Evolutionary Biology, 278 (2004), pp. 474–480.

[116] C. Palumbo, S. Palazzini, D. Zaffe, and G. Marotti, *Osteocyte differentiation in the tibia of newborn rabbit: an ultrastructural study of the formation of cytoplasmic processes*, Cells Tissues Organs, 137 (1990), pp. 350–358.

[117] A. Parfitt, *Osteonal and hemi-osteonal remodeling: the spatial and temporal framework for signal traffic in adult human bone*, Journal of Cellular Biochemistry, 55 (1994), pp. 273–286.

[118] U. E. Pazzaglia, T. Congiu, M. Marchese, and C. Dell'orbo, *The shape modulation of osteoblast–osteocyte transformation and its correlation with the fibrillar organization in secondary osteons: a SEM study employing the graded osmic maceration technique*, Cell and Tissue Research, 340 (2010), pp. 533–540.

[119] U. E. Pazzaglia, T. Congiu, V. Sibilia, and D. Quacci, *Osteoblast-osteocyte transformation. a SEM densitometric analysis of endosteal apposition in rabbit femur*, Journal of Anatomy, 224 (2014), pp. 132–141.

[120] J. Peacock, *Two-dimensional goodness-of-fit testing in astronomy*, Monthly Notices of the Royal Astronomical Society, 202 (1983), pp. 615–627.

[121] D. J. Pearce, A. M. Miller, G. Rowlands, and M. S. Turner, *Role of projection in the control of bird flocks*, Proceedings of the National Academy of Sciences, 111 (2014), pp. 10422–10426.

[122] M. Penrose, *Random Geometric Graphs*, Oxford University Press, Oxford, UK, 2003.

[123] B. Pettit, Z. Akos, T. Vicsek, and D. Biro, *Speed determines leadership and leadership determines learning during pigeon flocking*, Current Biology, 25 (2015), pp. 3132–3137.

[124] A. Piattelli, L. Artese, E. Penitente, F. Iaculli, M. Degidi, C. Mangano, J. A. Shibli, P. G. Coelho, V. Perrotti, and G. Iezzi, *Osteocyte density in the peri-implant bone of implants retrieved after different time periods (4 weeks to 27 years)*, Journal of Biomedical Materials Research Part B: Applied Biomaterials, 102 (2014), pp. 239–243.

[125] M. Pickup, S. Novitskiy, and H. L. Moses, *The roles of TGFβ in the tumour microenvironment*, Nature Reviews Cancer, 13 (2013), pp. 788–799.

[126] P. Pivonka and S. V. Komarova, *Mathematical modeling in bone biology: From intracellular signaling to tissue mechanics*, Bone, 47 (2010), pp. 181–189.

[127] K. E. Poole, R. L. Van Bezooijen, N. Loveridge, H. Hamersma, S. E. Papapoulos, C. W. Löwik, and J. Reeve, *Sclerostin is a delayed secreted product of osteocytes that inhibits bone formation*, The FASEB Journal, 19 (2005), pp. 1842–1844.

[128] J. Power, M. Doube, R. L. Van Bezooijen, N. Loveridge, and J. Reeve, *Osteocyte recruitment declines as the osteon fills in: interacting effects of osteocytic sclerostin and previous hip fracture on the size of cortical canals in the femoral neck*, Bone, 50 (2012), pp. 1107–1114.

[129] D. J. d. S. Price, *Little Science, Big Science and Beyond*, Columbia University Press, 1986.

[130] L. Qin, A. T. Mak, C. Cheng, L. Hung, and K. Chan, *Histomorphological study on pattern of fluid movement in cortical bone in goats*, The Anatomical Record, 255 (1999), pp. 380–387.

[131] K. A. Rejniak and A. R. A. Anderson, *Hybrid models of tumor growth*, Wiley Interdisciplinary Reviews: Systems Biology and Medicine, 3 (2011), pp. 115–125.

[132] A. G. Robling, A. B. Castillo, and C. H. Turner, *Biomechanical and molecular regulation of bone remodeling*, Annual Review of Biomedical Engineering, 8 (2006), pp. 455–498. PMID: 16834564.

[133] J. M. Rosen and K. Roarty, *Paracrine signaling in mammary gland development: what can we learn about intratumoral heterogeneity?*, Breast Cancer Research, 16 (2014), p. 3358.

[134] M. P. Roudier, L. D. True, C. S. Higano, H. Vesselle, W. Ellis, P. Lange, and R. L. Vessella, *Phenotypic heterogeneity of end-stage prostate carcinoma metastatic to bone*, Human Pathology, 34 (2003), pp. 646–653.

[135] M. D. Ryser, S. V. Komarova, and N. Nigam, *The cellular dynamics of bone remodeling: A mathematical model*, SIAM Journal on Applied Mathematics, 70 (2010), pp. 1899–1921.

[136] M. D. Ryser, N. Nigam, and S. V. Komarova, *Mathematical modeling of spatio-temporal dynamics of a single bone multicellular unit*, Journal of Bone and Mineral Research, 24 (2009), pp. 860–870.

[137] M. D. Ryser, Y. Qu, and S. V. Komarova, *Osteoprotegerin in bone metastases: Mathematical solution to the puzzle*, PLoS Computational Biology, 8 (2012), p. e1002703.

[138] R. Sapir-Koren and G. Livshits, *Osteocyte control of bone remodeling: Is sclerostin a key molecular coordinator of the balanced bone resorption–formation cycles?*, Osteoporosis International, (2014), pp. 1–16.

[139] T. N. Schumacher and R. D. Schreiber, *Neoantigens in cancer immunotherapy*, Science, 348 (2015), pp. 69–74.

[140] J. G. Skedros, J. L. Holmes, E. G. Vajda, and R. D. Bloebaum, *Cement lines of secondary osteons in human bone are not mineral-deficient: new data in a historical perspective*, The Anatomical Record Part A: Discoveries in Molecular, Cellular, and Evolutionary Biology, 286A (2005), pp. 781–803.

[141] J. M. Smith, *Evolution and the Theory of Games*, Cambridge university press, 1982.

[142] H. Spohn, *Large Scale Dynamics of Interacting Particles*, Springer, 1991.

[143] R. Steck and M. Knothe Tate, In silico *stochastic network models that emulate the molecular sieving characteristics of bone*, Annals of Biomedical Engineering, 33 (2005), pp. 87–94.

[144] P. S. Steeg, *Targeting metastasis*, Nature Reviews Cancer, 16 (2016), pp. 201–218.

[145] J. C. Stinson, *The ailing mythical osteocyte*, Medical Hypotheses, 1 (1975), pp. 186–190.

[146] H. Stone, *A simple derivation of the time-dependent convective-diffusion equation for surfactant transport along a deforming interface*, Physics of Fluids A: Fluid Dynamics, 2 (1990), pp. 111–112.

[147] Y. Sugawara, R. Ando, H. Kamioka, Y. Ishihara, T. Honjo, N. Kawanabe, H. Kurosaka, T. Takano-Yamamoto, and T. Yamashiro, *The three-dimensional morphometry and cell–cell communication of the osteocyte network in chick and mouse embryonic calvaria*, Calcified Tissue International, 88 (2011), pp. 416–424.

[148] Y. Sugawara, H. Kamioka, T. Honjo, K. ichi Tezuka, and T. Takano-Yamamoto, *Three-dimensional reconstruction of chick calvarial osteocytes and their cell processes using confocal microscopy*, Bone, 36 (2005), pp. 877–883.

[149] C. Swanton, *Intratumor heterogeneity: evolution through space and time*, Cancer Research, 72 (2012), pp. 4875–4882.

[150] G. Szabó and G. Fáth, *Evolutionary games on graphs*, Physics Reports, 446 (2007), pp. 97–216.

[151] M. L. K. Tate, J. R. Adamson, A. E. Tami, and T. W. Bauer, *The osteocyte*, The International Journal of Biochemistry & Cell Biology, 36 (2004), pp. 1–8.

[152] M. Tauro, G. Shay, S. S. Sansil, A. Laghezza, P. Tortorella, A. M. Neuger, H. Soliman, and C. C. Lynch, *Bone-Seeking Matrix Metalloproteinase-2 Inhibitors prevent bone metastatic breast cancer growth*, Molecular Cancer Therapeutics, 16 (2017), pp. 494–505.

[153] J. P. Taylor-King, E. van Loon, G. Rosser, and S. J. Chapman, *From birds to bacteria: Generalised velocity jump processes with resting states*, Bulletin of Mathematical Biology, (2014).

[154] A. Trinh, I. H. Rye, V. Almendro, Å. Helland, H. G. Russnes, and F. Markowetz, *GoIFISH: a system for the quantification of single cell heterogeneity from IFISH images*, Genome Biology, 15 (2014), p. 1.

[155] R. F. M. van Oers, J. Klein-Nulend, and R. l. G. Bacabac, *The osteocyte as an orchestrator of bone remodeling: An engineer's perspective*, Clinical Reviews in Bone and Mineral Metabolism, 12 (2014), pp. 2–13.

[156] D. S. Vinay, E. P. Ryan, G. Pawelec, W. H. Talib, J. Stagg, E. Elkord, T. Lichtor, W. K. Decker, R. L. Whelan, H. S. Kumara, and Others, *Immune evasion in cancer: Mechanistic basis and therapeutic strategies*, in Seminars in Cancer Biology, vol. 35, Elsevier, 2015, pp. S185–S198.

[157] D. Wang and S. Bodovitz, *Single cell analysis: the new frontier in 'omics'*, Trends in Biotechnology, 28 (2010), pp. 281–290.

[158] Wellcome Images. http://wellcomeimages.org/. Accessed: 24-07-2015. Copyrighted work available under Creative Commons from Kevin Mackenzie, University of Aberdeen (B0008430).

[159] M. J. Williams, B. Werner, C. P. Barnes, T. A. Graham, and A. Sottoriva, *Identification of neutral tumor evolution across cancer types*, Nature Genetics, (2016).

[160] T. R. Wilson, J. Fridlyand, Y. Yan, E. Penuel, L. Burton, E. Chan, J. Peng, E. Lin, Y. Wang, J. Sosman, et al., *Widespread potential for growth-factor-driven resistance to anticancer kinase inhibitors*, Nature, 487 (2012), pp. 505–509.

[161] D. I. Wimpenny and A. Moroz, *On allosteric control model of bone turnover cycle containing osteocyte regulation loop*, Biosystems, 90 (2007), pp. 295–308.

[162] L. H. Wong, P. Pattison, and G. Robins, *A spatial model for social networks*, Physica A, 360 (2006), pp. 99–120.

[163] K. Xia, H. Xue, D. Dong, S. Zhu, J. Wang, Q. Zhang, L. Hou, H. Chen, R. Tao, Z. Huang, et al., *Identification of the proliferation/differentiation switch in the cellular network of multicellular organisms*, PLoS Computational Biology, 2 (2006), p. e145.

[164] J. Xiong, M. Piemontese, J. D. Thostenson, R. S. Weinstein, S. C. Manolagas, and C. A. O'Brien, *Osteocyte-derived RANKL is a critical mediator of the increased bone resorption caused by dietary calcium deficiency*, Bone, 66 (2014), pp. 146 – 154.

[165] S. Xu and A. D. Chisholm, *Highly efficient optogenetic cell ablation in C. elegans using membrane-targeted miniSOG*, Scientific Reports, 6 (2016).

[166] T. Yamada, S. Takeuchi, J. Nakade, K. Kita, T. Nakagawa, S. Nanjo, T. Nakamura, K. Matsumoto, M. Soda, H. Mano, et al., *Paracrine receptor activation by microenvironment triggers bypass survival signals and ALK inhibitor resistance in EML4-ALK lung cancer cells*, Clinical Cancer Research, 18 (2012), pp. 3592–3602.

[167] K. Zhang, C. Barragan-Adjemian, L. Ye, S. Kotha, M. Dallas, Y. Lu, S. Zhao, M. Harris, S. E. Harris, J. Q. Feng, et al., *E11/gp38 selective expression in osteocytes: regulation by mechanical strain and role in dendrite elongation*, Molecular and Cellular Biology, 26 (2006), pp. 4539–4552.

[168] X. H.-F. Zhang, X. Jin, S. Malladi, Y. Zou, Y. H. Wen, E. Brogi, M. Smid, J. A. Foekens, and J. Massagué, *Selection of bone metastasis seeds by mesenchymal signals in the primary tumor stroma*, Cell, 154 (2013), pp. 1060–1073.

[169] W. P. Ziemer, *Weakly differentiable functions: Sobolev spaces and functions of bounded variation*, vol. 120, Springer Science & Business Media, 2012.

[170] K. Zuev, M. Boguñá, G. Bianconi, and D. Krioukov, *Emergence of soft communities from geometric preferential attachment*, Scientific Reports, (2015), p. 9421.